HOKKAIDO UNIVERSITY

DOCTORAL THESIS

Synthesis and Surface Engineering of InSb Colloidal Quantum Dot for Short Wave Infrared Photodiodes

---

Author:

Subhashri Chatterjee

Supervisor:

Prof. Naoto Shirahata

A thesis submitted in fulfillment of the requirements

for the Doctor of Philosophy

of the

Faculty of Functional Material

Graduate School of Chemical Sciences & Engineering

March, 2024

Declaration of Authorship

I, Subhashri Chatterjee, declare that this thesis titled, Synthesis and Surface Engineering of InSb Colloidal Quantum Dot For SWIR Photodiodes and the work presented in it are my own. I confirm that:

- This work was done wholly or mainly while in candidature for a research degree at this University.
- Where any part of this thesis has previously been submitted for a degree or any other qualification at this University or any other institution, this has been clearly stated.
- Where I have consulted the published work of others, this is always clearly attributed.
- Where I have quoted from the work of others, the source is always given. With the exception of such quotations, this thesis is entirely my own work.
- I have acknowledged all main sources of help.
- Where the thesis is based on work done by myself jointly with others, I have made clear exactly what was done by others and what I have contributed myself.

Signed: Subhashri Chatterjee

Date: 2023/12/20

Acknowledgements

The last 4.5 years were an amazing roller coaster ride that came to an end. I would like to express my deepest appreciation to Prof. Naoto Shirahata who provided me to work under his guidance in his group. His encouragement, guidance, and support from the initial to the final level was a big help for me. Every lab meeting and discussion I have learned a lot from his profound knowledge. My respectful gratitude to you especially standing beside me during my surgery time and after!

I would also like to thank all the past and current members of the lab who supported me throughout the course and research. Without effective collaboration, knowledge sharing, and learning instrumental strategies, I won't be able to finish any part of my thesis. It was an amazing ride with a lot of ups and downs which makes this journey memorable.

Last but not least, I want to thank you my family for your immense support and for listening to all my frustrations during the low time. Without them, I don't think I could finish my PhD. I am grateful to my ma, baba, and wife because of their enormous love, trust, and support throughout my PhD journey.

Wish you a happy read! Thank you very much.

HOKKAIDO UNIVERSITY

Abstract

Faculty of Functional Material

Graduate School of Chemical Sciences & Engineering

Doctor of Philosophy

Synthesis and Surface Engineering of InSb Colloidal Quantum Dot For SWIR Photodiodes

by Subhashri Chatterjee

SWIR detection by photodiode has high demand due their photodetection capability beyond visible range. SWIR photodiodes has application from remote-sensing, light-detection ranging (LIDAR), optical telecommunications, bio imaging, infrared and thermal imaging, medical monitoring for healthcare researches. Bulk semiconductors such as InGaAs, InAs, InSb, InAsSb are used as photosensitive active layers for various photodetection. But the high fabrication cost of these complex device structure appeared to be challenging for various applications such as poor spectral tunability, less material choice. Additionally, complex and expensive cooling system also become a blockage for foldable emergent practical infrared application. While the solution processed colloidal semiconductor has various advantages to overcome those issues. It offers bandgap tunability by controlling the diameter of the nanocrystal, which affects the absorption or emission wavelength range for optoelectronics applications for quantum dot light emitting diode, quantum dot photodetectors. Additionally, synthesis of solution processed CQDs is a cost effective wet chemical process where mass production cost could be reduced by multiple factors. Till date Pb and Hg based CQD has been used for SWIR photodetection as the active layer of a photodetector. However, due to their high toxicity according to RoHS-restricted element, it is utmost necessity to find a suitable substitute material for SWIR detection. To evade the toxicity issues, III-V semiconductor based InSb have attracted significant attention due to their absorption in NIR to SWIR wavelength range. Therefore, the thesis focuses on the synthesis of high crystalline impurity less InSb CQDs with readily available halide precursors. Additionally, to improve the carrier mobility for fast charge transfer, long

chain Oleylamine (OLA) ligand was exchanged with short chain bromide and sulfide ligands for self-powered SWIR photodiode application.

In Chapter 1, general background of SWIR materials, overview about the synthesis of CQDs and figure of merits for photodetection. In details the process, the purpose of this research which led to the urgency of studying InSb CQD for SWIR sensing.

Chapter 2 focus on the facile synthesis of InSb CQDs with halide precursor. Unlike to previous all the InSb CQDs synthesise reports, the motivation of this study is to synthesis pure phase impurity-less InSb CQDs with less reactive and easily available and stable precursors. We have used chloride and bromide precursors by following hot-injection synthesis procedure. Additionally, we have compared the product prepared by the two precursors.

Chapter 3 focus on the surface modification by ligand exchange procedure. As Oleylamine (OLA) is a long chain ligand which helps to CQDs dispersed in solution, while it acts as an insulator for charge transfer for device application. That's why ligand exchange from long to short chain is an important step in solution processed optoelectronic field. Here, ligand exchange was performed by bromide and sulfide ligands to increase carrier mobility and charge transfer between the CQDs.

Chapter 4 focus on the fabrication of InSb CQD based photodiode for SWIR sensing. Here, we have demonstrated first-ever InSb CQD based photodiode for SWIR sensing where bromide capped InSb was used as active layer. The resulting PDs achieve a photoresponse of ~550 ms at 0 V, with combining the best values of responsivity and external quantum efficiency of 0.098 A/W and 10.1% under a bias voltage of −1 V at room temperature even in ambient air. Secondly, to improve the carrier mobility sulfide capped InSb CQD was further used as active layer, QPD responded as self-powered photodiode and achieves 1.3% EQE and responded 200 ms at 0 V, with 18.5% EQE at -1 V under 1100 nm.

Chapter 5 proposes future work on al-inorganic InSb CQD with further improvement and conclude the thesis.

Colloidal Quantum Dots, Photodetector, InSb, SWIR

Contents

List of Figures

List of Schemes

List of Tables

List of Abbreviations

IR	**I**nfrared
NIR	**N**ear **I**nfrared
SWIR	**S**hort **W**ave **I**nfrared
MWIR	**M**id **W**ave **I**nfrared
LWIR	**L**ong **W**ave **I**nfrared
FIR	**F**ar **I**nfrared
LED	**L**ight **E**mitting **D**iode
LIDAR	**L**ight **D**etection and **R**anging
QD	**Q**uantum **D**ot
HR-TEM	**H**igh **R**esolution-**T**ransmission **E**lectron **M**icroscopy
CQD	**C**olloidal **Q**uantum **D**ot
EMA	**E**ffective **M**ass **A**pproximation
QDLED	**Q**uantum **D**ot **L**ight **E**mitting **D**iode
PD	**P**hotodiode
PT	**P**hototransistor
PC	**P**hotoconductor
OLA	**O**leylamine
TOP	**T**rioctylphosphine
TOPO	**T**rioctylphosphine **O**xide
OA	**O**leic **A**cid
FA	**F**ormamide
DMF	**N,N**-dimethylformamide

BTA	**B**utylamine
ROIC	**R**ead-out **I**ntegrated **C**ircuit
QPD	**Q**uantum Dot **P**hotodiode

Chapter 1

Introduction

Infrared light detection or optical sensing is an important feature that has been used currently for many applications from night vision imaging, remote sensing, optical communications, solar cells photovoltaics, biomedical sensing, tumor detection, etc [1–5]. Currently, infrared sensors are made with narrow bandgap bulk III-V semiconductors such as InGaAs, InAs, InSb, and InAsSb materials for their high detection efficiencies[6]. However, they have obstacles to be overcome for versatile use in various scenes.

First, current device fabrication processes are based on heteroepitaxial growth, which makes it challenging to utilize a variety of light absorbers. Second, they lack spectral tunability over a broad wavelength range due to the inherent photosensitivity of bulk crystals. Third, complex and expensive cooling systems and huge driving voltage have also become a blockage, significantly hampering the practical application of miniatures flexible portable IR devices in the future[7,8]. As a counterpart of this solution processed colloidal quantum dots as an active layer of photodetectors are being simplify the fabrication process with very cheap and cost effective for large scale production. Colloidal QDs can be tuned for different wavelengths by changing the diameters which could apply to the size-selective sensitivity of a photodetector. In the last decades, lead

and mercury-based colloidal QDs have been studied vastly as they are highly absorbing from Near-infrared (NIR) to short-wave infrared (SWIR) wavelength light[9–14]. However, due to their high toxicity, researchers are trying to investigate as a substitute for NIR to SWIR range.

In this context, InSb has excellent potential for SWIR applications as photodetectors. Bulk crystal InSb has been used in photovoltaics applications as it exhibits excellent electronic properties[15]. In the present work, I demonstrate a novel synthesizing process to synthesize InSb nanocrystals with readily available bromide precursors for al-inorganic SWIR photodiode application. Later I developed two different short-chain ligand exchange engineering processes to improve the charge transport between the dots to achieve a higher response with a high figure of merits of photodetector under the SWIR range.

1.1 SWIR application

The infrared region appears after the visible region from 800 nm to 100 μm. Figure 1.1 shows the full spectrum of the infrared region. While the transmission window can be divided into several sections, near-infrared (NIR) from 800 nm to 1 μm, short-wave infrared (SWIR) from 1 μm to 2.5 μm, mid-wave infrared (MWIR) from 2.5 μm to 5 μm, long-wave infrared (LWIR) from 5 μm to 12 μm, far-infrared (FIR) 12 μm to 100 μm.

FIGURE 1.1: Electromagnetic spectrum region

NIR to SWIR light extends region the vision ability which has been limited to visible wavelength. Infrared radiation was discovered by William Herschel [16]. Over the 200 years, there has been a continuous development in NIR/SWIR sensing to move our vision ability beyond visible wavelength. Earlier research on infrared technology was started by military applications for infrared detection and imaging[17]. Later there was a huge interest in applying infrared technology in other sectors such as commercial, industrial, environmental, medical, and communications.[18–20] For biomedical instrumentation, a pulse oximeter uses NIR and red LED to measure oxygen saturation.[19] Further, there has been extensive progress in solar cell application by integrating the visible region with the NIR range.[18]

A fundamental fact on SWIR light is not visible to our human eyes, although the light interacts in the same manner as visible light because of its reflective nature. SWIR light can penetrate through smoke, fog, etc., Figure 1.2 shows various images captured by QD-based SWIR image sensors. Primarily, SWIR sensors are heavily used in military applications such as night vision cameras and LIDAR applications.[20,21] Additionally, the SWIR spectral window offers low transmission loss which is why it is also used in telecommunication applications for 1.3 μm and 1.55 μm. Apart from these, it is also used in the sorting of products for food technology, temperature estimation, semiconductor inspection, etc. In this context, InGaAs have been used as the first choice for SWIR wavelength detection as it is extremely sensitive to this range of light. InGaAs-based sensors achieve high quantum efficiencies with high response speed which makes this material the perfect choice for this spectral region.[21]

However, there have been many obstacles to various application scenarios. Firstly, the fabrication process is based on heteroepitaxial film growth makes it difficult to expand the choice of material. Second, the

use of heteroepitaxial films results in poor spectral tunability over a broad wavelength range due to the inherent photosensitivity based on the energy structure of the bulk crystal. Third, complex and expensive cooling systems and huge driving voltage have also become a blockage, significantly hampering the practical application of miniatured flexible portable IR devices in the future.[7,8]

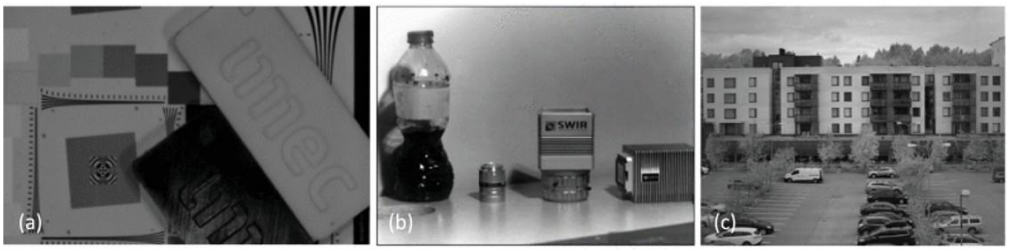

FIGURE 1.2: QD-based SWIR images produced by different image sensors (a) PbS QD, SWIR image (cutoff at 1.6 μm), 5-μm pixel pitch, and data courtesy of IMEC. (b) PbS QD, SWIR image (cutoff at 2 μm), 15-μm pixel pitch, and data courtesy of SWIR vision systems. (c) PbS QD, SWIR image (cutoff at 2 μm), 20-μm pixel pitch, and data courtesy of Emberion.)

1.2 Emergence of CQD

In a QD structure electron and hole-bound pairs which are known as exciton experience quantum confinement in all three spatial dimensions.[22] In the past two decades, CQD has attracted huge attention because of their various advantages: firstly, the bandgap tunability by controlling the diameter of the QDs, secondly the bandgap tunability also supports the optical and electrical modification of the QDs which is the most important feature over bulk semiconductors.[23] Quantum confinement appears if the QD diameter is smaller than Bohr's radius of the materials.[22] Decreasing the size of the QDs leads to achieving higher bandgap values because of an increase in the degree of quantum confinement. In a semiconductor, an electron-hole pair which is known as an exciton appears when an external photon incident. The exciton Bohr radius is known as the average distance

between the photo-induced bound electron-hole pair. Effective mass approximation (EMA) is used to investigate the size-dependent bandgap (E_g) of semiconductors and the equation is expressed as follows:[24]

$$E_g = E_{g0} + \frac{h^2}{8m_0 R^2}\left(\frac{1}{m_e^*} + \frac{1}{m_h^*}\right) \quad (1.1)$$

Where E_{go} is the bulk bandgap, R is the radius of the QD, m_e^* and m^*_h are electron and hole effective mass, respectively; h is the Planck constant, m_o is the free electron mass.

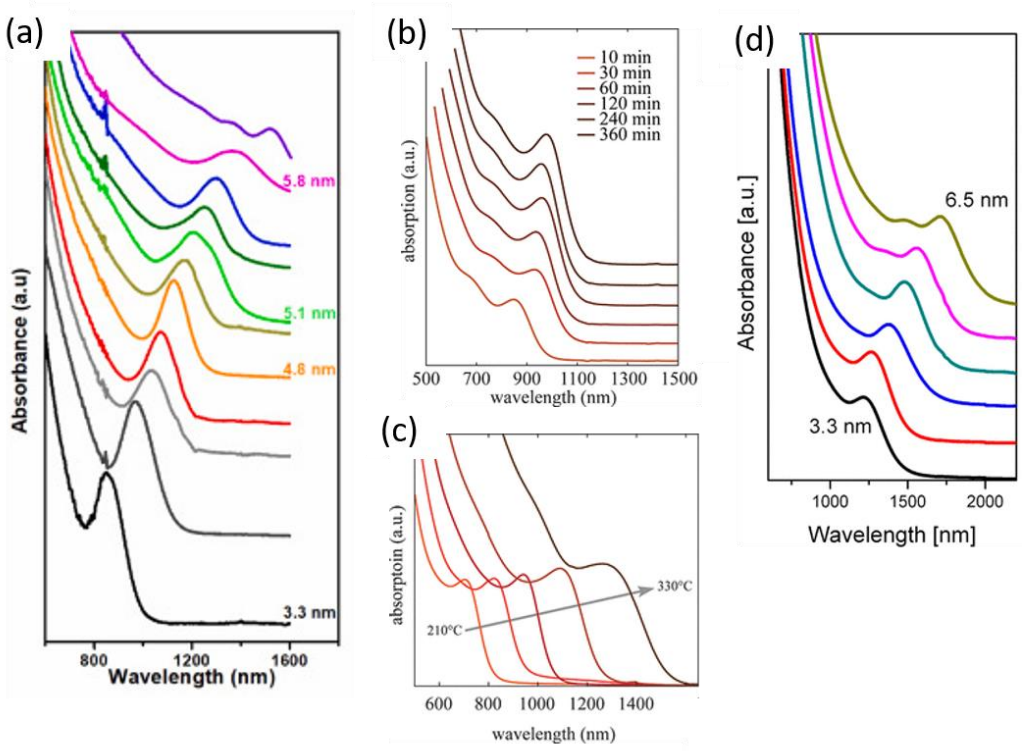

FIGURE 1.3: Size dependent absorption spectrum of (a) PbS CQD[25], (b)-(c) InAs CQD[26], (d) InSb CQD[27].

Figure 1.3 (a) shows the QD size-dependent excitonic feature where the size of the QD was varied from 4.3 nm to 8.4 nm. As an example, bulk PbS

has a Bohr radius of 21 nm, to obtain the strong quantum confinement of PbS QD was synthesized with a much smaller size than the Bohr radius. These tunable optical properties attract various QD-based optoelectronics applications such as photodiode photodetectors, LED, and solar cells.[9–12]

Further Figure 1.3 (b) and (c) show the size-dependent excitonic feature, where the excitonic peak was observed to shift due to changes in reaction time and temperature, respectively.[26,27] The bigger the CQD size exciton moves towards more SWIR range. Similar trends appear for one more material from III-V family InSb, where Talapin et al show size-dependent excitonic features InSb CQD size was synthesized from 3.3 - 6.5 nm, where exciton and emission redshifts towards the SWIR range were observed.

1.2.1 Colloidal Synthesis of QDs

The typical size-tuning properties and surface modification of QDs have generated broad interest to study next-generation photophysical applications for several optoelectronics devices (i.e., QDLED, QD-photodiode, QD-phototransistor, QD-Photoconductor, QD-Photodetector, QD-solar cells).[28–32] Colloidal synthesis of QD is a wet chemical approach to preparing QDs. By the superiority of this method, different sizes of QDs also prepared by easily tuning several parameters during the synthesis. One can control the reaction time, temperature, molar ratio of precursors, etc. to tune the working range of the QDs.[33] Several advancements in this wet chemical method al- low a wide range of researchers to prepare QDs at a very low-cost compared to other established methods.[33]

In a typical synthesis of CQDs, reaction solvents, precursors reagent, and reducing agent is mixed at high temperature and kept to react for some time to produce the product. After the completion of the synthesized reactive

solvent is washed by several centrifugation steps to separate different sizes of CQDs. There are two common way of synthesis methods, heat-up synthesis, and hot-injection synthesis method.[33] In the heat-up synthesis method, mixing the reagents and precursors at room temperature and elevating the reaction temperature at a constant time, after reaching the desired temperature reaction solution kept reacting for some time. Whereas, for the hot-injection method all the precursor and reagent additions were done at high temperatures and after that kept for some time to react. Figure 1.4 shows a schematic of a typical synthesis procedure by heat-up and hot-injection methods. In a typical nanocrystal synthesis, first precursors are converted into monomers, then after achieving the threshold of monomer concentration, it starts to form nuclei. After the formation of the nuclei, it follows particle growth. After achieving the desired particle size reaction typically quenched to stop further particle growth.

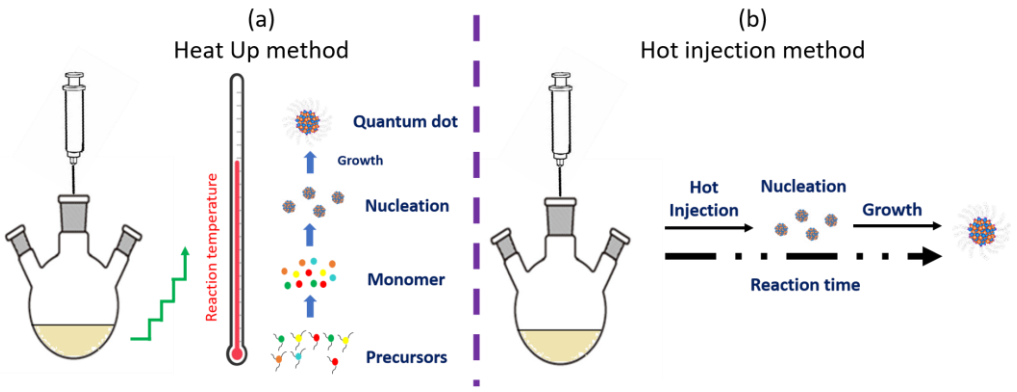

FIGURE 1.4: Schematic of nucleation and growth by (a) Heat up (b) Hot injection synthesis method.

1.2.2 Hot-injection synthesis of CQD

Synthesis of CQDs (CdS, CdSe, CdTe) by hot-injection method was developed in the early 1990s by Murray et al.[34,35] A common hot-injection synthesis of CQDs is carried out in a three-neck flask where rapid or drop-by-drop injection of one precursor solution into a reactive mixture at high temperature. According to the La Mer model at high temperature shown in Figure 1.5, a short burst of nucleation occurs where it suddenly boosts monomer concentration above the monomer concentration.[36] Upon injection of other precursors, the nucleation process stopped due to a reduction of temperature and a decrease in monomer concentration. Further, it follows the growth stage and after that Ostwald ripening stage. After reaching the desired CQD size heating source was removed and the reaction was quenched immediately by an ice bath. Different sizes of CQD can be tuned during synthesis by changing reaction temperature, reaction time, molar ratio or precursor, selection of precursors and ligands, etc. For example, after completing the Ostwald ripening stage, the longer the reaction time, the bigger the QDs grow further and form big agglomeration. Another example could be the injection of reactive precursor at higher temperatures could process particle growth step faster, which will further make bigger size QDs for keeping a long time. The concentration of the reaction mixture and ligands also can affect to achievement difference in the average size of QDs.

1.2.3 Purification and Size Selection of CQDs

After completion of the synthesis, the crude solution needs to be centrifuged to separate the impurities, organics, and non-reactive substances

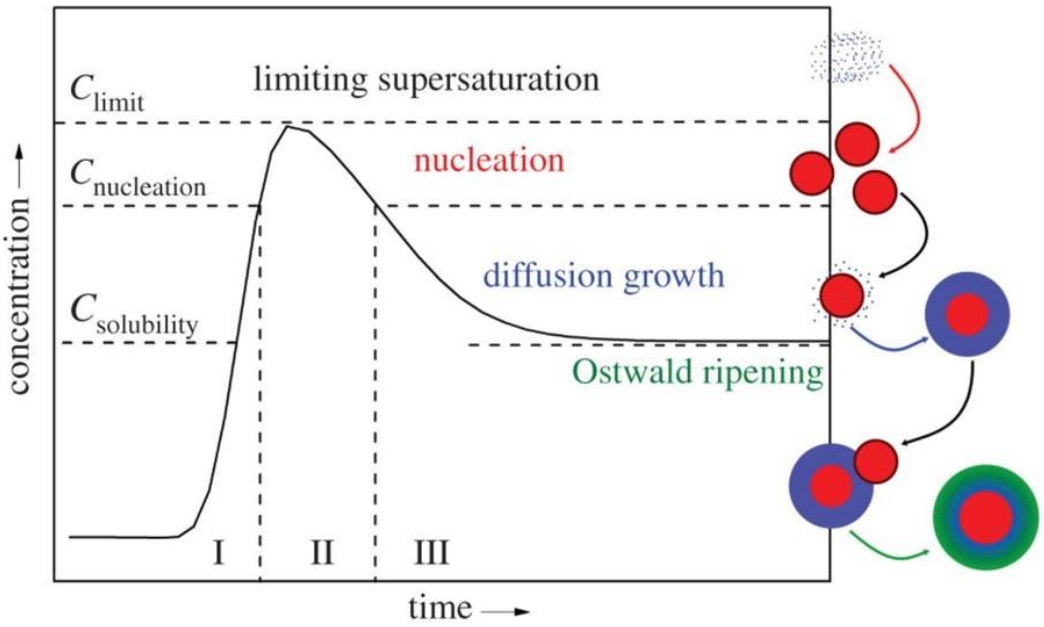

FIGURE 1.5: Schematic of La Mer model of synthesis of nanocrystals with time.[36]

from the final desired product. The centrifuge or washing process is always performed under air or in an inert environment (such as inside a glovebox or using a rubber stopper plastic sealed centrifuge tube). To acquire the final product through the centrifuge process multiple sequential precipitation and re-dispersion of CQDs by using solvents and anti- solvents. After synthesis, due to the satirical characteristics of CQDs with organic ligands are favored to disperse in the non-polar solvent.[33,37] To separate the nanoparticles, destabilization of CQD dispersion should be reduced by the addition of some anti-solvent (such as methanol, ethanol, etc.) which increases the polarity of the solution mixture to decline the inter-dot repulsive forces between the CQDs. Further, the QDs get aggregated and precipitated, while by-product and precursor residues are separated with supernatants. Further, precipitated/isolated samples were washed by re-dispersion of solvents and anti-solvents to rid out organic residues bound on the surface of the nanoparticles, while the supernatant was washed with only the addition of an anti-solvent. To achieve the size selective precipitation washing with anti-solvent was performed multiple times only with the supernatant ascribed from every

washing step. Due to larger van der Waals forces between the bigger QDs compared to the smaller ones, they aggregate before due to the addition of an anti-solvent.[38] A higher amount of anti-solvent causes precipitates the big-size QDs easily, that's why it is very important to control the amount of anti-solvent during the size-selective precipitation. The washing steps including the selection of solvent and anti-solvent play an important role in the colloidal stability and optical and electrical properties of nanoparticles.[39] In colloidal chemistry size distribution plays a major role in achieving better optical characteristics such as absorption or PL.[27,34,40] Narrowing down the CQD size distribution helps to achieve sharp and narrower features respectively. In that context, size-selective precipitation by controlling the anti-solvent amount during centrifuge is a crucial step in colloidal chemistry.

1.2.4 Improving Surface Chemistry by Ligand Exchange of CQDs

For next-generation thin-film technology solutions processed optoelectronics devices are very promising candidates.[23,41–46] Opto-electronic properties of QDs depend on various reasons such as the structural pattern of the QDs, sizes, and shapes, and most importantly surface of the QDs. The surface chemistry of QDs is solely connected to carrier mobility, charge transfer between adjacent QDs, doping concentration, and energy levels.[47,48] As-synthesized QDs capped with long-chain native ligands are not suitable for device application as they work as an insulator for charge transfer. [46]That is why it very important step for making functional devices to exchange the ligand from the long chain to the short counterpart to improve carrier mobility, energy band, stoichiometry, and the surface of the QDs.

A surface ligand of CQDs is molecule that is attached to the CQD surface and protects the core with adjacent CQDs in a solvent as a solution

form for a long time. In a solution without the surface ligand CQDs could destroy the core by agglomeration with other CQDs. Additionally, surface ligands during synthesis help to control the kinetics of nucleation and growth.[34] There are three types of surface ligands commonly used in the QD system: X-type, L-type, and Z-type.[49] X-type ligands are attached with opposite ionic charged sites on the CQD surfaces. Some examples are inorganic ions such as halides, chalcogenides, etc. A few others are carboxylates ($RCOO^-$), phosphonates ($RPO(OH)O^-$), and thionates (RS^-). While L-type ligands such as amines (RHN_2) and phosphines (R_3P) are neutrally charged, they coordinate with metal atoms on the surface with a lone electron pair. Z-type ligands are those having neutral molecules that can attach to the electron-rich side as electron acceptors with their metal atoms.

Typically, organic molecules and long hydrocarbon tail ligands such as oleylamine (OLA), trioctylphosphine (TOP), and trioctylphosphine oxide (TOPO) are L-type and oleic acid (OA) X-type ligands are used in chemical synthesis of CQDs.[23] During the chemical synthesis of CQDs such as PbS, PbSe, CdS, CdSe, CdTe, InAs, InP, HgTe, HgSe, InSb, InAsSb, OLA, and OA have been used widely to prevent aggregation and sterical stabilization for the QD growth system by making an outer shell.[23] While making the QD in the thin film as a solid layer these long chains capping agents poorly transfer the charges between the QDs.[50] To improve the carrier transport phenomenon in thin films these long chains are favored to exchange with

the more compact short-chain ligands such as ethanedithiol, mercaptopropionic acid, ethylenediamine, mercaptoethanol, etc. After exchanging ligands inter-dot distance is reduced and improves the charge transport.[50,51] Figure 1.6 (a) shows a schematic of QD assembly before and after ligand exchange, the inter-dot distance is reduced after short ligand treatment.[52]

There are two kinds of ligand exchange methods present: Solid State ligand exchange process and Solution process phase change ligand exchange process.[53–60] Solid-state ligand exchange is performed during the fabrication process of spin coating of the QD layer on the substrate.[59,61] Firstly long-chain capped ligand dispersed in the non-polar is prepared, while at the same time short-chain ligand in a polar solvent solution is also prepared. Then the long-chain capped QD solution is spin-coated on top of the substrate and after that device is immersed/rinsed into the short- chain ligand solution for a few seconds to exchange the ligands. Within a few seconds, the new ligand is introduced in the device system leading to a reduction of QD distance. During the ligand exchange process, cracks or structural rearrangements may happen on top of the layer which might affect the electrical performance. That is why these ligand exchange processes repeat many times (layer-by-layer fashion) to fill the cracks and thicken the QD layer to achieve better carrier mobility.[62] Although the mobility of a device does not only depend on the thickness of the QD layer, it depends on many other parameters which will be discussed in the later part of this thesis.

There is another kind of ligand exchange process is the solution process ligand exchange.[51] The important part of the solution ligand exchange process is dispersity because long-chain ligands usually aggregate in polar solvents. As for the hydrocarbon chains, it is energetically favorable to minimize their contact with the polar solvents, which causes a reduction

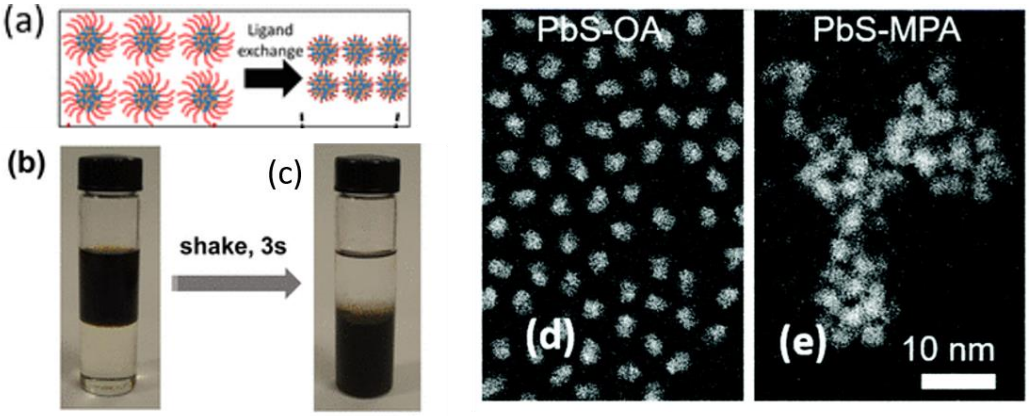

FIGURE 1.6: (a) Schematic ligand exchange before and after, Phase change during solution process ligand exchange[52] (b) before and (c) after,[63] (d) and (e) are HR-TEM images[64] of before and after ligand exchange of PbS CQDs respectively.

of steric stabilization and leads to aggregation. Consequently, the polarity on the QD surface transforms from non-polar to polar which results in a phase change after some mixing, which is labeled as a phase change of the QD solution. Solution-phase ligand exchange chemistry has been applied successfully in many II-VI, IV-VI, and III-V semiconductor QDs with thiol and halide ligands.[53,65–67] Balancing the charges on the QD surface is the key to attaching new ligands is the key to a ligand exchange process, as the anionic ligands are attached to the cationic side of the surface. For solution, ligand exchange FA, DMF, and BTA solvents are used widely. Experimentally, it is visually realized the clear phase change after ligand exchange. For example, Figure 1.6 (b) and (c) are solution process phase changes before and after ligand exchange of PbSe QDs from Hexane (top) to DMF phase (bottom) using NH_4I[63]. For IV-VI and III-V semiconductor CQDs after ligand exchange, some solvents such as DMF, FA, BTA, etc. are used to improve the QD assembly and coordination in thin films.[51] There is an advantage for solution ligand exchange over solid-state ligand exchange QDs for device fabrication is that the layers of the device become smooth with fewer or no cracks and closely packed QDs in thin film form, which makes it superior for better thin film applications. Besides the improvement in thin film and stabilization of CQDs, other properties influence its

superiority. The distance between the QDs also determined by the size of the ligand molecule, which affects the electronic coupling in thin film.[50] Figure 1.6 (d) and (e) show an HR-TEM image of PbS CQDs[64]. In this way, by increasing the electronic coupling the mobility of the device increased.

Further, the energy band HOMO, LUMO, and fermi levels of CQDs can be tuned by controlling the doping concentration of the material, where the doping concentration is directly connected with the different surface ligands.[50] Because the ligand engineering induces dipoles between atoms and ligand headgroups. Depending on the characteristics of the surface ligands the energy band and fermi level of the CQDs shift from vacuum. Previously, there has been much research on Pb-based ligands achieving n-doped and p-doped characteristics after ligand exchange which has been summarized in Figure 1.7 (a).[68] Major advantages of this study are CQD solution after ligand exchange can acquire higher carrier mobility with different doping. Additionally, Pb-based CQDs with the n-doped and p-doped solutions were prepared and applied as solution-processed Pb-based p-n junction diode which reduced the fabrication cost with accompanying high detectivity of NIR to SWIR light.[69] However afterwards, re- searchers are trying to achieve similar ligand exchange techniques to pre-pare III-V semiconductor-based n-doped and p-doped CQDs such as with InAs, In(As)P CQDs.[70–73] Figure 1.7 (b) shows energy band level of In(As)P CQDs with native ligand and another short chain ligand MPD $BuNH_2$. Figure 1.7 (c) shows the energy band of InAs CQDs with halide and thiolate ligands, the fermi level has been shifted indicating intrinsic to heavily n-type characteristics.

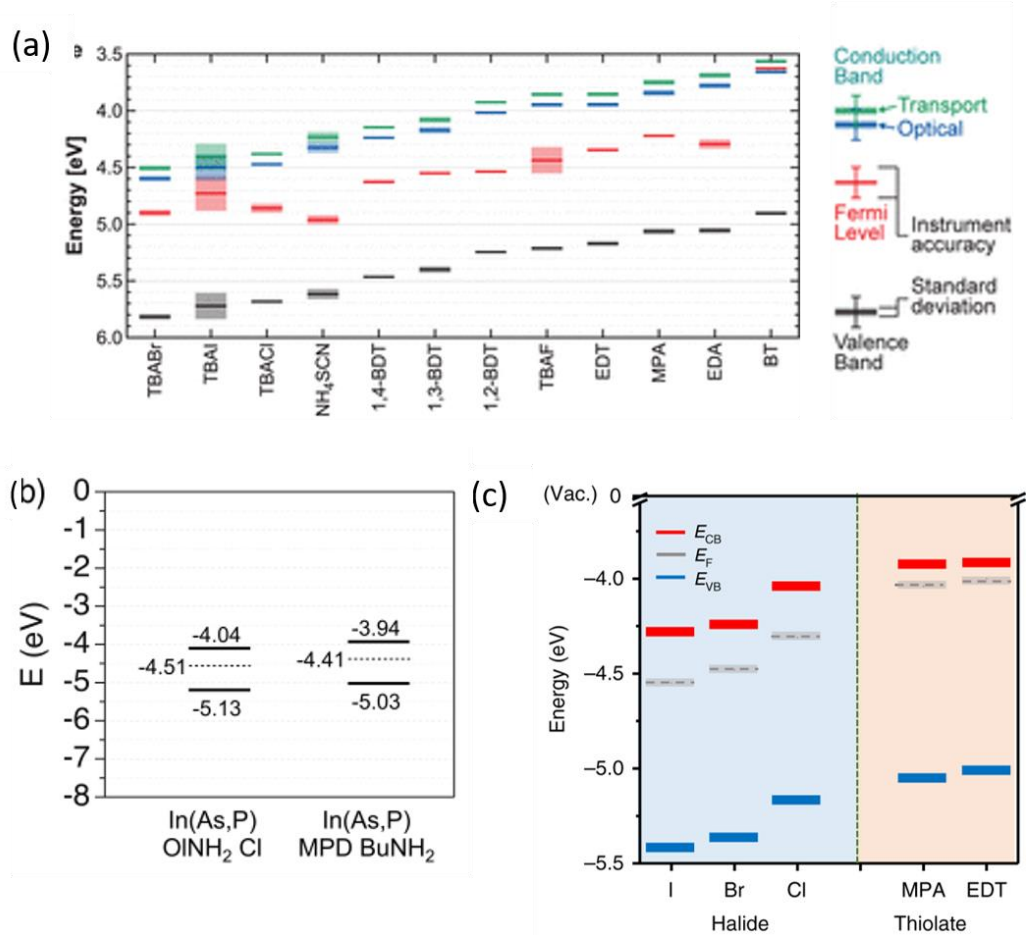

FIGURE 1.7: Energy levels of (a) PbS[68] and (b) In(As)P[74] and (c) InAs[73] CQDs after different ligand exchange treatment measured by UPS.

1.3 Advantage of Solution-Processed QD based photodevices

Optoelectronic device fabrication with CQDs is most promising topic for the next generation, as it holds many advantages compared to bulk semiconductor-based devices. It simplifies the fabrication process which helps to synthesize and fabricate on a mass scale with less expense.[32] Currently, the mass production of infrared sensing and imaging devices is performed by epitaxial semiconductor technologies. But, in near future CQD based solution processed can be used as a superior substitution.[32] CQD

ink can be synthesise and prepared with desired structural and optical properties which can be very effective in device application, owing to the size tunability and surface modification CQD holds very promising application. Solution processed CQD devices can be fabricated by several cheap thin film fabrication technique such as spin-coating, dip-coating, spray-coating, inject printing, 3D printing, doctor blade coating etc.[32,75] These fabrication processes are not requiring vacuum-free, low temperature environment which reduces the fabrication cost and as well as can be prepared in flexible substrates also. In the following part I will discuss about the three main kind of optoelectronics devices such as: field-effective transistors, solar cells, photodiode and photodetector.

1.3.1 QD based photo-transistor - QDPT

In modern analog and digital electronic, transistors are the fundamental devices. Colloidal QD based thin FET can be integrated in ICs, where the fabrication of bottom-gate or top-gate FETs can be done by simply spin coating the QD layer on top of Si/SiO_2 substrate. During the spin coating the QD as active layer solid state ligand exchange also can be done to increase the carrier mobility of the device. In a FET structure, top electrodes namely source and drain can be evaporated by thermal or electron-gun evaporation through some metal mask. In FET structure, channel length which is the distance between source and drain is an important part of the device, in general shorter the distance faster the charge transportation. Although, fabrication of short channel length is hard, usually it is around several μm scale. The carrier concentration and conductivity of the device between the channel is control through the gate bias. At unbiased or insufficient bias voltage, transistor conductivity is very poor. But, increasing the voltage to

a sufficient level carrier concentration increase and form the conductive path through the source and drain channel, that voltage known as threshold voltage (V_t). By increasing the V_t device operates as ON state. Many important figure of merits and characteristics can be determine by the analyzing QDPT, such as: carrier mobility, on- off ratio, responsivity, EQE, time response, threshold voltage etc. For real time applications, on-off ratio and mobility are two most important factors for FET. Recently, QDPTs are integrated with some 2d materials such as graphene/black phosphorous to improve the on-off ratio and mobility.[76] On that context, sufficient solution and solid-state ligand exchange process helps to improve the figure of merits of the device. Figure 1.8 shows the performance of a hybrid QDPT where black phosphorous was used with InP CQDs as active layer. Figure 1.8 (a) shows the schematic diagram of the device, where Figure 1.8 (b) shows the optical image of the device including the channel between the drain and source. Figure 1.8 (c) shows the TEM image of the InP CQD which has been used as active layer. Figure 1.8 (d) shows the current from drain to source which has been controlled by gate voltage in dark and light condition and Figure 1.8 (e) shows the current from drain to source with different optical power densities. Figure 1.8 (f) shows the photoresponse of the device under different light intensities at a drain-source voltage of = -60 V. By increasing the light intensity, the photocurrent and photoresponse increases.

1.3.2 CQD-Based Solar Cells

Solution processed solar cell has been first reported in 2005, PbS CQD as active material.[77] PbS CQDs shows strong quantum-confinement where bandgap energies were 1.1-1.3 eV, established as promising candidate for

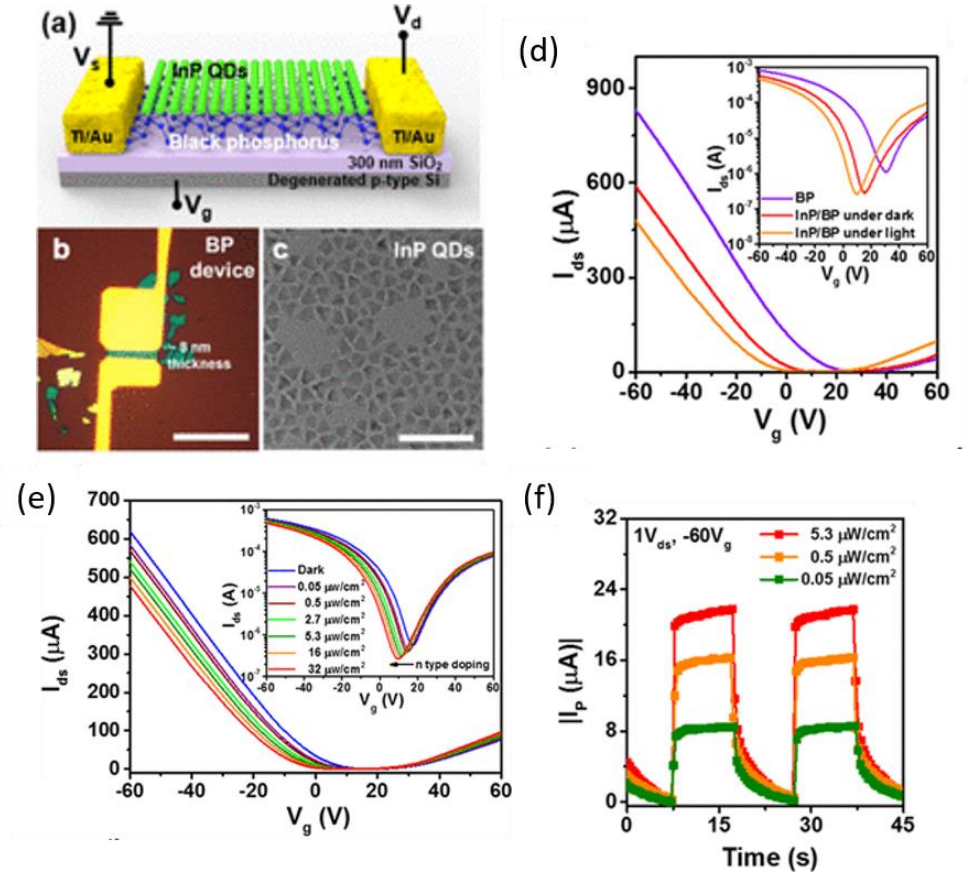

FIGURE 1.8: (a) Schematic diagram of QDPT. (b) Optical image of FET. (c) TEM images of InP CQDs. (d) I_d vs V_g characteristics of the QDPT. (e) I_{ds} vs V_g characteristics of the QDPT with different optical power intensities. (f) Photoresponse of the device with different optical power densities at V_{ds} and V_g = -60 V.[76]

photovoltaics.[28] Since the first report, there has been extensive studies with PbS CQDs based photodiode, photodetectors and solar cells.[2,11,12,25,64,78] In solar cells most important figure of merit is power conversion efficiency (PCE), PbS CQD based devices shows improvement from 4 to 12 % till now.[79] A solar cell p-i-n or p-n junction diode structure consists of a transparent substrate (such as ITO or FTO), above that p- and n-QD layer as an active layer and top of that one metal electrode (such as Ag, Al, Au). Solar energy conversion in P-i-n or p-n junction diode relies on the sufficient electron-hole separation and collection of carriers in electrodes. Carrier recombination and collection mostly depends on the thickness of the depletion region; too thick active layers can suffer with carrier recombination. Which further leads to higher series resistance and lower

PCE. However, there has been few researches on finding optimal thickness of the PbS QD based devices, where thickness of the QDs has been tuned from 80 to 400 nm.[69,79] Depletion region is formed at the interface of p-n junction or metal/semiconductor interface. Charge carriers generated by incident illumination which gets the drift velocity under the built-in-potential V_{bi}. The width of the depletion length can be determined by the following formula:[80]

$$x_d = \sqrt{\frac{2\epsilon s}{q}\left(\frac{1}{N_a} + \frac{1}{d}\right)(V_{bi} - V_a)} \tag{1.2}$$

Where ϵ_s is the permittivity of the semiconductor, V_a is the applied bias. N_a and N_d are the concentrations of acceptors and donors in the n-type and p-type material, respectively. In a p-n doped photodevice depletion layer majorly lies mostly on the heavily doped side of the junction. In the case of highly p-doped where $N_d > N_a$, depletion width is inversely proportional to N_a. For solar cell p-n or p-i-n devices improvement of PCE of recent devices are being done by modifying the device structure. Recently, PbS CQD based p-n junction solar cell achieved 13.30 % of PCE[78]. Figure 1.9 (a) shows the schematic diagram of PbS CQD-based solar cell device. Similar device structure with solution processed PbS ink has been reported for solar cell applications.[78] Here, ZnO nanoparticle solution was spin-coated as ETL. Lately, ZnO as a wide bandgap has been considered superior candidate for electron transport layer with highly n-doped nature. Further, PbS CQD ink was used as active layer. PbS-MPA ligand (ligand exchanged by solid state exchange process) was used as HTL and Au was used as electrode.

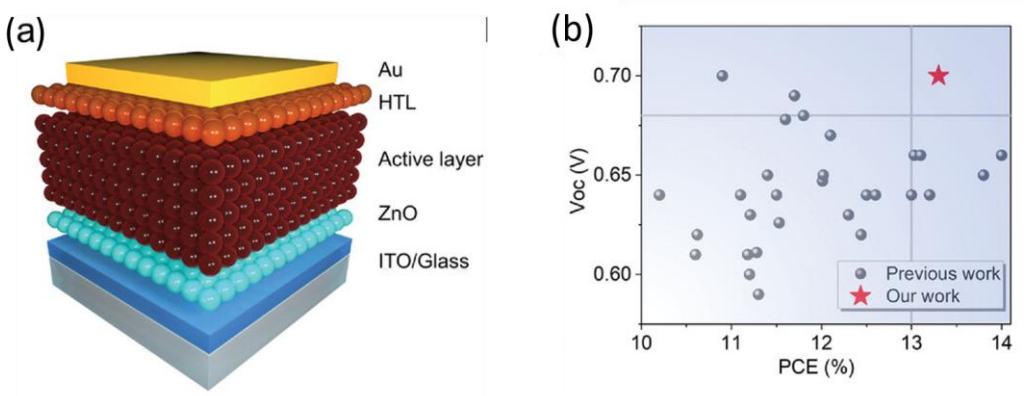

FIGURE 1.9: (a) Schematic diagram of PbS CQD-based QPD.[78] (b) open-circuit voltage (V_{oc}) of PbS CQDs solar cells with PCE >10%. (Note that the bandgaps of PbS CQD solar cells are calculated via their absorption/external quantum efficiency onsets).[78]

1.3.3 CQD based Photodiode Photodetector - QPD

Photodiode photodetectors are similar with p-n/p-i-n structure solar cell where only exception is that it working function is self-powered mode and mostly reverse bias voltage. Additionally, the time response speed of a photodiode photodetector is much faster than solar cell. High speed detection ability is an important figure of merit of a photodiode, mostly photodiode is integrated with ROIC circuit for application. Photoconductors and phototransistors are two and three terminal photodetectors. The differences of working phenomenon of PC or PT are carrier transport phenomenon with lateral side, while PD photodetectors works where carriers move vertically. Post-visible areas where Si limits its application, there has been very less option for SWIR sensitive materials in-terms of high performances and less-toxicity. PbX and HgX (X = S, Se, Te) are being used vastly for SWIR application with high performances but due to their high toxicity its urgent needs to find less toxic or non-toxic materials to introduce in this field of research. Recently, III-V semiconductors are introduced with InY (Y = As, Sb, AsSb, AsP) for NIR to SWIR photodiode.

QPD shows broad spectral sensitivity throughout NIR to MWIR range. There are many figure of merits are important parameters to judge the performance of a photodiode.

(a) **Dark current (A)**: Dark current of a photodiode flows when there is no illumination on the active areas of the diode, but still there is some current exists due to trap states, high junction defects, high roughness of layers, oxidation of active layers etc. High dark current impacts negatively on a photodiode performance. Device performance is inversely proportional to the dark current of photodiode. Figure 1.10 (a) shows a schematic inverted stacked InAs QPD device where the dark current has been achieved very less (10^{-11} A) shown in Figure 1.10 (b).[72]

(b) **Photocurrent (A)**: Photocurrent of a QPD is the current generate after illumination of incident light in the active area of the device. Due to the incident light electron-hole payer generates and a depletion region formed. Photocurrent at 0 V or no bias condition is known as self-powered phenomenon of a photodiode, on the other hand in bias condition especially at reverse r negative bias condition photodiode generates higher currents than dark condition. In ideal condition, by increasing the illumination intensity current at 0 V and reverse voltage increases linearly. Similar effect has been shown in Figure 1.10 (b) of inverted stacked InAs QPD device, where photocurrent at 0 v and negative bias increases by increment of the incident light power density.[72]

(c) **Photoresponse Speed (s)**: Photoresponse speed of a photodetector measured under light ON and OFF state. In this case photoresponse speed determines how fast a photodetector sense to incident light. Figure 1.10 (c) shows a photoresponse of PbS QPD under light ON and OFF state un- der different bias situation.[10] In theoretical study, photoresposne speed in

the case of photodiode photodetector is faster than phototransistor photodetector. Because, in the case of photodiode, upon incident of light carrier transport phenomenon occurs vertically in between the stacked layer which is in nm scale distance. On the other side, for phototransistor, upon illumination of light carrier transport happens in lateral direction between the two electrodes namely channel length. Usually, channel length of a phototransistor is in μm scale, far longer distance to travel compare to stacked photodiode structure.

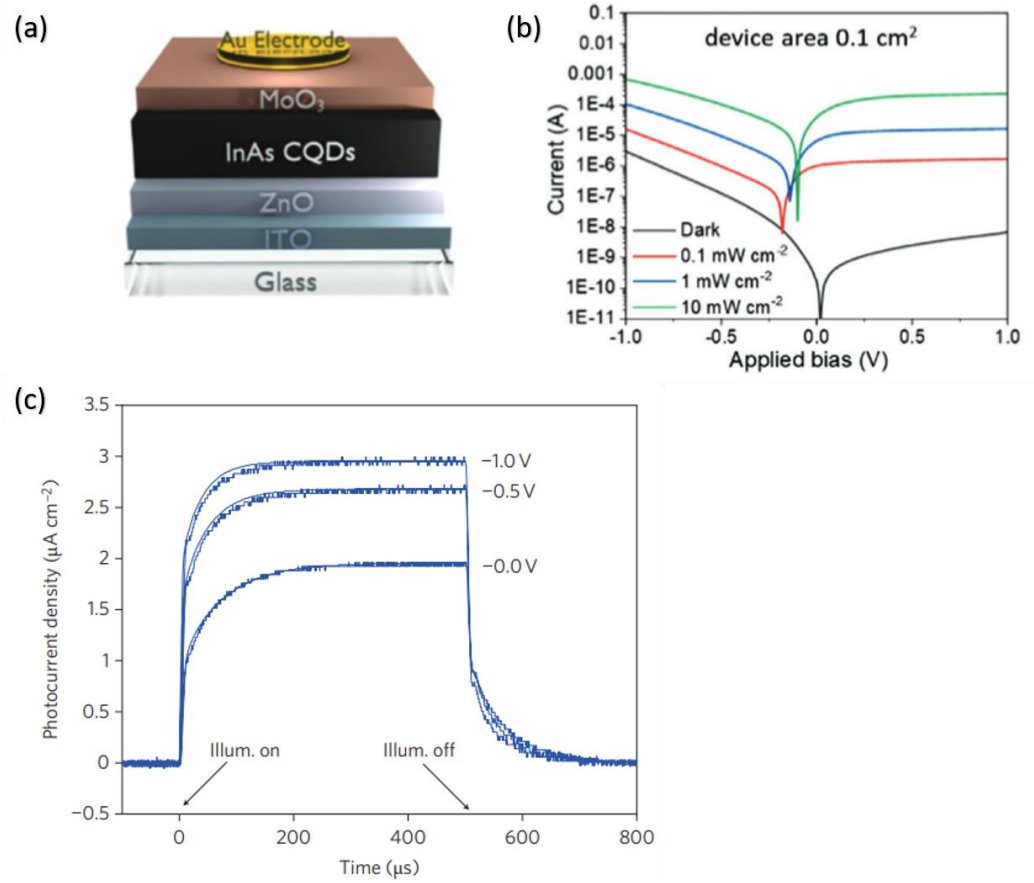

FIGURE 1.10: (a) Schematic diagram of InAs CQD-based QPD.[72] (b) I-V characteristics of the QPD under dark and light condition in log-scale,[72] (c) Photoresponse speed of a PbS QPD under light ON and OFF state.[10]

(c) **Responsivity (A/W)**: Responsivity of a photodiode is defined as the generated photocucurrent due to incident light per incident unit optical

power expressed in Equation. 1.3.

$$R = \frac{I_{light} - I_{dark}}{PA}; \tag{1.3}$$

Where, I_{light}, I_{dark}, P and A are the photocurrent, dark current, incident light power and area of the active area of the photodiode.

(d) **EQE (%)**: EQE values indicates the amount of current generates by incident a particular wavelength of light on to the device. The current generates due to photon is known as photocurrent which is equal to electron in other side. Generally, by simplifying, EQE is the ratio between number of carriers conducting and number of incident photons which has been expressed in Equation. 1.4. Figure 1.11 (a) shows EQE values of PbS QPD under different wavelength light.

$$EQE = \frac{hcR}{e\lambda} \tag{1.4}$$

Where is h is the planck's constant, and c is the speed of light, R is the responsivity, e is electric charge and λ is the wavelength of incident light.

(e) **Noise Current**: The lowest detectable current or signal in dark condition is known as dark current which determines the sensitivity or detectivity of a photodetector. Although the high dark current is due to presence of many noises signal which could be eliminated in the ideal condition. The noise current can be expressed as shown in Equation 1.5.

$$\begin{aligned} i_{\text{noise}} &= \sqrt{i_{\text{shot}}^2 + i_{\text{thermal}}^2 + i_{\text{trap}}^2} \\ &= \sqrt{2ei_{\text{dark}}B + \frac{4kTB}{R_{\text{sh}}} + i_{\text{trap}}^2} \end{aligned} \tag{1.5}$$

Where, T is the temperature, k is the Boltzmann constant, R_{sc} is the shunt resistance of the photodetector. Here, i_{shot} and $i_{thermal}$ is the shot and thermal noise of the photodetector, respectively. These two noise cur- rent can be determined by dark current, shunt resistance and bandwidth. Shot noise and thermal noise the main source for the noise in a photodetec- tor. Although to determine the whole noise current steady-state electrical measurement or frequency dependent measurement is needed.

(f) **Noise equivalent power (NEP)**: The minimum amount of detectable signal at a signal-to-ratio of 1 for a 1 Hz bandwidth of a photodetector is known as NEP (in units of $\frac{W}{\sqrt{Hz}}$) responsivity, whereas directly proportional to noise current of the photodetector. NEP of can be expressed in Equation. 1.6.

$$NEP = \frac{i_{noise}}{R} \tag{1.6}$$

(g) **Specific Detectivity (D^*)**: One of the important figure of merit of a photodetector is specific detectivity (D^*, in units of cm. $\sqrt{Hz/W}$ or Jones) of the photodetector which explains how much sensitive a photodetector can be on a specific wavelength. The D^* can be expressed in two ways. When the noise current of a photodetector is ignored or neglected Equation 1.7 used in many reports. Figure 1.11 (a) shows D^* values of PbS QPD under different wavelength light.[10]

$$D = \frac{R}{\sqrt{\frac{2eI_{\text{dark}}}{A}}} \tag{1.7}$$

In many reports, noise measurement is very important step to deter- mine the D^*, if the dark current or noise current is very high. On that case, D^* can be expressed as Equation 1.8.

$$D^* = \frac{\sqrt{A}}{NEP} = \frac{R\sqrt{A}}{i_{\text{noise}}} \tag{1.8}$$

(h) **-3dB bandwidth (BW)**: Using the photoresponse speed BW of a photodetector can be calculate. -3dB bandwidth is expressed as Equation. 1.9:[10]

$$-3d\ Bbandwidth = \frac{0.35}{t_r} \tag{1.9}$$

Where, t_r is the rise time of the photodetector due to incident light illumination. Figure 1.11 (e)-(f) shown BW of the PbS CQD based photodetector values vs different incident light densities and voltages, respectively.

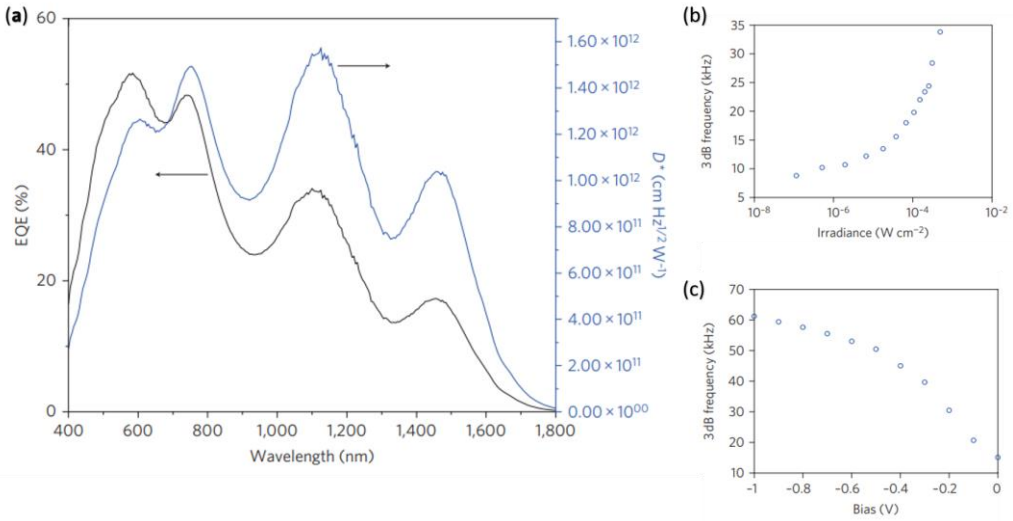

FIGURE 1.11: (a) EQE and D* of PbS QPD under different wavelength of light.[10] (b) illumination light power density[10] and (c) bias voltage dependence -3 dB BW Frequency values. [10]

1.4 RoHS-Compliant Material vs Non-toxic InSb

With increasing demands on the wavelength selectivity to the light of SWIR photodetectors as well as other device performances including responsivity, detectability, and response time, there has also been growing interest in the use of the first exciton peak that appears in the optical absorption spectrum depending on the diameter of the semiconductor quantum dots (QDs). To date, lead- and mercury-based QDs have been vigorously investigated for this purpose, and the SWIR photodiodes with their QDs serving as the light-absorbing layers are known to exhibit high device performances, although there still remain some problems such as high dark current and inherent toxicity of elemental constituents of QDs, which are unsafe for the environment and predominantly limit their applications.[9–14,81,82] Indium antimonide (InSb), a typical III-V direct bandgap semiconductor, exhibits excellent electronic properties including a narrow bandgap (0.17 eV at 300 K), high electron mobility at room temperature (7.7 × 10^4 cm^2/V.s), small effective masses for holes (m_h^* = 0.25m_0) and electrons (m_h^* = 0.014m_0) (where m_0 is free electron mass), low thermal conductivity (0.18 W/cm.°C), small exciton binding energy (0.5 meV), and large exciton Bohr radius (r_B) 60 nm.[83] In this context, the synthesis of InSb nanocrystals in which charged carriers would be strongly confined are attracting a great deal of attention in recent years.[84]

1.4.1 Current situation of Synthesis of InSb CQDs

But there are still a limited number of published papers on their synthesis. Three possible reasons are raised: first, due to the highly covalent nature of InSb, their synthesis requires reactive organometallic precursors compared to II-VI compound semiconductors. Nevertheless, choices of

precursors of indium and antimony are limited at present. Second, due to its strong covalent nature, nucleation and growth of InSb nanocrystals require a high energy field provided at high temperature for the synthetic reaction. Third, post-synthetic purification is still a challenging theme. To synthesize a stoichiometric InSb nanocrystal, the balance between the reduction rates of In and Sb precursors is of importance for co-reduction of both elements. In early studies,[85,86] a pair of tris(trimethylsilyl)-antimony, $(TMS)_3Sb$, and indium acetate was chosen to prepare nanocrystals, but the papers had not shown conclusive data on the formation of the single phase of InSb nanocrystals. Also, $(TMS)_3Sb$ exhibits a stability lower than $(TMS)_3P$ due to its larger anionic radius. Talapin et al. reported the synthesis of InSb nanocrystals without secondary phase and size dependence of the first-exciton peaks in the optical absorption spectra in the SWIR range although $Sb[N(Si(Me)_3)_2]_3$ used as an anion source is violently sensitive to oxygen and thus requires storage in a glovebox freezer at -40 °C or lower.[27] Tris(dimethylamino) antimony, which is available for use in a glovebox filled with inert gas at room temperature, was also concluded to react with $In[N(Si(Me)_3)_2]_3$ or $InCl_3$ as a cation to form a single phase of InSb nanocrystals.[87–89] Kagan et al. reported a heat-up method where $InCl_3$ and $SbCl_3$, which are less reactive to oxygen and water than the other precursors mentioned above, were used as a pair of reactants, but the photodetectors with the resultant InSb nanocrystals showed no response to incident light.[59] Recently, He et al. reported a photodetector with a light-absorbing layer composed of InSb QD and a composite of PCMB and poly-TPD, but its device performance including responsivity was low in the NIR-SWIR region.[90] All the synthesis conditions are showed below in Table 1.1:

TABLE 1.1: Reported synthesis condition for InSb CQDs

Precursor for Indium	Precursor for Antimony	Solvent and Capping agent	Reducing agent	Ref
0.8 mmol of $InCl_3$	0.8 mmol of $Sb[N(Si(Me)_3)_2]_3$	12 ml OLA 3.2 ml of n-trioctylphosphine 5 ml of OA	5 ml of 2M SH solution in DOE	27
0.5 mmol of $In[N(Si(Me)_3)_2]_3$	0.25 mmol of $Sb[NMe_2]_3$	5 ml TOP 0.2 ml of OA		89
0.12 mmol of $In[N(Si(Me)_3)_2]_3$	0.06 mmol of $Sb[NMe_2]_3$	10 ml TOA 6 ml Hexadecane		
3 mmol of Indium Acetate $(In(OA)_3)$	3 mmol of $Sb[NMe_2]_3$	10 ml ODE 9 mmol of OA	3 mmol of BuLi	91
0.125 mmol of $InCl_3$	0.0625 mmol of $Sb[NMe_2]_3$	10 ml of degassed TOA 2 % OA solution	0.18-0.37 mmol of $Li[N(SiMe_3)_2]$ 150 μl of nBuLi (0.37 mmol) 375 μl of SH (0.37 mmol)	88
1 mmol of $InCl_3$	5 mmol of $SbCl_3$	11 ml of OLA 1 ml of OA	1.1 ml of 2M SH solution in DOE	59
0.78 mmol of $InCl_3$	2 ml of Tol 1.86 mmol of OLA 0.78 mmol of $Sb[NMe_2]_3$	10 ml of OLA 1 ml of OA	1.2 mmol of SH in DOE solution	87

1.5 Organization of dissertation

In this thesis, I have studied the synthesise of InSb CQDs by simplify- ing the synthesis precursors and procedure. Later, I have studied and improved the quality of InSb CQD to achieve impurity-less nanocrystal. Further, I have studied the surface modification of InSb CQDs for fabrication of InSb CQD based photodiodes for SWIR sensing.

Chapter 2 focus on the facile synthesis of InSb CQDs with halide precursor. Unlike to previous all the InSb CQDs synthesise reports, the motivation of this study is to synthesis pure phase impurity-less InSb CQDs with less reactive and easily available and stable precursors. I have used chloride and bromide precursors by following hot-injection synthesis pro- cedure. Additionally, I have compared the product prepared by the two precursors.

Chapter 3 focus on the surface modification by ligand exchange procedure. Ligand exchange was performed by different ligands to increase carrier mobility and charge transfer between the CQDs.

Chapter 4 focus on the fabrication of InSb CQD based photodiode for

SWIR sensing. InSb CQD with different ligand device were prepared. Opto-electrical performances were compared for further applications in the field of SWIR sensing.

Chapter 5 proposes future work and development on the InSb CQD based p-n photodiode where InSb CQD can be doped from n-type to p-type and concludes the thesis.

Chapter 2

Synthesise of InSb QD

2.1 Synthesis of InSb QD by Halide precursor

Previously, studies on synthesizing InSb QDs were more focused on highly reactive precursors. But recently, the trend focused on synthesizing InSb QDs with safer and more easily available precursors (such as halogen pre- cursor) with more feasible handling processes. Here, I report a general and straightforward method for the synthesis of pure InSb QDs by super- hydride reduction of InX_3 and SbX_3 (X = Cl, Br) in OLA at high temperature. I showed the facile synthetic route toward pure InSb QDs with- out any secondary metallic phases by using bromine precursors. Further, to continue with Br_3 precursors, by controlling the synthesis parameters, OLA-capped InSb QDs with three different average diameters were obtained. The appearance of the first-exciton absorption peaks suggested the confinement of carriers photogenerated in their nanocrystals. Next, the terminal ligand of the OLA molecules was replaced with a small counterpart. The resultant QDs were used to fabricate the first-ever InSb QD- based photodiode (InSb-QPD) for SWIR light detection, which is operable even at a bias voltage of 0 V in ambient air.

2.1.1 Preparation of Precursor Solution

InX_3 (X = Cl, Br) and SbX_3 were dissolved together in 10 mL of OLA, which was preliminarily degassed in a vacuum overnight, in a rubber stopper plastic sealed glass bottle inside of a glovebox filled with Ar. Then, the sealed glass bottle was heated overnight at 50 °C in an oil bath. The amount of InX_3 was varied between 0.20 and 0.28 mmol, while the amount of SbX_3 was fixed at 0.20 mmol.

2.1.2 Preparation of Reducing Agent Solution

Here, 2.5 mL of LiET3BH (superhydride, SH) solution was mixed with 2.5 mL of DOE, which was preliminarily degassed under vacuum overnight, in a 25 mL two-necked flask connected to an air-free Schlenk line, followed by evacuation at room temperature overnight to remove THF, yielding a DOE solution of SH. Because SH is highly reactive and sensitive to air, I treated SH in a vacuum glovebox where water and oxygen were kept below 1 ppm.

2.1.3 Synthesis and Purification of OLA-Capped InSb QD

InSb QDs were synthesized by a hot-injection method using a Schlenk line under Ar gas flow. First, 10 mL of OLA, which was preliminary degassed under vacuum overnight, was added to a three-necked flask under constant stirring, and then, the flask was heated to 240 °C. A 2.5 mL portion of the SH solution was added to the flask at 240 °C. The solution color became pale yellow within minutes. The In-Sb precursor solution was injected drop-by-drop over a 5-minute period. Upon injection, the precursor solution turned dark brown. When the predetermined reaction time was reached, the reaction solution was transferred into a rubber stopper

SCHEME 2.1: Scheme for Colloidal Synthesis of InSb QDs by Hot-Injection Method

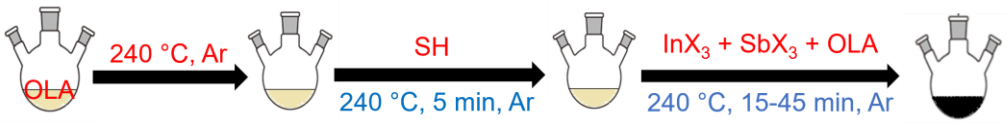

plastic sealed glass bottle containing 12 mL of toluene via a glass syringe technique for quenching the reaction. The mixture was separated into two centrifuge tubes capped with septa of 50 mL each. Centrifugation for 5 min at 8000 rpm yielded a black precipitate and a brown supernatant solution. Next, the precipitate was dispersed in 8 mL of hexane as a solvent while 8 mL of methanol was added as antisolvent, followed by centrifugation for 10 min at 10,000 rpm. I obtained a black precipitate and transparent supernatant. The transparent supernatant was discarded, and the precipitate was placed under a vacuum and dried overnight.

2.1.4 Synthesis and Characterization of OLA-Capped InSb QDs

The experimental procedure for synthesizing the OLA-capped InSb QDs in powder form on the scale of hundreds of milligrams is shown in Scheme 2.1.

The synthesis was based on a hot-injection method and electric reduction of halide salts of indium and antimony with SH on a conventional setup equipped with a Schlenk line. In a typical experiment, 2.5 mL of 1.0 M SH in DOE was injected into 10 mL of OLA in a three-necked flask heated at 240 °C. A mixture of InX_3 and SbX_3, which were previously stirred in 10 mL of OLA at 50 °C overnight for making a pale yellow solution shown in Figure 2.1 (a), was injected into the flask using the Hamilton

gastight syringe technique. Upon addition, the color of the reaction solution changed to black from pale yellow, as shown in Figure 2.1 (b).

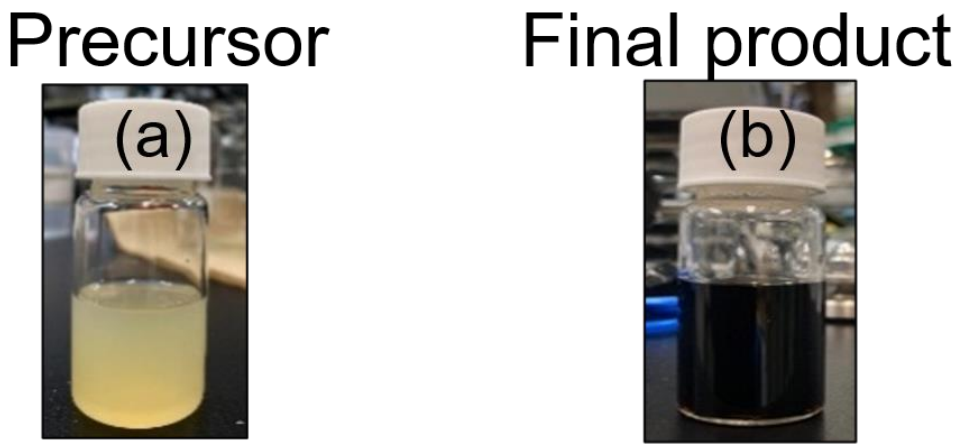

FIGURE 2.1: Images of (a) precursor solution of $InBr_3$, $SbBr_3$ in OLA,(b) precursor solution after SH reaction.

The In/Sb molar ratio was varied to find suitable conditions to synthesize a pure crystalline InSb without a secondary phase or impurity. When the reaction had reacted for the predefined time, the heater was removed. The reaction solution was then immediately extracted with a glass syringe and mixed with toluene in a glass bottle. As a result, the reaction was forced to be stopped by dropping the temperature (quench). Once the solution had dropped to room temperature, it was transferred to an Ar gas-filled centrifuge tube with a septum cap and was immediately processed for precipitation (probably within ∼30 s). As a control experiment, I observed that increasing the extraction time (∼30 s to 10 min) of the reaction mixture to toluene leads to increasing the mean size and broadening the size distribution of the product significantly (see Figure 2.2, XRD and TEM images of different samples prepared with different extraction times) be- cause of aggregation of QDs. Finally, the precipitated product was dried overnight under vacuum conditions. The dried product was not an oily

product but a solid as evidenced in Figure 2.3 (a). In addition, the solid in powder form was easily re-dispersed in hexane. As evidenced in Figure 2.3 (b), the dispersity of the product in hexane was extremely high even at a concentration of 100 mg/mL, possibly due to the high packing density of the OLA ligand bound to the InSb surface as described later.

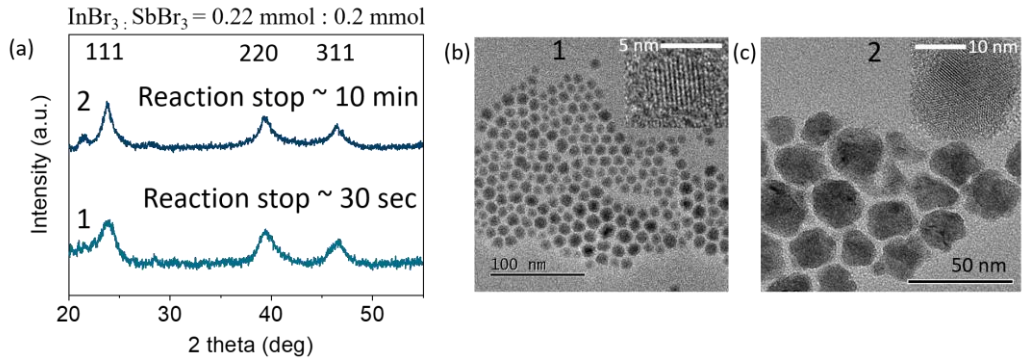

FIGURE 2.2: XRD pattern of the product synthesized with prepared at 240°C for 15 min at a molar ratio of $InBr_3/SbBr_3$ = 0.22:0.2 with a different reaction stopping time, HR-TEM images of the respective products where reaction sample was mixed with toluene on different timing to stop the reaction (b) after 30 sec (c) after 10 min. The insets show the enlarged images.

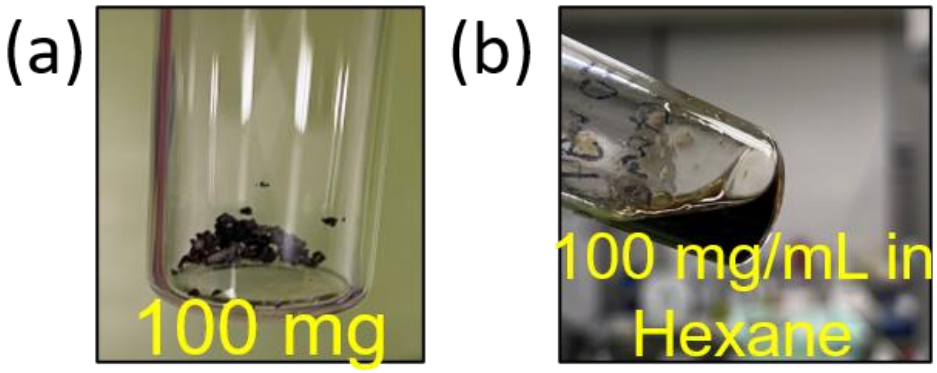

FIGURE 2.3: Digital photographs of (a) the dried product and (b) hexane solution of the product with 100 mg/mL concentration.

Comparison Study of Product Obtain Through Chloride and Bromide Precursors

An XRD study has revealed the optimal conditions to obtain a pure phase of cubic InSb nanocrystals free of metallic antimony and indium and/or other crystalline phases derived from their oxides and hydroxides. Figure 2.4 (a) and (b) show XRD patterns of the samples prepared from the $InCl_3$-$SbCl_3$ and $InBr_3$-$SbBr_3$ pairs, respectively. The In/Sb molar ratios of precursors varied between 1.0 and 1.4 for the chlorides and between 1.0 and 1.25 for the bromides. The reaction time was fixed to 15 min at 240 °C in every case because above 230 °C the reduction rate of both In and Sb precursors is sufficiently fast to allow co-reduction of both elements.[87] In Figure 2.4 (a), once the molar ratio of the precursor is set to 1:1, three peaks appearing at 2θ = 23.8°, 39.3°, and 46.3° are characteristic of (111), (220), and (311) planes of the zinc blende InSb structure, respectively. Whereas there are small peaks at 28.8°, 40.0°, 41.9°, and 51.8° attributed to (012), (104), (110), and (202) planes of metallic antimony as a secondary phase, while the intensity of these peaks weakens with increasing molar ratio. A further increase in the molar ratio showed the appearance of metallic indium as a secondary phase instead of the absence of antimony. As exemplified in these diffraction patterns, I could not obtain an InSb single-phase sample. On the other hand, I obtained a good result upon the synthesis using an $InBr_3$-$SbBr_3$ pair. As shown in Figure 2.4 (b), using a 1.0 molar ratio of precursor, I confirmed the formation of metallic antimony as a secondary phase in addition to the cubic InSb phase. The absence of the secondary phase was observed only once, and the In/Sb molar ratio was set to 1.1. As the molar ratio was

further increased, the diffraction peak attributed to the In(101) phase appeared. Comparison of the XRD patterns shows that the diffraction peaks are narrower for the samples prepared from the chlorides than from the bromides, possibly due to the increase in diameter of the nanocrystals. This could be relevant to the fact that the presence of bromide significantly reduces the reduction potential compared to chloride in the case of metal halides.[92,93] In other words, chlorides react faster than bromides and may therefore yield QDs of larger sizes. EDS-STEM spectra shown in Figure 2.4 (c) and (d) confirmed the presence of indium and antimony in the samples prepared from the molar ratio of 1.25 for the chlorides and 1.1 for the bromides, respectively. According to the spectral analysis in Figure 2.4 (d), the sample contains 52.5% indium and 47.5% antimony, nearly corresponding to the precursor ratio. The ratio of indium to antimony is almost unity, with little deviation from the stoichiometric composition, and consistent with the result of XRD characterization. Microstructures of both samples were investigated by HR-TEM and EDS-STEM elemental mapping. Figure 2.4 (e) shows a typical high-resolution image and the result of elemental mapping of the sample prepared from the chlorides. InSb nanocrystals observed are in-homogeneously distributed and agglomerated. Whereas with the bromide-derived sample, spherical-shaped InSb nanocrystals are highly distributed without aggregation but have a broad size distribution (see Figure 2.4 (f)). Hereafter, for further characterization, I used InSb nanocrystals prepared with a molar ratio of $InBr_3$:$SbBr_3$ = 0.22:0.2.

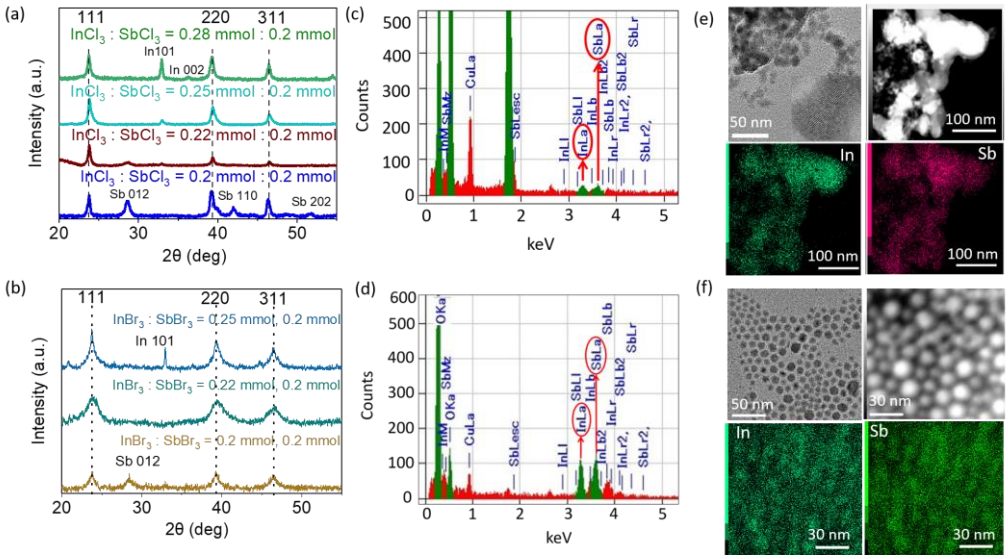

FIGURE 2.4: XRD patterns of the products prepared at 240 °C for 15 min with different (a) $InCl_3/SbCl_3$ and (b) $InBr_3/SbBr_3$ molar ratios. EDX spectroscopic profiles of the products prepared at 240 °C for 15 min with the molar ratios of (c) $InCl_3/SbCl_3$ = 0.25:0.2 and (d) $InBr_3/SbBr_3$ = 0.22:0.2. HR-TEM image and STEM-EDS maps of (e) $InCl_3/SbCl_3$ = 0.25:0.2 and (f) $InBr_3/SbBr_3$ = 0.22:0.2.

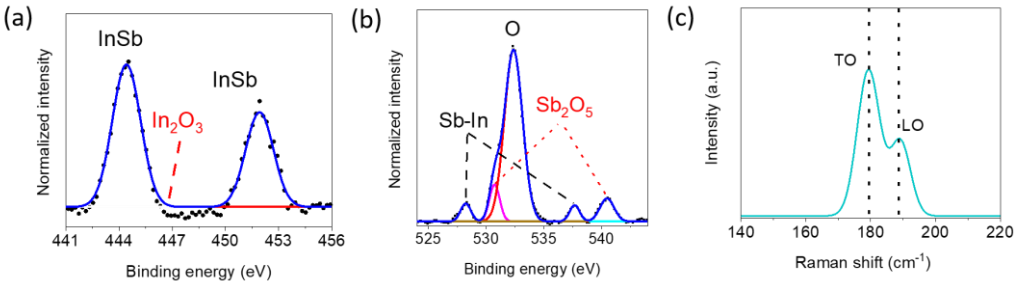

FIGURE 2.5: XPS (a) In 3d and (b) Sb 3d spectra, fitted with Gaussian functions, and (c) Raman spectrum of the product prepared at 240 °C for 15 min with a molar ratio of $InBr_3$:$SbBr_3$ = 0.22:0.2

Surface characterization of InSb CQDs

The representative XPS spectra of the sample are shown in Figure 2.5. The In 3D core level spectrum exhibits the In-Sb bond identified at a binding energy of 444.5 eV for In 3d5/2 (see Figure 2.5 (a)), consistent with

data for InSb bulk and QD.[88,94] I also see no other electronic states of indium compounds such as In_2O_3 that are known to give the In 3d5/2 peak at ~446.4 eV.[88] The XPS spectra of Sb 3d and O 1s are usually overlapped but could be de-convoluted to the O 1s component and Sb 3d counterpart (see Figure 2.5 (b)). The Sb 3d5/2 peak was found at binding energies of 528.2 eV that is assigned to the In-Sb bond of the bulk InSb crystal.[94] The Sb 3d core level spectrum shows the presence of oxidized Sb compounds such as Sb_2O_5 which is known to give the Sb 3d5/2 peak at 530.5 eV.[95] It is broadly known that crystalline InSb is prone to oxidation due to its highly oxophilic nature of both indium (binding energy, In-O 360 kJ/mol) and antimony (binding energy, Sb-O 372 kJ/mol).[88] In our purification process, the InSb nanocrystals were strictly washed many times to remove organics that might be physically adsorbed on their surfaces and obtain the product in powder form. The surface oxidation might occur during the purification process. A typical Raman spectrum is shown in Figure 2.5 (c). The sample was excited by a 532.3 nm line of a monochromatic Raman laser, and the average power density on the sample was about 0.42 mW to give the spectrum. Two well-resolved peaks corresponding to transverse optics (TO) and longitudinal optics (LO) appeared at 179.5 and 188.8 cm^{-1}. Com- pared to bulk InSb, the TO and LO peaks have a blueshift toward higher frequency by 1.3 and 0.8 cm^{-1} respectively. Frequencies of TO and LO modes of nanocrystals with diameters more than 10 nm were the same as the bulk crystal. The appearance of a blue shift might be due to the influ- ence of a strong phonon confinement effect and strain in the nanocrystals smaller than 10 nm. Also, I see the absence of the peak at 145 cm^{-1} attributed to the amorphous InSb phase.[96–98]

2.1.5 Optical Properties of OLA-Capped InSb QDs

To control the average size of InSb nanocrystals, the reaction time was varied between 15 to 45 min at 240 °C, while the In/ Sb molar ratio of the precursor was set to 0.22:0.20 mmol. Samples prepared with reaction times of 15, 30, and 45 min are labeled A, B, and C in Figure 2.6 (a). As predicted from the results in Figure 2.4, these three samples are composed of a cubic InSb crystalline structure that does not contain any other phases. The diffraction peaks become narrower as the reaction time increases, indicating that the diameter of the InSb nanocrystals increases as the reaction time increases. HR-TEM images shown in Figure 2.6 (b-d) demonstrate the dots are round-shaped nanocrystals. Figure 2.6 (e) shows the variation of size distribution as the reaction time increases. The chemical compositions of InSb nanocrystals displayed were confirmed to be nearly stoichiometric by EDS-STEM mapping analysis. The estimated average diameters of samples A, B, and C were 5.1 ± 1.1, 7.8 ± 1.3, and 12 ± 1.8 nm, respectively. Once the reaction time was extended to 60 min, the nanocrystals grew to ∼20 nm in diameter and aggregated with each other (see Figure 2.7, TEM image of nanocrystals reacted ∼60 min).

Optical absorption spectra of samples A, B, and C in solution form are shown in Figure 2.6 (f-h), respectively. I could see no sharp first-exciton peaks in the absorption spectra, but tiny humps as a shoulder were observed at around 1200 and 1400 nm for samples A and B, respectively. These exciton characteristics could be also seen for samples A and B in thin film form (see Figure 2.8, UV-vis-NIR absorption spectra). There are no excitonic characteristics for sample C. There are two possible reasons. First, in the region from 1700 to 1800 nm, the presence of organic ligands might suppress the observation of such a tiny hump. Second, compared

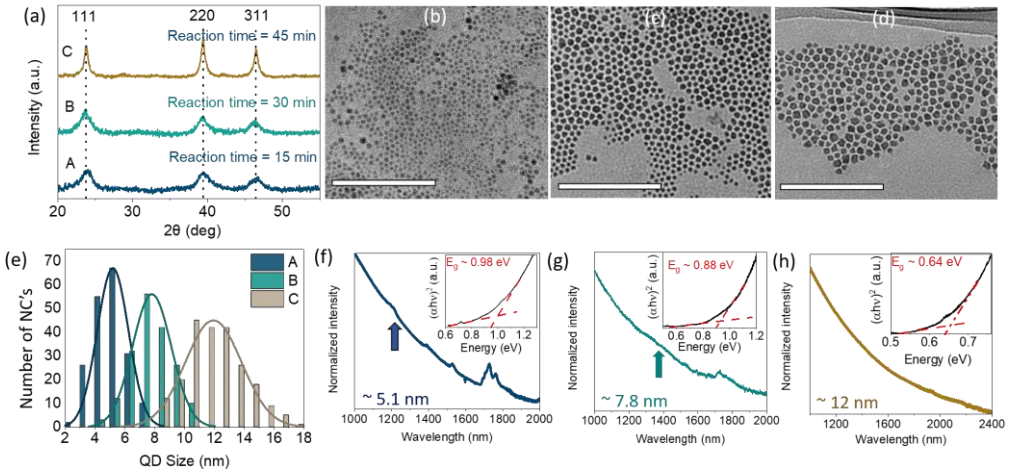

FIGURE 2.6: (a) XRD patterns of the products at a molar ratio of In:Sb = 0.22:0.2 and varying reaction time. HR-TEM images of sample A (b), sample B (c), and sample C (d). Scale bars indicate 200 nm. (e) Size distribution profiles of samples A, B, and C were obtained by measuring the dot size in the images (a), (b), and (c). Tauc plots (inset) and room-temperature NIR absorption spectra of the (f) sample A (d = 5.1 nm), (g) sample B (d = 7.8 nm), and (h) sample C (d = 12 nm).

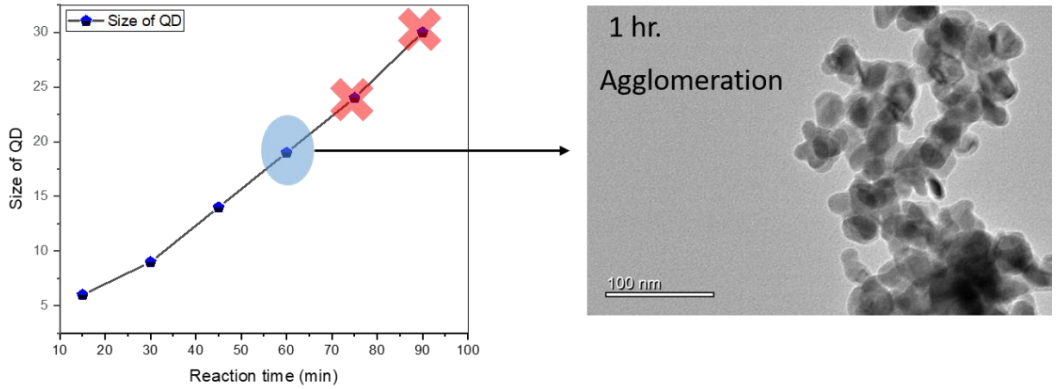

FIGURE 2.7: Measured diameters of InSb QDs synthesized at 240°C for different reaction times (Left) and a typical HR-TEM image of the sample prepared at 60 min of reaction time (Right).

to samples A and B, the diameter of nanocrystals in sample C is too large to strengthen the confinement of photoexcited carriers, resulting in weakened exciton characteristics.

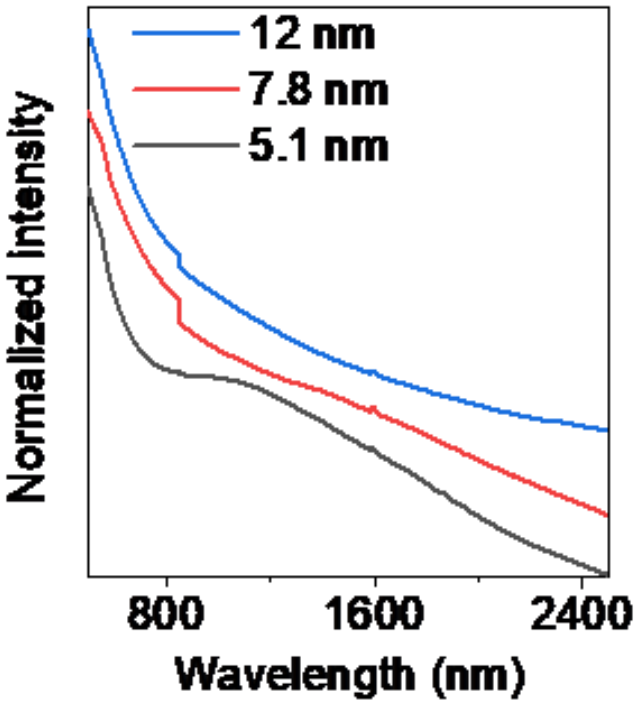

FIGURE 2.8: Room-temperature UV-VIS-NIR absorption spectra of OLA capped sample A (d =5.1 nm), B (d = 7.8 nm) and C (d = 12 nm) in thin film form after centrifugation at 10000 rpm for 10 min and dried on the hot plate at 120 °C.

Tauc plot extrapolation has been employed to extract the bandgap energies of various semiconductor QDs.[99] In the inset of Figure 2.6 (f-h), Tauc plots of $(\alpha h\nu)^2$ versus photon energy are shown for the samples, and the experimental values of bandgap were estimated to be 0.98 0.88, and 0.64 eV, respectively. The bandgaps of samples A and B nearly correspond in magnitude to the positions of the humps in absorption spectra. The broadening of excitonic bands is probably due to the ensemble size polydispersity of the nanocrystals, consistent with the broad size distribution as plotted in Figure 2.6 (e). EMA equation 1.1 is used to investigate the size-dependent bandgap (E_g) of semiconductors.[24] The theoretical relationship between nanocrystal size and E_g was calculated by EMA as well as our experimental plots shown in Figure 2.9, bandgap approximation plot with corresponding synthesized QDs).

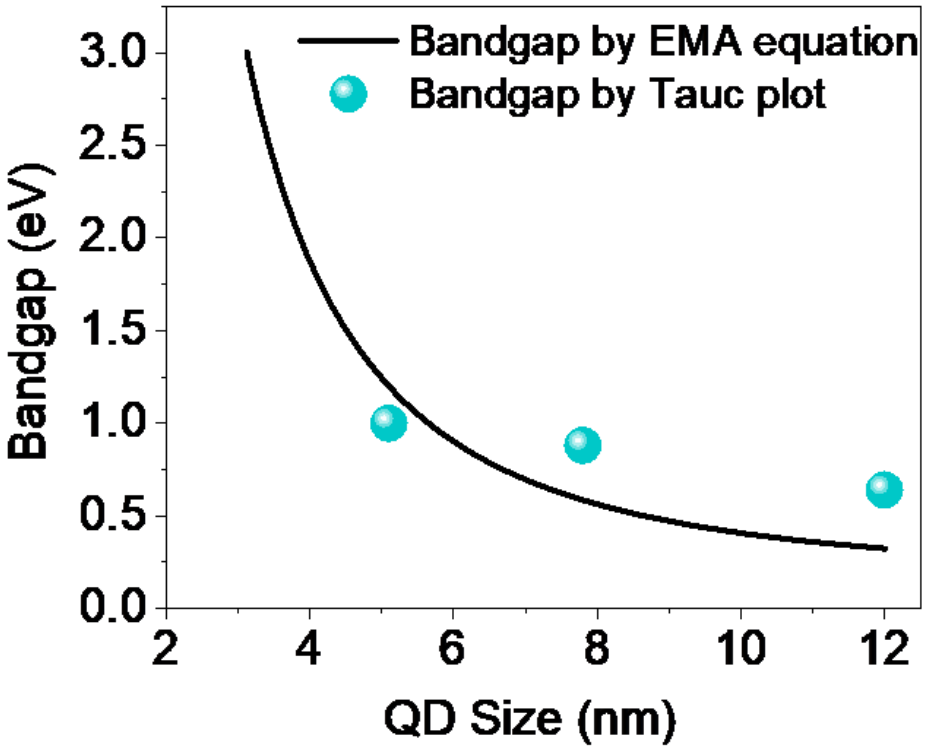

FIGURE 2.9: Bandgap energies plotted versus the InSb QD diameter, in which the solid curve shows the theoretical relationship between the values of E(d) calculated using the EMA and the diameters of QDs. Experimental values for the samples A-C.

Comparing the optical bandgap attributed to the experiment with the theoretical relationship, I found that EMA prediction provides an accurate trend for bigger QDs, while overestimated for smaller particles (~5 nm). This the discrepancy is already reported earlier for InSb and other low bandgap materials. There can be various reasons such as underestimated leakage of the wave functions into the surrounding medium or band structure beyond Γ; the valley cannot be ignored during the experiment unlike in the theoretical model.[27] Another possible reason could be that the size dependences of the bandgaps of the QDs not only depended on $1/R_2$ (quantum confinement effect) but also depend on 1/ R (electron and hole Coulomb interaction) which has been neglected in parabolic

EMA.[87,100,101] Nevertheless, the magnitude of the optical bandgap increases with a reduction in diameter of InSb QDs based on the effect of quantum confinement, suggesting that the wavelengths of the first exciton peak can be tuned from 1200 to 1400 nm by adjusting the QD size between 5.1 and 7.8 nm on the assumption that the size distribution should be narrowed with a relative the standard deviation of 10%.

In conclusion to this section, the synthesis was performed in the presence of super- hydride by the hot-injection method using bromides of indium and antimony, which are chemically stable and commercially available precursors and can be handled in a conventional laboratory environment. The resulting InSb QDs were capped with OLA and showed high solubility in non-polar solvents, even at concentrations as high as 100 mg/moL. The bandgap was tuned between 0.64 and 0.98 eV depending on the QD diameter.

2.2 Size-selective Precipitation Technique

Herein, I have improved synthesis by leveraging our previous report with modified parameters to revamp the optical properties of the InSb CQDs. I performed the size separation of the synthesized CQDs to obtain the narrow distribution of the CQDs. Obtained CQDs with different diameters showed significant absorption and band-edge emission from NIR to SWIR. In our current study, QDs achieved photoluminescence at room temperature which justifies the improved quality of InSb CQDs.

SCHEME 2.2: Scheme for size separation

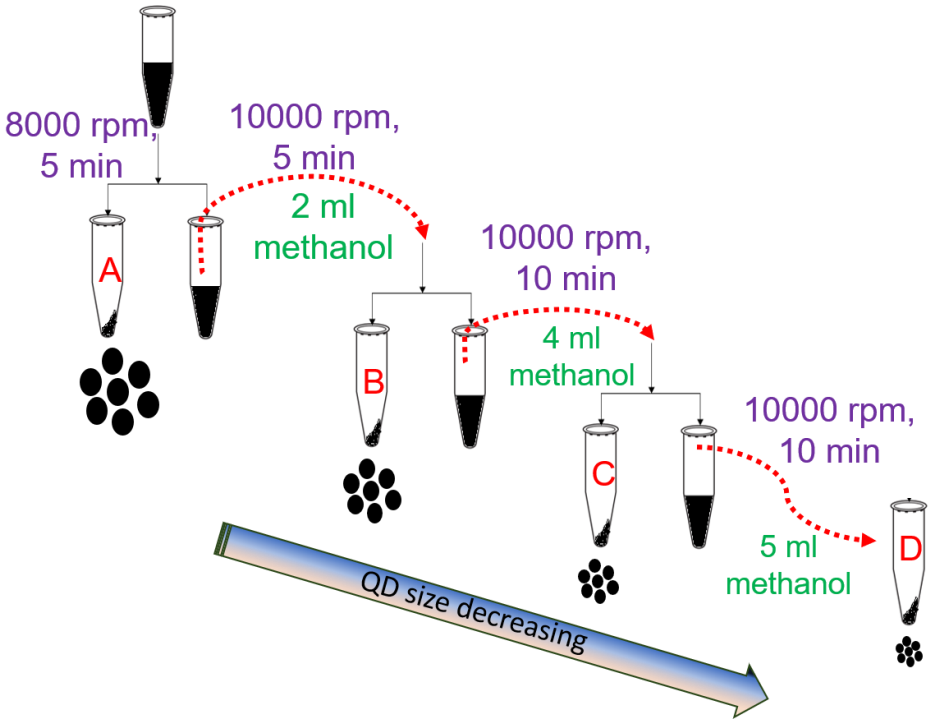

2.2.1 Size Separation Precipitation

I started the synthesis by considering concentration of super hydride (SH) as a reducing agent and a molecular ratio of In/Sb precursors to suppress oxidation of resulting CQDs during synthesis and formation of metallic antimony which were difficulties to solve.[52,59,91] The optimized volume ratio of oleylamine (OLA) as solvent with SH was 5.2 (see Experimental section). Scheme 2.2 illustrates a size separation procedure that involves four-step centrifugation to narrow the size distribution of CQDs. Samples obtained in each step are labelled as A, B, C and D.

2.2.2 Structure and Surface Characterization of OLA-capped InSb QDs

I performed several experiments to confirm the synthesis of high-crystalline, non-oxidized colloidal InSb QDs. Analysis of the powder X-ray diffraction (XRD) patterns shown in Figure 2.10a confirms that samples A-D are pure phase zinc blende structures, without any secondary phases present. The diffraction peaks centered at 2θ = 23.8°, 39.3° and 46.3° are characteristic of (111), (220) and (311) planes, respectively. The broad peak at 21.52° can be attributed to the excess amounts of organics remaining in sample D.[102] The diffraction peaks broadened with the incremental addition of methanol as antisolvent in the centrifugation process, suggesting the decrease in the average diameter of QDs. Figure 2.10b and 2.10c shows the representative X-ray photoelectron spectroscopic (XPS) spectra corresponding to the core levels of In3d and Sb3d, respectively. Panel (b) shows the chemical bonding state in which In is bound to Sb and not to oxygen, consistent with the literature.[52] In Panel (c), the overlapped XPS spectra of Sb3d and O1s core levels were deconvoluted as the dotted line. Sb 3d5/2 and Sb 3d3/2 peaks were assigned to In-Sb bond at binding energies of 528.2 eV and 537.6 eV.[94,95] Besides, the absence of a peak at 540.4 eV indicates that there is no Sb-O component. Inductively coupled plasma mass spectrometric (ICP-OES) study confirmed an In:Sb ratio of 1:1. These structural analyses indicated that the stoichiometric InSb QDs having the high crystalline degree and no surface oxidation were synthesized as the SH concentration in the feed solution was increased. HR-TEM images of samples A, B, C, and D are shown in Figure 2.11 (a), Figure 2.10 (d), Figure 2.11 (d), Figure 2.12, respectively. In common with all samples, the QDs having spherical shapes were isolated and dispersed without aggregation, suggesting that their surfaces are terminated

with OLA molecules. The estimated diameters were 17 ± 2.9 nm, 8.7 ± 1.2 nm, 4.8 ± 0.7 nm, and 2.6 ± 0.4 nm for samples A, B, C, and D, respectively. The centrifugation process with stepwise addition of methanol allowed fractionation of the mother sample into a relatively narrow polydispersity (standard deviation, = 25-27%) sub-ensemble.

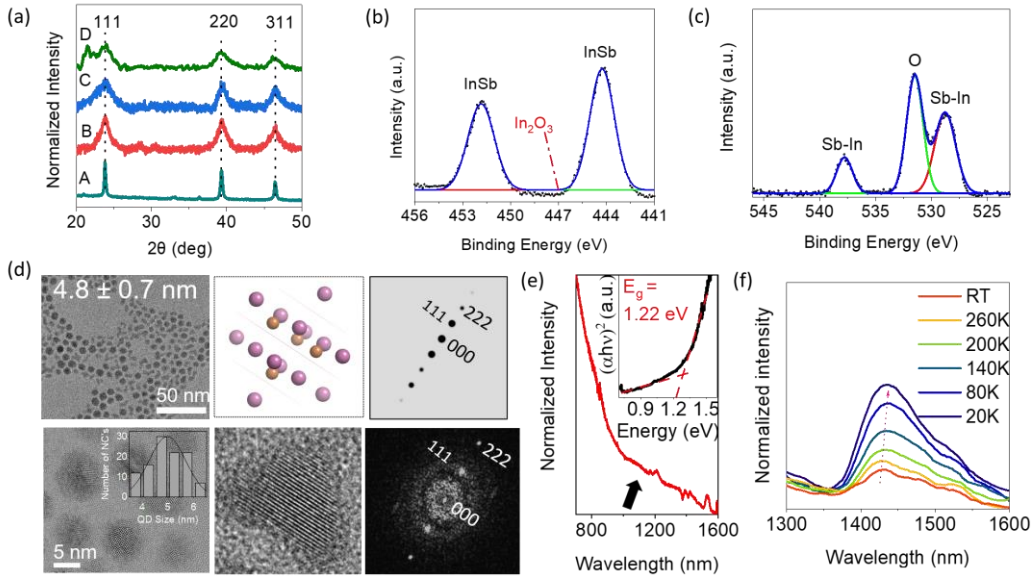

FIGURE 2.10: (a) Powder XRD patterns of the products prepared with different centrifugation processes; detailed scheme can be found in Scheme 2.2. XPS spectra of the of the sample C (b) In 3d and (c) Sb 3d regions, fitted with Gaussian function. (d) HR-TEM images of sample C with the size distribution profile in the inset. (e) Normalized absorption spectra of sample C in TCE at room temperature. (f) Low-temperature PL spectra of the sample C.

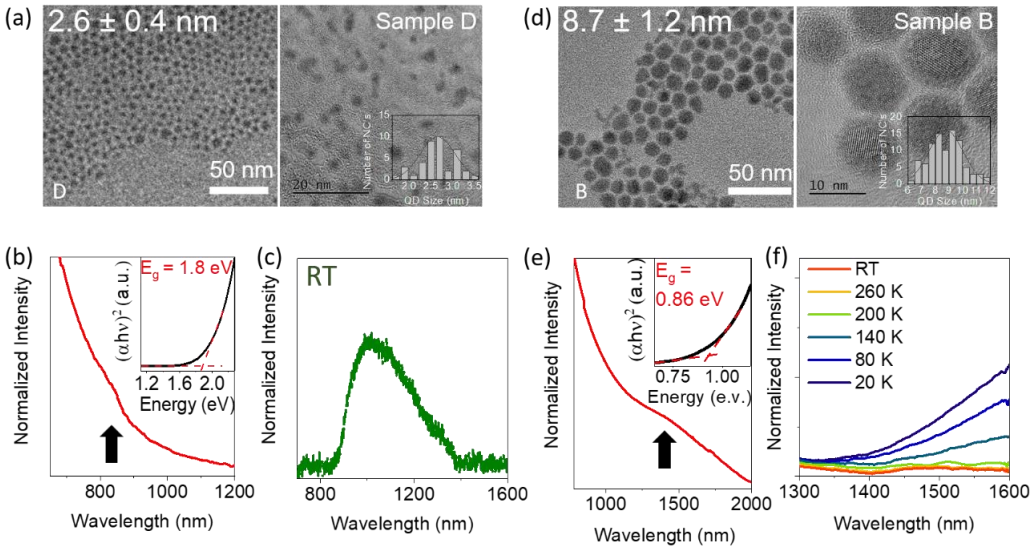

FIGURE 2.11: (a), (b), (c) TEM image, absorption spectra and room temperature PL spectra of InSb QD sample with smallest size obtained by size selective procedure respectively, which has been labeled as 'sample D'. (d), (e), (f) TEM image, absorption spectra and low temperature PL spectra of InSb QD sample respectively labeled as 'sample B'.

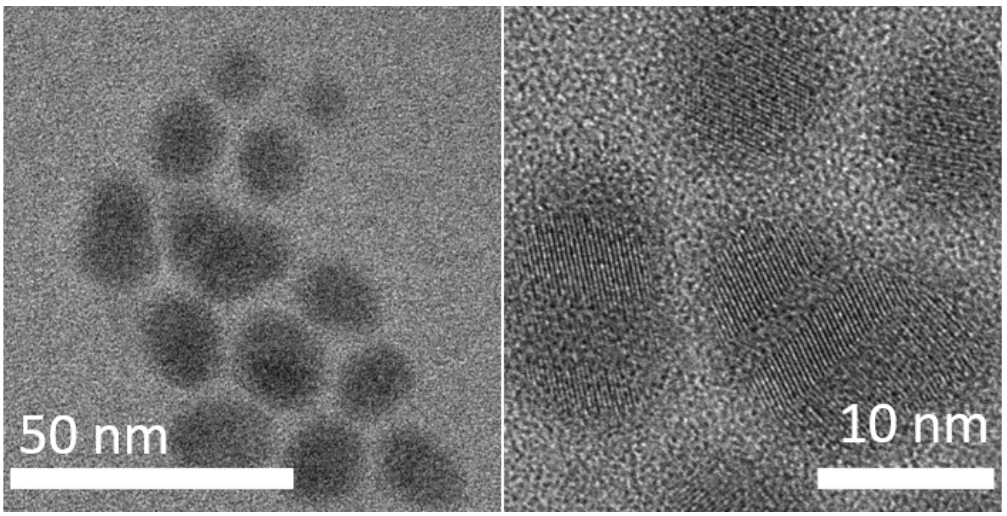

FIGURE 2.12: TEM image of bigger size InSb QD obtained by size selective procedure which has been labeled as 'sample A'.

2.2.3 Optical properties of OLA-capped InSb QDs

Optical properties were investigated to understand the relationship between QD size and optical bandgap. The NIR absorption spectrum of samples C is presented in Figure 2.10 (e) while the spectra for samples B and D are shown in Figure 2.11 (b) and Figure 2.11 (e). In these spectra, the excitonic peak energy positions are not clear but I can see humps as a shoulder at around 845 nm, 1100 nm, and 1450 nm for samples B, C, and D, respectively. This is probably due to the semi-ensemble size polydispersity of the InSb QDs in the σ = 25-27% range, consistent with the literature.[87] As will be discussed in the latter of this paragraph, the hump shape becomes more obscured as a shoulder in the region of smaller QD size. On the other hand, no characteristic peak was observed in sample A, even though the diameter of the QDs is considerably smaller than the Bohr radius of the bulk exciton. Indeed, the appearance of the first excitonic peak in the absorbance spectrum is limited in the literature to cases where the diameter of the QD is smaller than 7 nm,[27,59,87] suggesting that a 17 ± 2.9 nm diameter is too large to generate the quantum confinement effect. Tauc plots from which optical bandgap energy can be determined are shown in the inset of Figures 2.10 (e), Figure 2.11 (b) and Figure 2.11 (e) for each sample. The estimated values were 0.86 eV, 1.22 eV, and 1.60 eV for the 8.7-nm, 4.8-nm and 2.6-nm diameter QDs, respectively. To facilitate a quantitative comparison of size-dependent bandgaps, our experimental data were plotted along with reported values and theoretical relationships calculated by effective mass approximation (EMA, see Figure 2.13).[24] The calculated EMA model indicates that the bandgap increases slowly in the range of QD diameters larger than 6 nm but increases rapidly in the range of QD diameters smaller than 5 nm. For the d < 5nm, even relatively small size deviations can cause a large shift in

photon energy of exciton absorption, yielding a spectral broadening. In other words, the σ = 25-27% of standard deviation is too large to generate the distinct exciton peaks in the absorption spectra for samples C and D. Conversely, for QDs larger than 8 nm in diameter (i.e., sample B), the band gap variation with QD size is small. Thus, the standard deviation of σ = 25-27% is small enough to produce a distinctly shaped hump implying exciton absorption. Now, the bandgap calculated with EMA showed an overestimated trend compared to the bandgap attributed to experimental values in the 2-6 nm size regime. Similar trends with InSb CQDs have been reported before.[27,87] Possible mechanisms are underestimated leakage of the wave functions into adjacent mediums or beyond the band structure and the dependency of 1/R of coulomb interaction which has been ignored during EMA calculation.[27,87100,101]

Photoluminescence (PL) spectra of the samples B, C and D are shown in Figure 2.11 (c), Figures 2.10 (f), and Figure 2.11 (f), respectively. As expected from the prediction of EMA, PL spectral peak position was varied from 1015 nm to 1445 nm by tuning the diameter of QDs from 2.6 ± 0.4 nm to 4.8 ± 0.7 nm. Such a large Stokes shift between the excitonic absorption and PL peak is commonly observed for InSb QD and discussed resulting from the presence of internal defect states or polydispersity of CQDs in the system.[103] PL spectra of the samples C and D were observed at room temperature, but the spectral intensity became weak for smaller in size of QD. Although the limited wavelength range of the SWIR detector did not allow us to detect the exact PL peak in sample B, it is particularly noteworthy that the 8.7-nm QDs showed for the first time the potential to be emitters with PL peaks at wavelengths longer than 1600 nm (see Figure 2.11 (f)).

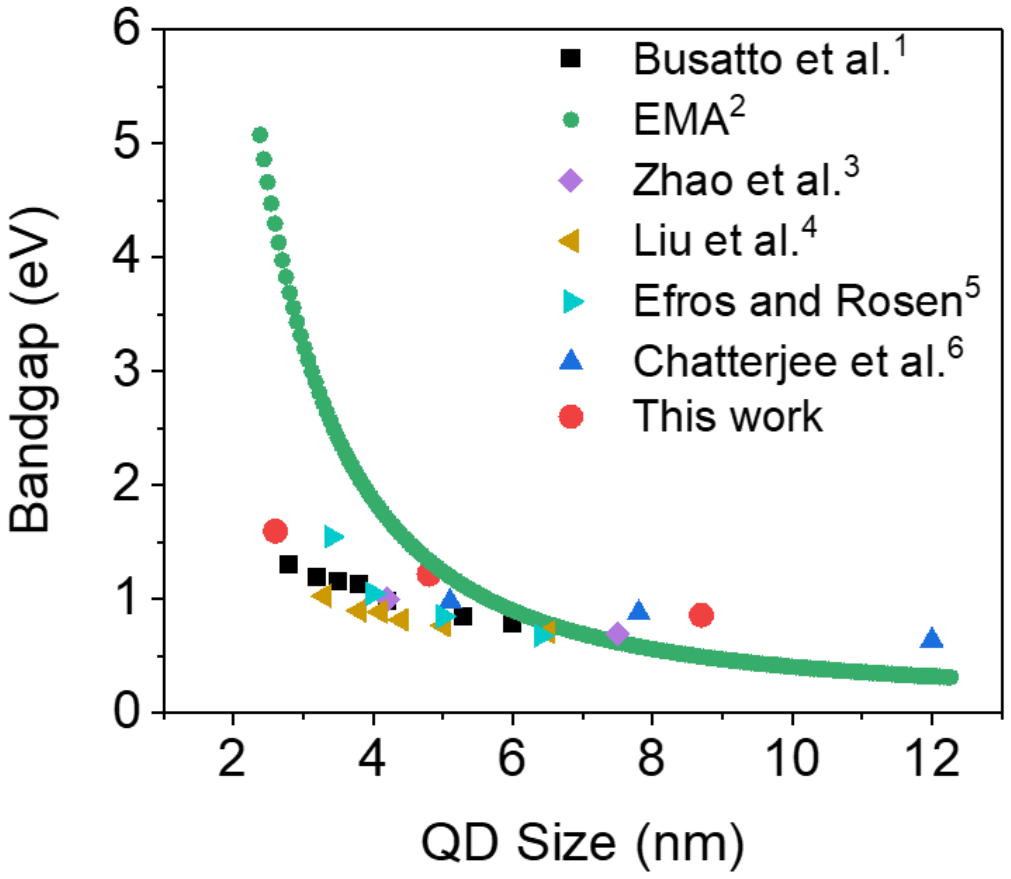

FIGURE 2.13: Bandgap energies plotted versus the InSb QD diameter, solid curve shows the theoretical relationship between the values of E_g calculated using EMA and the diameters of QDs. Prepared QDs has been compared with our previous work.

2.3 Conclusion

In summary, I have modified the synthesised route to achieve pure InSb CQDs with easily available bromide precursors which eventually ascribed no surface oxidation on QD surface. This is the first report on no-oxidation on surface for both In and Sb element among all the previously reported InSb CQD literature. Additionally, size selective precipitation procedure helps to achieve narrower size distribution. Optical properties and bandgap were varied from 840 nm to 1450 nm with 1.8 eV to 0.86 eV, while photoluminescence was achieved from 1015 nm and 1440 nm for QD size 2.6 nm and 4.8 nm respectively.

Chapter 3

Ligand exchange of InSb QD

Solution-phase ligand exchange is a critical step to improve inter-dot coupling, charge transfer, electrical conductivity, and carrier concentration for enhanced optoelectronic device performance. Conventionally, the long chain molecules bound to the QD surface, which stabilize and isolate QDs in organic solvent during synthesis, are replaced with short-chain molecules or ions.

3.1 $InBr_3$ ligand

In this work, I found that the OLA ligand was replaced by an $InBr_3$ counterpart by using a two-phase approach where oleic acid bound to the surface of InAs QD is exchanged by $InBr_3$ ligand shown in Figure 3.1 (a).[72] To perform the exchange, an octane solution of the OLA-capped QDs was introduced to the ligand solution where $InBr_3$-AA was dispersed in a polar solvent such as DMF. Because of the presence of the OLA ligand, the QD was dispersed highly in octane as shown in the glass bottle shown in Figure 3.1 (b), followed by vigorous shaking of the mixture by hand. Once the OLA ligand was exchanged, the QDs were transferred to the DMF phase within minutes, as evidenced in a photograph of the glass bottle as shown in Figure 3.1 (c). The octane phase was removed using a separate funnel.

InSb QDs were highly dispersed in DMF and did not precipitate, even at 50 mg/mL (see Figure 3.1 (d)).

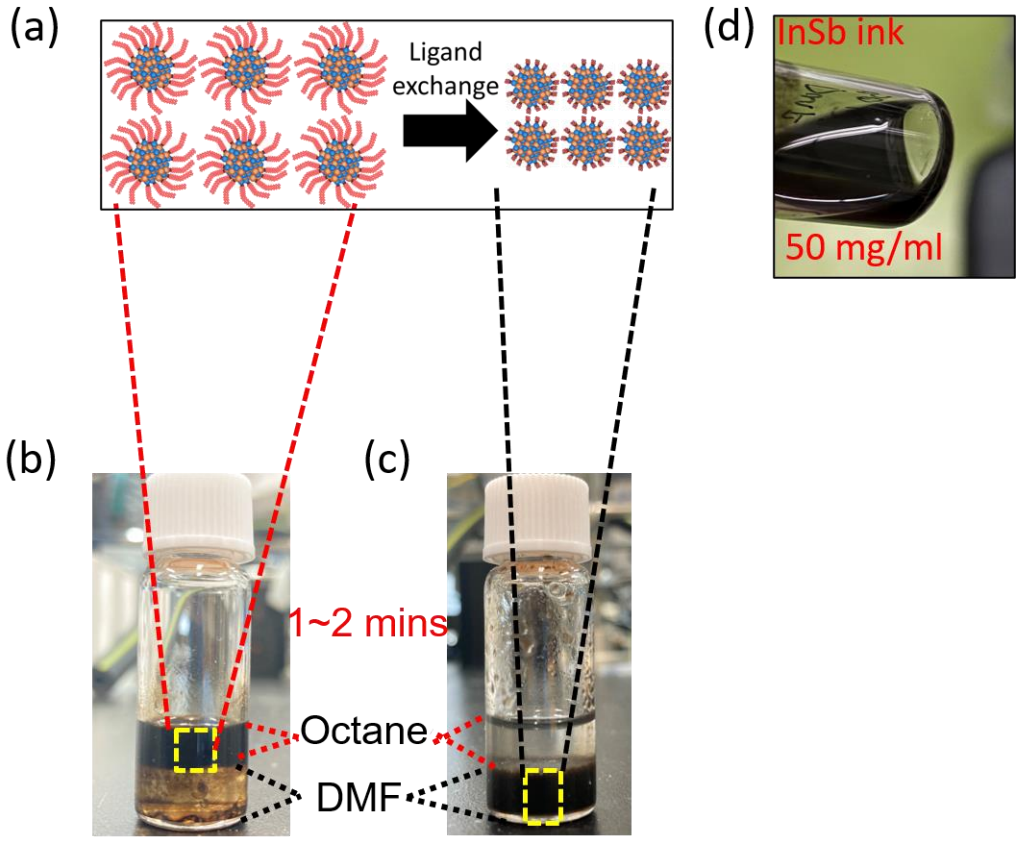

FIGURE 3.1: (a) Scheme of ligand exchange process, Digital photographs of InSb QD phase (b) before and (c) after ligand exchange. (d) Digital photograph of 50 mg/mL InSb QD ink after ligand exchange.

Optical absorption spectra of the ligand-exchanged sample in solution form are shown in Figure 3.2 (a), indicating the excitonic features at around 1200 nm. Further, it suggests the bandgap and sizes of the sample were unchanged after ligand exchange. Figure 3.2 (b), size distribution profile of InSb CQD after ligand exchange. Attachment of Br^- ligands to the surface of the QDs was confirmed by XPS characterization. Figure 3.2 (c) shows the XPS Br 3d spectra of the sample before and after the ligand exchange reaction. Despite using a Br_3 precursor for synthesizing

InSb QDs, there was no signal for bromide in the OLA-capped QD, suggesting the removal of byproduct in the purification process. After ligand exchange, there was a strong signal at 69.3 eV, indicating the presence of $InBr_3$ as a ligand bound to QD surface.[104] Completeness of ligand exchange was also verified by an ATR-FTIR spectroscopic study, as shown in Figure 3.2 (d). Before the QDs were subjected to the ligand exchange step, the sample showed strong absorption bands in the aliphatic C-H stretching region between 2850 and 2960 cm^{-1} and the C-H bending/scissoring region between 1350 and 1500 cm^{-1}.[105] After the ligand exchange, the C-H signatures of OLA disappeared while a single peak at 1653 cm^{-1}, which is attributed to DMF-$InBr_3$ complex,[72] was observed.

To assess the interparticle distance of exchanged QDs I carried out grazing-incidence small-angle X-ray diffraction (GI-XRD) shown in Figure 3.3 (a). After ligand exchanged distance between adjacent InSb QDs were reduced from 5.0 ± 0.5 nm to 2.6 ± 0.3 nm. Sample preparation for GI-XRD including calculation and measurement details is explained in the end of this chapter. Figure 3.3 (b) shows a typical HR-TEM image of the sample before ligand exchange, indicating ∼4.9 ± 0.5 nm (see Figure 3.3 (d), approximate interdot distance calculation before ligand exchange) interparticle distance between adjacent QDs. Whereas the distance decreased to ∼2.6 ± 0.3 nm (see Figure 3.3 (e), approximate interdot distance calculation after ligand exchange) after the ligand exchange as shown in Figure 3.3 (c).

3.2 Na_2S ligand

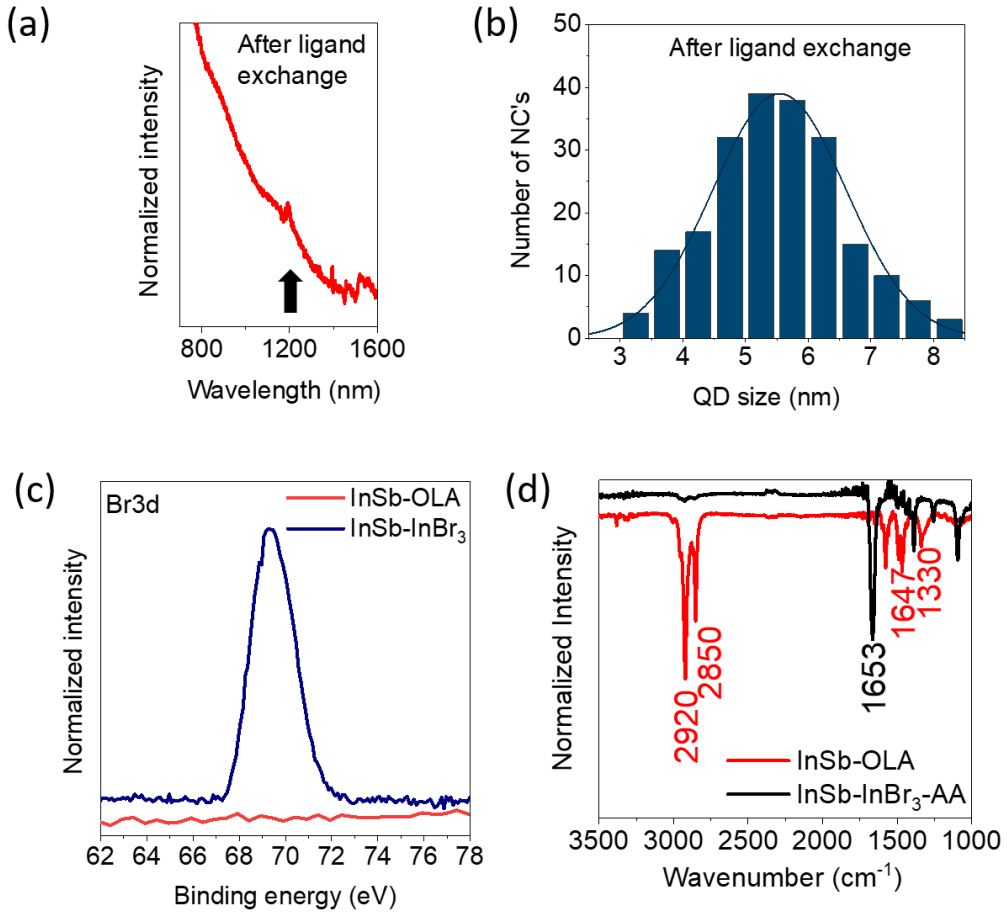

FIGURE 3.2: (a) UV-vis absorption spectra of synthesized InSb QD after ligand exchange. (b) Size Size distribution profiles of InSb CQD after ligand exchange. (c) XPS Br 3d spectra of InSb QDs before (red) and after ligand exchange (blue). (d) ATR-FTIR spectra of the InSb QDs before (red) and after ligand exchange (black).

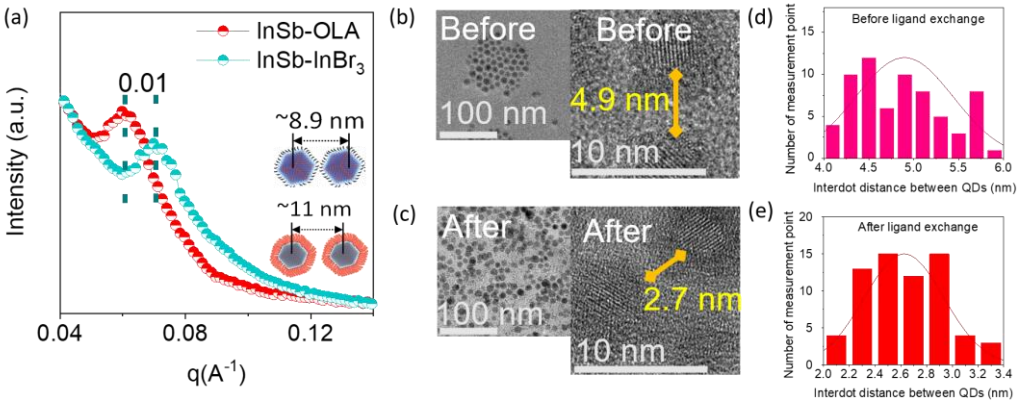

FIGURE 3.3: (a) q values of InSb QD films with OLA and $InBr_3$ ligands. HR-TEM images of the InSb QDs (b) before and (c) after ligand exchange. Inter-particle distance of QDs (d) before (e) after ligand exchange respectively.

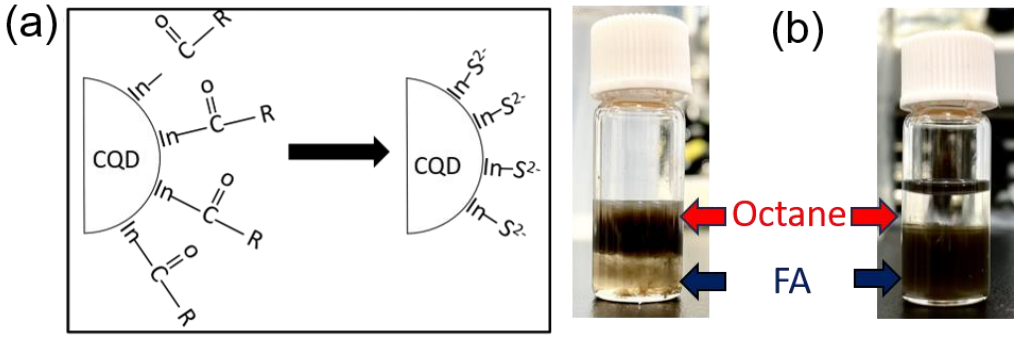

FIGURE 3.4: (a) q values of InSb QD films with OLA and $InBr_3$ ligands. HR-TEM images of the InSb QDs (b) before and (c) after ligand exchange. Inter-particle distance of QDs (d) before (e) after ligand exchange respectively.

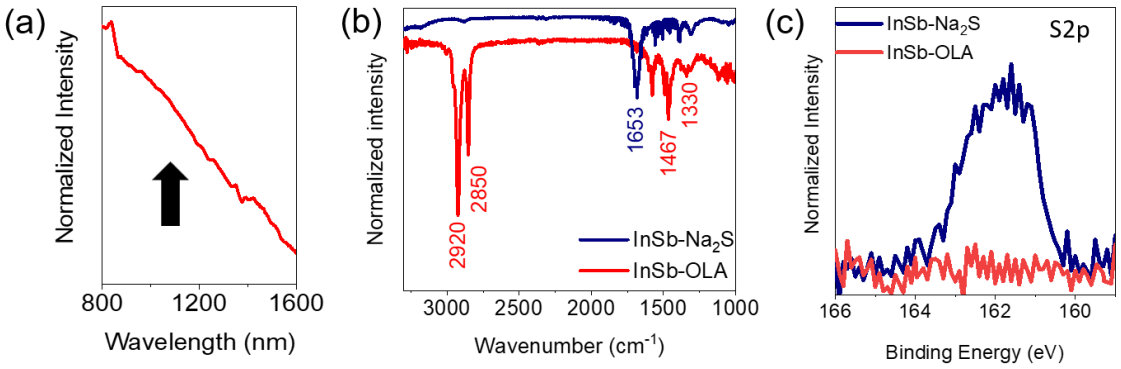

FIGURE 3.5: (a) q values of InSb QD films with OLA and $InBr_3$ ligands. HR-TEM images of the InSb QDs (b) before and (c) after ligand exchange. Inter-particle distance of QDs (d) before (e) after ligand exchange respectively.

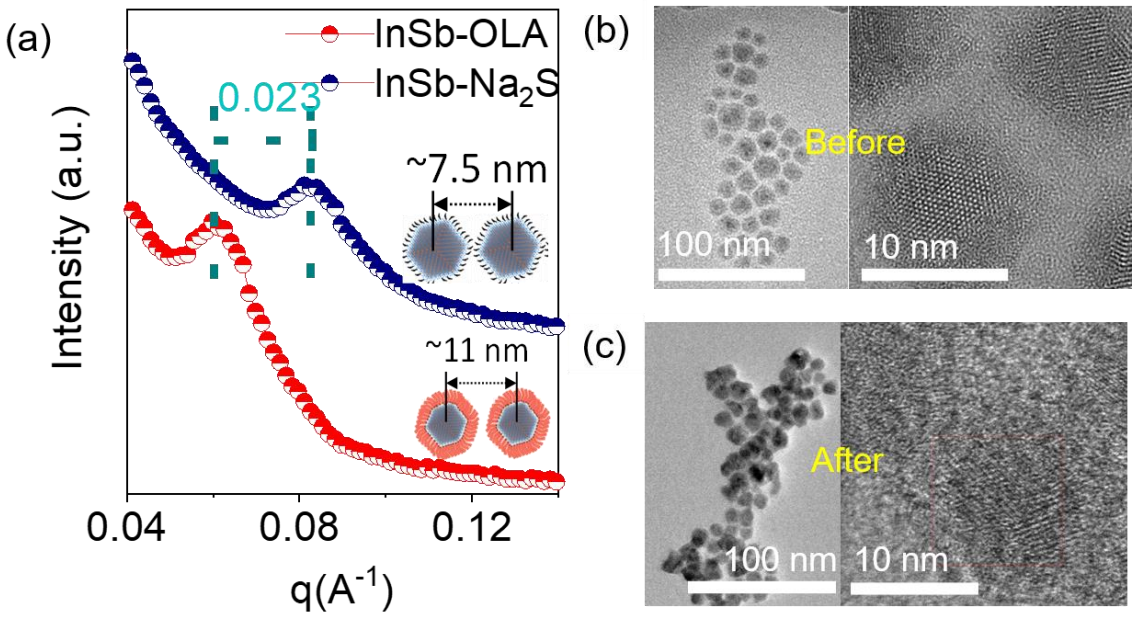

FIGURE 3.6: (a) q values of InSb QD films with OLA and $InBr_3$ ligands. HR-TEM images of the InSb QDs (b) before and (c) after ligand exchange. Inter-particle distance of QDs (d) before (e) after ligand exchange respectively.

In a typical synthesis, long-chain organic acids or bases attached to CQD surface as ligands aid the homogeneous growth of nanocrystals and stabilize the CQDs in organic solvent.[33,37] However, such ligands probably hinder the long-range charged carrier transport in CQD assemblies, yielding the reduced device performance of QPD.[46] Towards device design and development of QPDs, the exchange of long ligands allows widespread choice of materials to improve performance where charge carrier transport/transfer plays a major role.[45] It is expected that the in-plane carrier mobility of light-absorbing layer can be improved by shortening interparticle distance in CQD assemblies, leading to the improved performance of device such as responsivity, EQE and photoresponse time. In this work, Na_2S was treated to exchange with OLA ligands immobilized on InSb CQDs. Inorganic chalcogenides small ligand sulfide has been chosen because of its longer stability, low ionization energy donor for III-V semiconductors.[106] Details of ligand engineering is explained in Experiment section.

During synthesis of the InSb CQDs, OLA ligands were attached with cation (In3+) as L-type ligand.[107] Ligand exchange can be described as nucleophilic substitution at the metal site, while in the polar solvent anions has less solubility than cations. A schematic image shows removal of OLA ligand to S_2^- from CQD surface in Figure 3.4 (a). To exchange the OLA ligands to sulfur ions, the standard two-phase transfer protocol was performed. Briefly, in the post-synthesis step, OLA-capped InSb CQD dissolved in n-octane were vigorously mixed with the formamide (FA) solution of Na_2S. As the reaction happens over few minutes, CQDs were completely transferred from n-octane phase (top layer) to FA phase (bottom layer) as shown in Figure 3.4 (b), where chalcogenide ligands are favoured for electro statical stabilization.[108]

Next, changes in surface chemical property of CQDs before and after the Na2S treatment were characterized with combination of attenuated total reflection Fourier transform infrared (ATR-FTIR) spectroscopy and XPS. Figure 3.5 (b) shows ATR-FTIR spectrum of the OLA-capped InSb CQDs which demonstrates strong absorption bands in aliphatic C–H stretching region between 2850 and 2960 cm^{-1} and C–H bending/scissoring region between 1350 and 1500 cm^{-1}.[109] The C-H signatures disappeared after treating with Na_2S whereas a single peak was observed at 1653 cm^{-1} which is attributed to DMF-complex.[110] XPS spectrum of S 2p core level after Na_2S treatment demonstrates the appearance of the peak centered at 161 eV, indicating the formation of sulfur-capped CQDs by ligand exchange (Figure 3.5 (c))[111].

To elucidate an effect of sulfur-termination on the interparticle distance of CQDs in the photoactive layer, I measured the grazing-incidence small-angle X-ray diffraction (GI-XRD) patterns of OLA-, sulfur- and bromine-capped InSb CQDs (see Figure 3.6 (a)), respectively. Halides, a famous atomic ligand family, have been widely used to terminate the surface of CQDs for enhancing charge carrier transport in CQD solids,[9,52,104] and bromine was

served as a standard in this work. For accuracy of comparison, I used a same sample that consists of OLA-capped CQDs having a mean diameter of 5.5 ± 0.5 nm. The diffraction peak of OLA-capped QDs occurred at 2θ = 0.85°, whereas diffraction peaks were shifted to 2θ = 0.98° and 1.2° for bromine-capped and sulfur-capped counterparts, respectively (See Figure 3.7). The estimated value of centre-to-centre distance of CQDs was reduced from 5.0 ± 0.5 nm (for OLA-capping) to 1.5 ± 0.5 nm (for sulfur capping). It is worth noting that the interparticle distance of the sulfur-capped QD solid was significantly shorter than that of the bromine-capped counterpart (2.6 ± 0.3 nm). Furthermore, for the sulfur-capped CQD solid, the peak broadened as the peak-to-valley ratio decreased, suggesting an increase in packing density of the CQDs.[71] Transmission electron microscopy (TEM) revealed the reduction of interdot distance which indicate the successful exchange of ligands of InSb CQDs, while the sizes of nanocrystal's are unchanged after ligand exchange. The decrease in interparticle distance could be also confirmed by HR-TEM observation as shown in Figure 3.6 (b)-(c). In the sample before treatment with Na_2S, the CQDs were dispersed and isolated from each other, keeping the interparticle distance constant, as expected. In contrast, the CQDs were aggregated in the sample after exchanging the OLA with sulfur ligand. This was an unexpected and interesting observation result. Because even termination of CQDs with bromine (a typical atomic ligand) does not allow the agglomeration and the interparticle is kept constant.[52] To quantitatively understand the difference in CQD interaction between bromine and sulfur ligands quantitatively, I measured the zeta potential of both samples of QDs highly dispersed in DMF. As shown in Figure 3.7 (b) the sulfur-capped InSb CQDs in DMF solution showed a -4 mV of zeta-potential, nearly equal to electrically neutral. On the other hand, the value of zeta potential of the bromine-capped InSb CQDs in DMF solution was +20 mV as shown in Figure 3.7 (c). Such a large difference in zeta potential suggests

that the steric repulsion on CQD surface for sulfur-capped InSb CQDs is much weaker than bromine-capped counterpart, resulting in the difference in dispersion behaviours of CQD solids observed by HR-TEM and GI-XRD.

Figure 3.5 (a) shows an NIR absorption spectrum of a sulfur-capped CQD solid in film form. A broad clear excitonic characteristics around 1100 nm was observed. I confirmed that the relationship between bandgap and size was retained. Possible reason of the broad peak character might be due to the agglomeration of the CQDs.

3.2.1 Calculation of inter-particle distance from GI-XRD

Sample preparation for GI-XRD sample: InSb QD in DMF with concentration of 80 mg/ml was spin coated on top of Si substrate with 500 rpm for 30 sec, followed by heat treatment at 120 °C for 15 min.

Figure 3.7 shows the GI-XRD data of the InSb CQDs with OLA, $InBr_3$, Na_2S ligands. 2θ value was converted with Braggs formula:[112]

$$q = \frac{4\pi}{\lambda} sin\theta \tag{3.1}$$

Here, λ = 1.54 Å, 2λ is the scattering angle.

Here, d is Particle-to-particle distance calculated from following formula:[112]

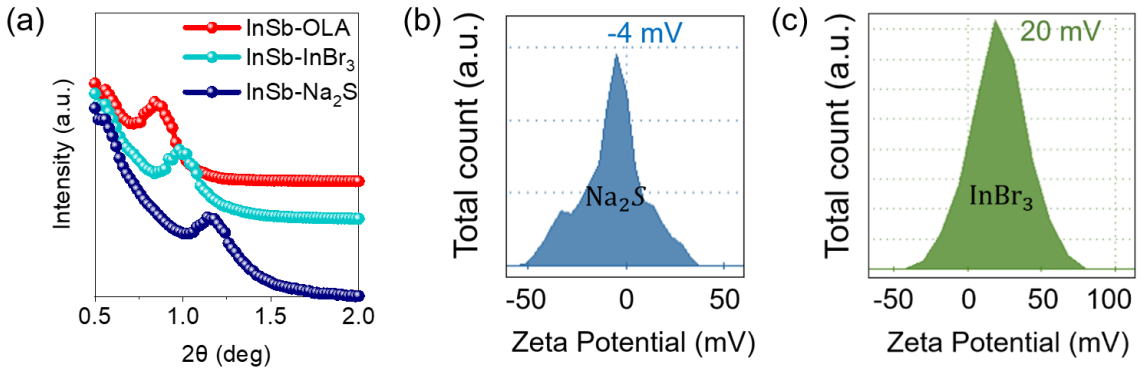

FIGURE 3.7: (a) GI-XRD data of InSb with OLA, $InBr_3$, Na_2S, capped QDs in 2θ. Zeta potential of InSb CQDs (approx. 2~ 3 mg/ml in DMF) using capping agent sulfide (b) and $InBr_3$ (c).

$$d = \frac{2\pi}{q} \tag{3.2}$$

Adjacent distance between particle (edge-to-edge of particle) was calculated by following formula:[112]

$$D = 2R - d \tag{3.3}$$

Here, R is average diameter of QDs.

3.3 Conclusion

In this chapter, OLA capped InSb was treated to exchange the long chain native ligand to short chain bromide and sulfide ligand counterpart. The ligand exchange was performed to improve the optoelectronic performance of the InSb QPD for fast charge transfer. FTIR study shows the complete removal of OLA as ligand. Whereas, XPS measurement shows the existence of bromide and sulfur peak after $InBr_3$ and Na_2S treatment, which further claims the attachment of these ligands. Additionally, we perform the GI-XRD to determine the exact value of interparticle distance after ligand exchange. HR-TEM was compared to support the inter particle reduction visually. Furthermore, to find the reason behind the close compactness of the QDs, I studied zeta potential to determine the surface charge on the QD surface which affects the steric repulsion on QD surface.

3.4 Experimental Section

Ligand exchange of $InBr_3$ ligand

Ligand exchange was performed as reported for InAs QDs.[72] In a typical experiment, 30 mg/mL of OLA-capped InSb QDs dispersed in octane were mixed with a mixture of 0.18 g of $InBr_3$ with 0.023 g of AA dissolved in anhydrous DMF. The mixture was then vortexed for 1-2 min, and the QD phase changed from octane to DMF. The transparent octane phase was discarded, and 1 mL of octane was added and vortexed for another 1-2 min. This step was repeated twice to wash the QDs. Then, 2 mL of toluene as anti-solvent was added and centrifuged at 6000 rpm for 10 min to precipitate the sample. The sample was placed under vacuum and dried for 2 h, followed by re-dispersion in anhydrous DMF at 50 mg/ mL concentration for device fabrication.

Ligand exchange of Na_2S ligand

Solution process ligand exchange was followed with modification of the report by Kagan et. al.[59] InSb CQDs dissolve in octane at 30 mg/mL were mixed with 20 mg/ml of Na_2S in FA (solution mixing ratio is 1 ml:1 ml). Then the solution was vortex for 10 min and CQD phase was changed from octane to FA. Then centrifuge at 4000 rpm for 5 mins to precipitate. After discarding the transparent solution 1 ml super hydrated Hexane was added and vortex for 5 mins and then centrifuged again at 4000 rpm for 5 mins to precipitate, this step has been done one more time. Then precipitated sample was dissolved in 1 ml of super hydrated Hexane and 1 ml of super hydrated Methanol was added and centrifuged at 6000 rpm for 10 mins to get the exchanged ligand sample. After 2 hr. of drying in a vacuum, the sample was dissolved in BTA + anhydrous DMF in a ratio of 2:1 for fabrication at a concentration of 100 mg/mL.

Chapter 4

InSb QD based Photodiode for SWIR sensing

4.1 QPD with Conventional Structure

4.1.1 $InBr_3$ ligand based InSb QPD

In general, PD devices have several advantages such as (i) operation at a bias voltage of 0 V, (ii) operation under both forward and reverse bias voltage, and (iii) long device lifetime.[46] To the best of our knowledge, this is the first paper to report InSb-QPD for the detection of SWIR light. Since the use of a smaller size of QD is suitable for enhanced hole mobility,[113] sample with size ~5 nm was chosen to form a light absorption layer of InSb-QD to achieve fast photoresponse. Figure 4.1 (a) shows the measurement system where a 400 W halogen light source from the NIR to SWIR range is used to illuminate the device from the ITO side. Photocurrent and photoresponses of the InSb QPD were measured by a Keithley 2425 source meter at room temperature in ambient air. In this work, I used a conventional device structure with the following multi-layer structure: ITO/PEDOT:PSS/InSb-QD/ ZnO/Al. In this device architecture, the PEDOT:PSS and ZnO layers served as the HTL and ETL, respectively. A cross-sectional view of the multi-layer structure shows that the thickness of the active layer was approximately 130 nm, whereas the thicknesses of the PEDOT:PSS and ZnO layers were 20 and 10 nm, respectively (see Figure

4.1 (b)). The proposed energy level diagram under a zero applied bias voltage is shown in Figure 4.1 (c). The values of the HOMO and LUMO of the PEDOT:PSS layer are taken from our previous work.[114] The energy structures of the InSb QD and ZnO thin films were characterized by a UPS study. The work function is defined as the difference in energy between the vacuum level and the Fermi level (e_{Fermi}). The UPS spectra of the secondary electron cutoff and valence band edge regions of their thin films are shown in Figure 4.1 (d) and Figure 4.2 (a)-(b), respectively. The work function is generally calculated by the dif- ference in energy between the secondary electron cutoff and the excitation photon energy ($h\nu$ = 21.22 eV). For the InSb QD thin film, the low and high binding energy cutoff regions of the UPS spectra are 0.74 eV (c_{onset}) and 16.42 eV ($cutoff_{high}$), respectively. The HOMO (ev) value was calcu- lated to be 5.54 eV from the following equations:[68]

$$e_v = h\nu - (Cutoff_{high} - C_{onset}) \tag{4.1}$$

Using the magnitude of the bandgap of InSb QD (E_g = 0.98 eV), the LUMO (e_c) was calculated to be 4.56 eV from:

$$e_c = e_v - E_g \tag{4.2}$$

From the equation, e_c has been calculated as 4.56 eV, whereas the Fermi energy level (e_{Fermi}) of the InSb QD was calculated to be 4.8 eV from[90]

$$e_{Fermi} = h\nu - cutoff_{high} \tag{4.3}$$

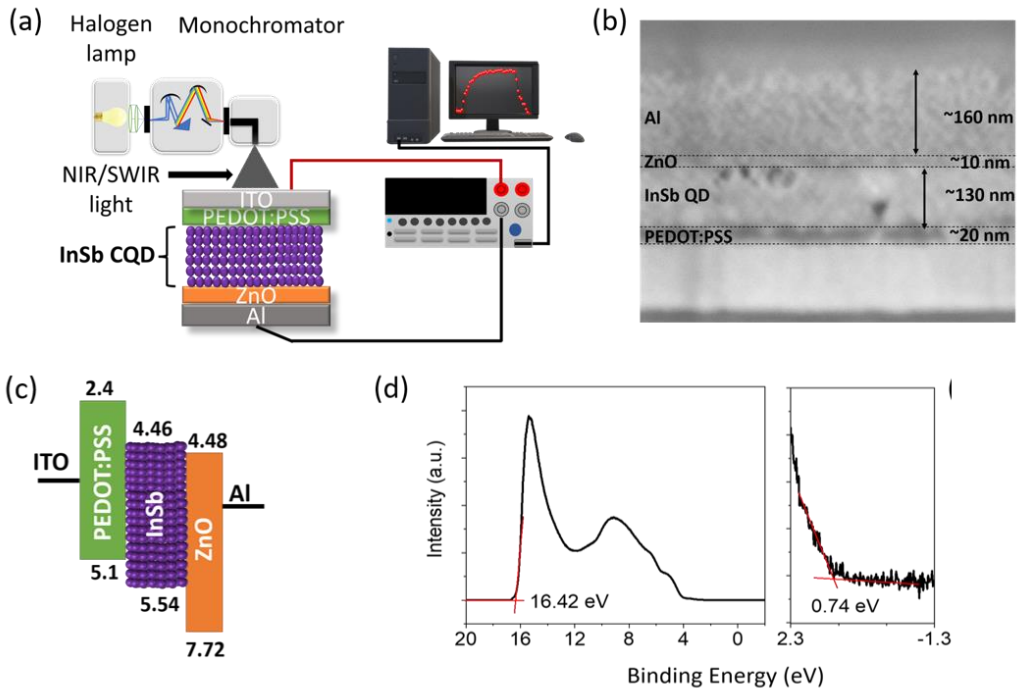

FIGURE 4.1: (a) Optical setup for device performance characterization of InSb-QPD. (b) A typical cross-sectional SEM image of the InSb-QPD structure with the organic-inorganic hybrid multi-layer stack. (c) Energy band diagram in the unbiased conditions. (d) UPS spectrum of InSb QD where the high-binding-energy cut-toff region is determined; the right panel displays the low-binding-energy cutoff region, respectively.

For the ZnO thin film, the calculated values of e_v and e_c were 7.72 and 4.72 eV as shown in Figure 4.2 (c) (UPS spectra and bandgap calculation of ZnO by tauc plot.

Figure 4.3 (a) (I-V characteristics in logarithmic scale) and Figure 4.3 (b) (I-V characteristics in linear scale) depict the current versus voltage (I-V) characteristics of the InSb QPD in the dark and SWIR light illumination with different light intensities (λe_m = 1200 nm, 1.0, 2.0, and 4.0 mW/cm^2). The active area of the device was approximately 0.04 cm^2. According to the I-V curve, the dark minimum appears at the negative region of the voltage because of the capacitive hysteresis effect in the device, which happens possibly due to the interface of electrodes

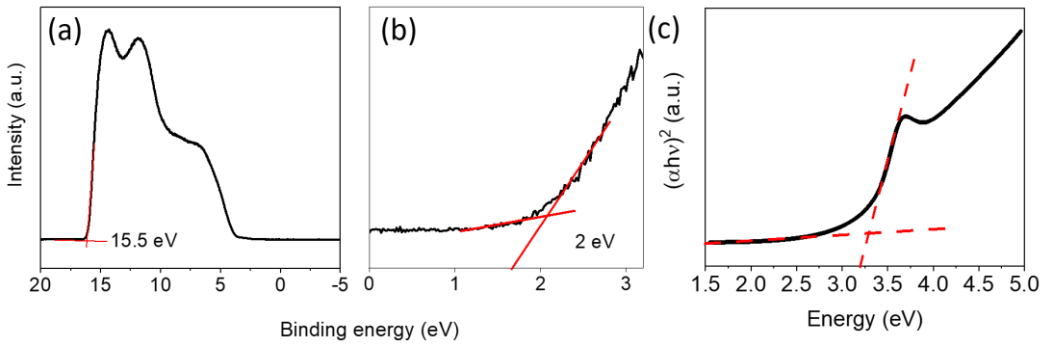

FIGURE 4.2: (a) UPS spectrum of ZnO where the high-binding-energy cutoff is determined, (b) the right panel displays low-binding-energy cutoff region, respectively. (c) Tauc plot of ZnO calculated from absorption spectra of ZnO.

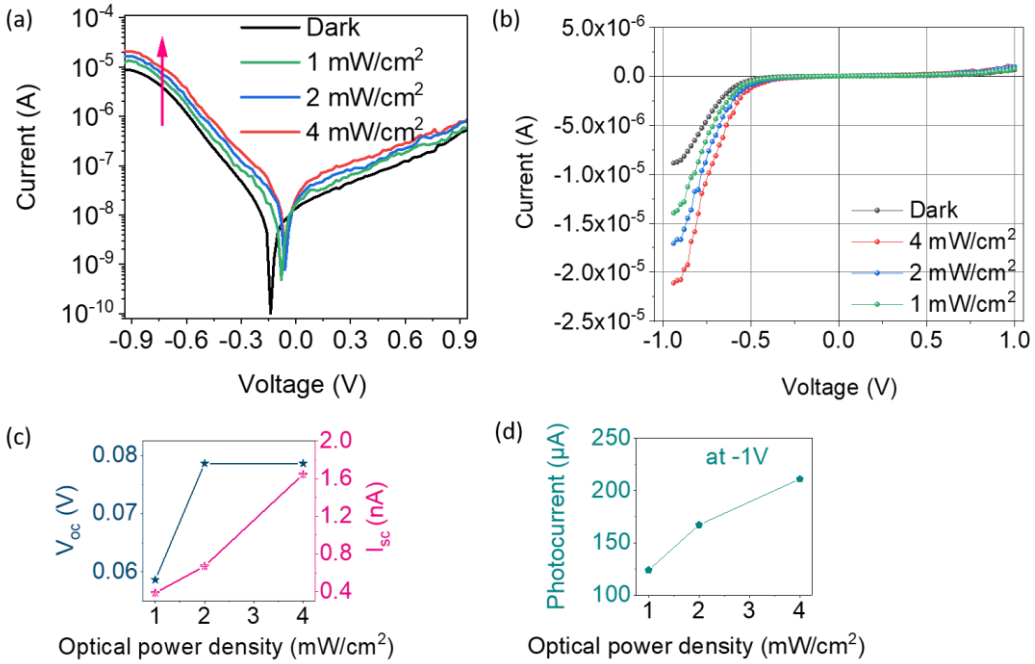

FIGURE 4.3: I-V characteristics in (a) log- and (b) linear-scale of InSb-QPD under the illumination of SWIR light (λ = 1200), optical intensity-dependent values of (c) V_{oc} and I_{sc}, and (d) photocurrent at -1 V.

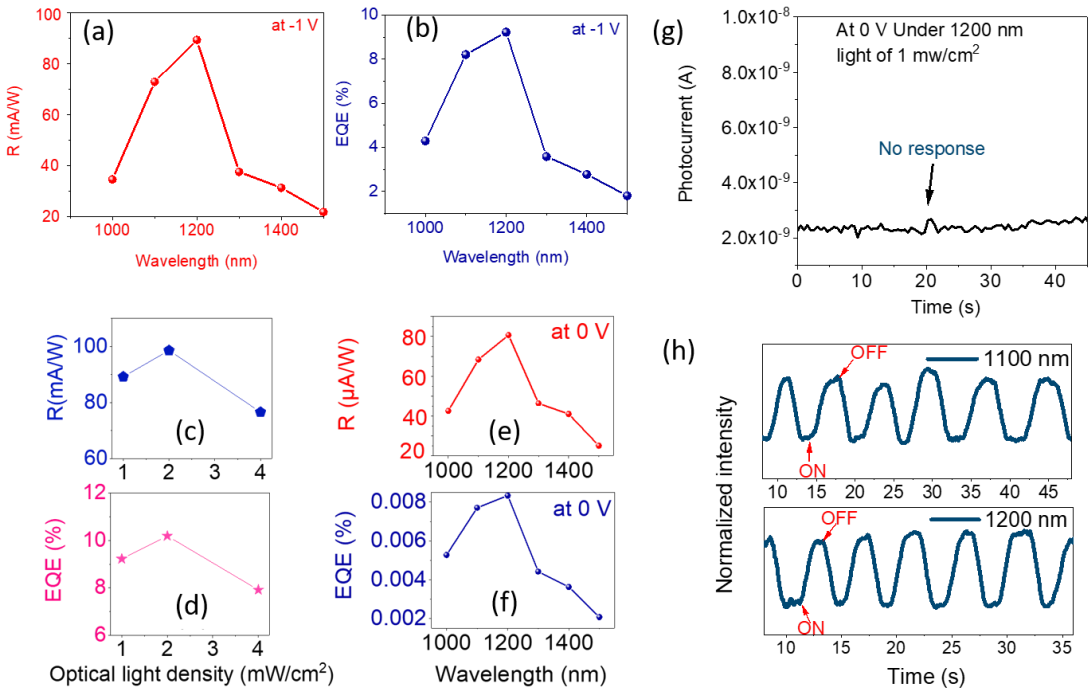

FIGURE 4.4: (a),(e) R (b), (f) EQE corresponds to the figure of merits under different wavelengths of light under (illumination of 1 mW/cm^2) at -1 and 0 V of the photodiode, respectively. Whereas (c) and (d) are, R and EQE of the photodiode under different intensities of 1200 nm light at -1 V, respectively. (g) Photoresponse of OLA-QD device under at a constant optical power density of 1 mW/cm^2 of SWIR light (1200 nm) at a bias voltage of 0 V. (h) Time response curve of photocurrent at 0 V bias voltage under the SWIR light illumination (λ = 1100 and 1200 nm, 1 mW/cm^2.

and adjacent layers. These nonzero-crossing phenomena were often observed in many photodetectors before.[72,115–119] Nevertheless, a typical rectifying characteristic was observed, suggesting the formation of a heterojunction between ETL, QD layer, and HTL. Upon irradiation of SWIR light, an open circuit voltage (V_{oc}) and a short circuit current (I_{sc}) were generated, where I_{sc} was increased linearly by increasing the illumination power densities, which signified the PD characteristics. The trend of the values of V_{oc} and I_{sc} with changing optical power density is shown in Figure 4.3 (c). Figure 4.3 (d) depicts the linear trend of the photocurrent at -1 V by increasing the light intensity of SWIR light. The current increased due to the photogenerated carriers in parallel with the reverse bias. Under the reverse bias at -1 V, the dark current was 8.84 μA, whereas the light current of the device was 21.1 μA upon increasing the illumination intensity of SWIR light up to 4 mW/cm^2, indicating the detection of the SWIR light. The current device achieved an I_{light}/I_{dark} ratio of 2.38 at -1 V. At -1 V, the dark current was very high, contributing to the photodiode's shot noise. Here, I assume shot noise is the main source of noise for the photodiode, as InSb is a low bandgap material. R, defined by the generated photocurrent per incident unit optical power, was calculated according to the following equation:[74]

$$R = \frac{(I_{Light} - I_{Dark})}{PA} \tag{4.4}$$

where I_{light}, I_{dark}, P, and A are the photocurrent, dark current, incident light power, and effective device area (0.04 cm^2), respectively.

Figure 4.4 (a) shows the responsivities as a function of wavelength of incident light with a constant optical light power density (1 mW/cm^2) at a bias voltage of -1 V when the wavelength was varied between 1000 and

1500 nm. I see an increasing trend of responsivity in the shorter wavelength range, the peak value (~89 mA/W) at 1200 nm, and a decrease after that, which is a similar feature to the optical absorption characteristic of the sample. In the whole wavelength range, the calculated responsivities were higher than previous values reported elsewhere (see Table 4.1). External quantum efficiency (EQE), the practical figure of merit is defined as the number of free electrons recovered by the device's external circuitry per photon incident on the device and expressed by the following equation:[120]

$$EQE = \frac{hcR}{e\lambda} \tag{4.5}$$

where h is Planck's constant, and c is the velocity of light.

Figure 4.4 (b) shows the external quantum efficiency (EQE) of the InSb-QPD operated at -1 V while varying the wavelength of the incident light between 1000 and 1500 nm. EQE increases between 1000 and 1200 nm and peaks at 1200 nm, while it decreases between 1300 and 1500 nm, consistent with the excitonic feature of the absorption spectrum is show in Figure 3.2 (a). The best value of the EQE at -1 V was 9.2% when irradiated with 1200 nm light at an optical power density of 1 mW/cm^2. Further, both figures of merits were calculated under a 1200 nm wavelength light with different light power intensities as shown in Figure 4.4 (c) and (d) (R and EQE of the photodiode at -1 V with different optical light density), where R and EQE values were increased to ~98 mA/W and 10.1%, respectively, but later with higher intensities of light, both values took decreasing trends which have been observed widely in QD-based photodetectors.[46,121,122] At 0 V, the photodiode achieved R and EQE of 80.6 μA/W and 0.008%, respectively

(Figure 4.4 (e)-(f) R and EQE of the photodiode at 0 V with different wavelengths with constant optical power density 1 mW/cm^2). Nevertheless, this phenomenon justifies the working phenomenon of typical self-driven characteristics of photodetector.

To date, InSb QDs have been developed to serve as light-absorbing layers in phototransistors and photoconductors, as listed in Table 4.1, but they have faced the barrier of low responsivity. There are three possible reasons why I observed high values of responsivity to the SWIR light of 1000-1500 nm wavelength in this work. First, the stoichiometric InSb QDs synthesized from a new combination of precursors, $InBr_3$ and $SbBr_3$ were composed of only a crystalline structure without an amorphous phase and other secondary phases including hydroxides or oxides. The purification steps worked for completely removing byproducts and unreacted molecules including ligand molecules, yielding a solid product in powder form, unlike an oily product. The high molecular packing density of OLA, as evidenced by the high solubility of the QDs in octane even at the concentration as high as 100 mg/mL, probably inhibits surface oxidation. Second, due to the high molecular density of $InBr_3$ bonded to the QD, the resultant colloidal ink would work to form a flat and smooth thin film serving as an optical absorbance layer. Furthermore, the molecular replacement with $InBr_3$ ligands alters the interparticle dielectric environment as well as tunneling distance, possibly leading to the enhanced carrier mobility. As predicted, the device where the OLA-capped QDs were used as a light absorption layer showed no response to the SWIR light irradiation (see Figure 4.4 (g), photoresponse of the OLA-QD device), indicating suppressed carrier mobility by the insulating OLA shells. Third, as shown in Figure 4.1 (c), the deep HOMO level of the ZnO layer could block leaking holes, whereas the PEDOTT:PSS would block leaking

the electrons, yielding efficient dissociation of photogenerated carriers to improve the responsivity.

The typical photoresponses of the device are shown in Figure 4.4 (h) demonstrate the reproducible photocurrent response and cycling stability even at a voltage bias of 0 V under illumination of 1100 and 1200 nm light with an optical power density as low as 1 mW/cm^2. The response profile shows that the measured rise time (τ_{rise}: from 10 % to 90 % of the saturated value) and fall time (τ_{fall}: from 90 % to 10 % of the peak value) were ~550 and ~800 ms. It is noted that the InSb-QPD exhibited the pronounced photovoltaic behavior under light illumination at the external bias voltage of 0 V, indicating that the device functions as a self-driven photodetector.

4.1.2 Na_2S ligand based InSb QPD

DMF ink of the sulfur-capped InSb CQDs was used to fabricate SWIR photodiodes. The sample C (Figure 2.10 (a)) was chosen as a photoactive material. The resultant InSb-QPD was compared with the bromine-capped counterpart to explore the effect of shortened interparticle distance on device performance. An ultraviolet photoelectron spectroscopic (UPS) spectrum of the spin-coated sulfur-capped InSb CQD film shown in Figure 4.5 (a) demonstrates the low and high binding-energy cutoff region which were 0.82 eV and 16.6 eV respectively. As the work function is calculated by the difference in energy between the secondary electron cutoff and the excitation photon energy (hυ= 21.22 eV), the highest occupied molecular orbital (HOMO) value was estimated to be 5.44 eV. Using the magnitude of bandgap of the sample C (E_g = 1.22 eV) the lowest unoccupied molecular orbital (LUMO) value was estimated to be 4.22 eV. The Fermi energy level was estimated to be 4.62 eV. The proposed energy level diagram under a zero applied bias was depicted in Figure 4.5 (b). The HOMO and LUMO values of

PEDOT:PSS and ZnO films were referred to the values reported in the previous paper.[52] A typical cross-sectional scanning electron microscopic (SEM) image shown in Figure 4.5 (c) demonstrates 20-nm thick ZnO and 10-nm thick PEDOT:PSS layers. The sulfur-capped InSb CQD layer has a thickness of 130 nm and its surface was rough at nanoscale because they were beginning to aggregate in DMF. The photoactive area of the QPD was approximately 0.04 cm^2.

Device performances of the QPDs, where sulfur-capped InSb QDs served as a photoactive layer, measured at room temperature in ambient air are summarized in Figure 4.6 (a)-(e) and Figure 4.7. The representative photocurrent-voltage characteristics (I-V) shown in Figure 4.6 (a) were obtained using the sample C (Figure 2.10 (a)) and measured under dark conditions (no illumination) and light illumination of different wavelength ranging between 1000 nm and 1500 nm while the photon power density of the incident light was fixed at 1 mW/cm^2. Photocurrent generated greater than dark current indicated that the device responded to light and are also dependent of wavelength of incident light. The highest photocurrent was achieved under 1100 nm wavelength light. Device responsivity and EQE are figure of merit of photodiode devices. The photoresponsivity (R) is defined as equation below:[123]

$$R = (I_{light}-I_{dark})/P_{in}A$$

where I_{light}, I_{dark}, P_{in}, and A are photocurrent, dark current, incident light density, and active device area, respectively. EQE is defined as the number of free electrons recovered by the device's external circuitry per photon incident on the device, and expressed by equation below:[120]

$$EQE = hcR/e\lambda$$

where h is Planck's constant, c is velocity of light.

Figure 4.6 (b)-(d) show the values of EQE and R at 0 V, which proves the self-powered operation of the QPD. The highest values of EQE and R for the QPD operated at 0 V with 1100-nm light at a power density of 1 mW/cm^2 power density were 1.32 % and 0.012 A/W, respectively. As expected, EQE and R of the photodiode were enhanced when bias voltage is applied to the device as shown in Figure 4.6 (c)-(e). Similar enhancement was observed at other incident light wavelengths. The best values of EQE and R under 1100 nm at -1 V were 18.52 % and 0.18 A/W. Comparing with recent progress of SWIR Pb- and Hg-free QPDs, our InSb QPD achieved better EQE at 0 and -1 V as evidenced in Table 4.1.

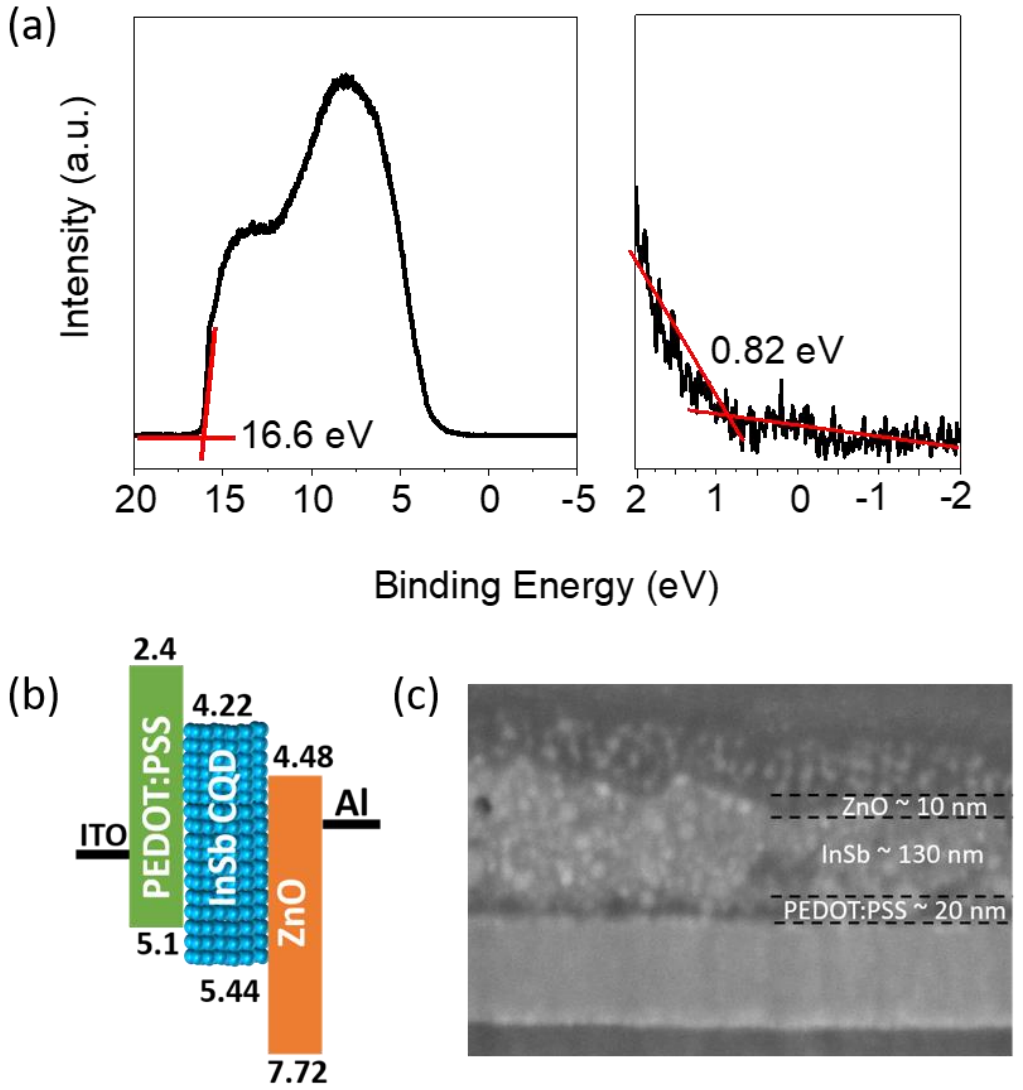

FIGURE 4.5: (a) UPS spectra of S^{2-} capped InSb CQD with high-and low-binding energy cutoff region was determined. Energy band diagram of the QPD at no bias condition. A typical cross-sectional SEM image of the QPD stack.

Figure 4.7 (a) shows I-V characteristics of the InSb-QPD on a logarithmic scale when the incident light optical power density at 1100 nm was varied between 1.0 and 4.0 mW/cm^2. Surprisingly, a dark current density was as low as 3.8 nA cm^{-2} and 70 µA cm^{-2} at 0 V and -1 V. Furthermore, dark current density appears 3.5- and 3.15-times less at -0.5 V and -1 V compare to previously reported bromine-capped InSb QPD device, which results higher EQE and R values for sulfur-capped InSb QPD. Recently, for QPD devices it was discussed that dark current density of QPD device is sensitive due to CQD doping and trap density, a lower trap density and doping level can cause lower dark current and higher EQE in a device.[71] Here, UPS study of sulfur-capped InSb CQDs shows 0.06 eV intrinsic behavior than bromine-capped InSb CQDs, which is one of the possible reasons for decrease in dark current (Figure 4.8). Therefore, InSb QPD attained less dark current due to less doping level which eventually aids to lower the trap density and improved the arrangement quality of the CQDs in film. The photocurrent density was dependent of optical power density of the incident light. With increasing optical power density, photocurrent density increases up to 850 µA/cm^2 at 4 mW/cm^2. Figure 4.7 (b) displays the short circuit current and photocurrent at -1 V, whereas V_{oc} of the QPD is shown in Figure 4.7 (c) with different intensity of light. It shows a linear increase which further implies the general work function of a photodiode, R^2 values has been mentioned in the figures. Figure 4.7 (d) shows the enhanced intensity of photoresponse with increasing optical power density of incident light. A typical result of the time response curves is shown in Figure 4.7 (e), where a quick and reproducible photocurrent responses and good cycling stabilities were observed at 0 V and 0.1 V of bias voltage. Furthermore, the response profile exhibits that the measured rise time (τ_r: from 10% to 90% the saturated value) and fall time (τ_f: from 90% to 10% of the saturated value) are ~200 msec and ~200 msec at 0 V of bias voltage. These values were 2.75 and 4.5 times smaller than

recently reported InSb CQD QPD.[52] Such improvement was also observed under white light irradiation even at very high optical power density (80 mW/cm^2), especially in the fall time of the QPD (Figure 4.9 (a) and (b)).

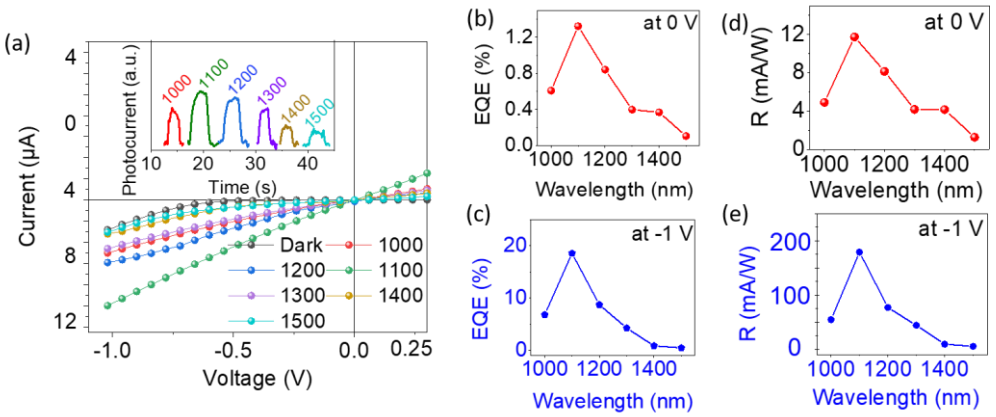

FIGURE 4.6: (a) I-V characteristic of the QPD in linear form under different SWIR wavelength of light, inset shows the photoresponse of the QPD under different wavelength of SWIR light. (b) and (c) shows the EQE of the QPD, whereas (d) and (e) show the Responsivity of the QPD under 0 and -1 V, respectively.

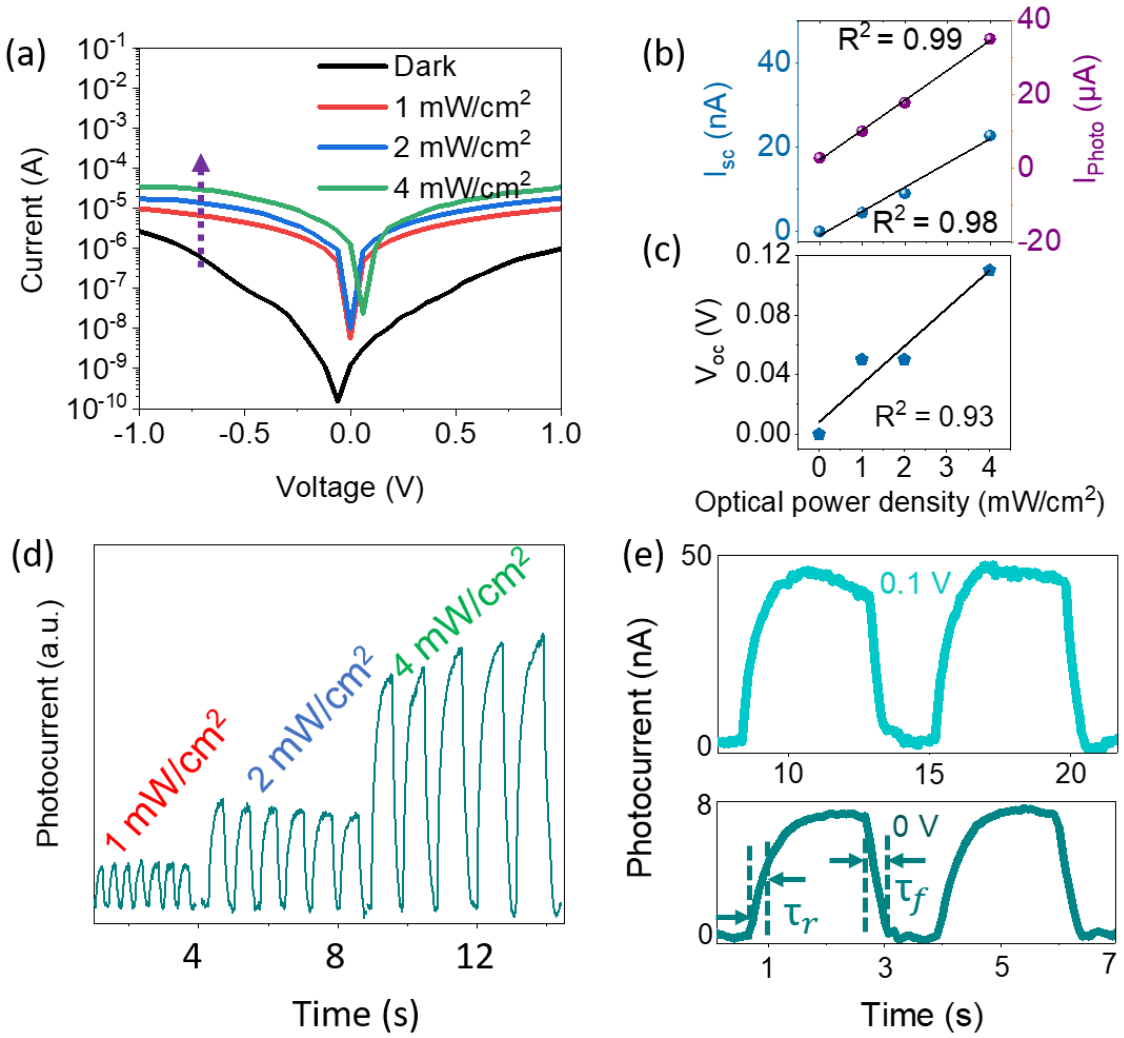

FIGURE 4.7: (a) Logarithmic I-V characteristic of QPD under 1100 nm with different optical light intensity. Optical illumination intensity dependent (b) I_{sc} and I_{photo} (-1 V) and (c) V_{oc} values. (d) Photoresponse of the QPD under different light intensities of 1100 nm light. (e) Photoresponse of the QPD under 0 and 0.1 V.

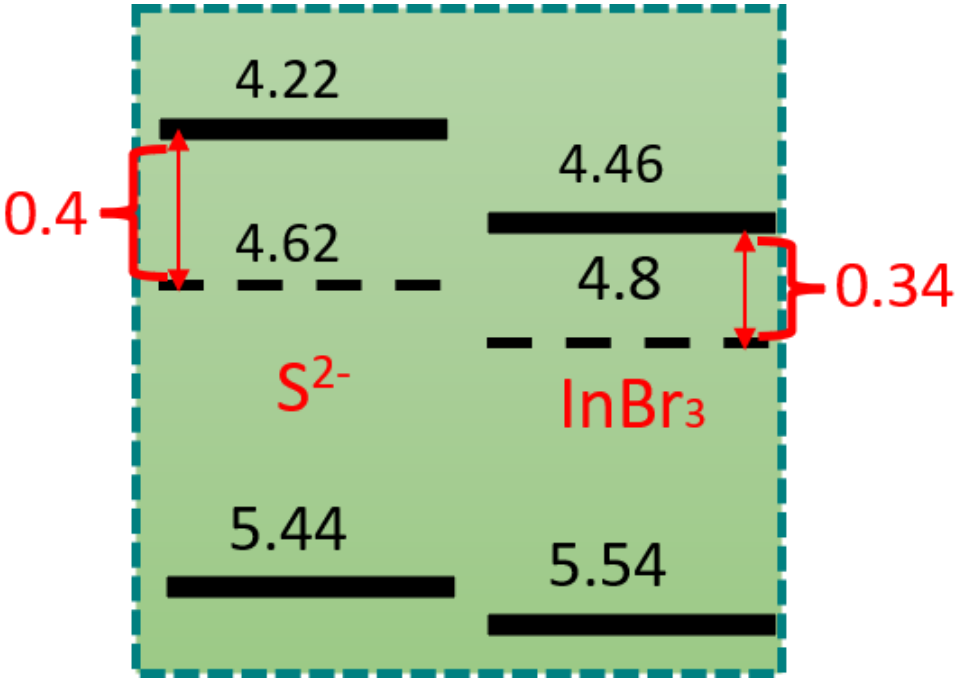

FIGURE 4.8: Energy band diagram of two different ligands measured by Ultra Photon Spectroscopy (UPS).

TABLE 4.1: Summary of the device performances for NIR-SWIR photodetectors based on InSb QDs. PT: Phototransistor, PC: Photoconductor, PD: Photodiode, R: Responsivity, EQE: Equivalent quantum efficiency, T: Response time and λ: Incident-light wavelength.

Optically Active Layer	Device Type	Ligand	R (A/W)	EQE (%)	λ (μm)	T (sec)	Ref
InSb	PT	K_2S, K_2Te	------	------	------	------	27
InSb	PC	Na_2S	------	------	------	------	59
InSb:PCBM:poly-TPD	PT	OLA	4×10^{-5}	------	1, 1.2, 1.4	0.08	74
In(P)As	PD	MPD	0.031(-3V) 0.029(-3V) 0.007(-3V)	5(-4V) 5(-4V) 1(-4V)	1.14 1.27 1.4	1.2×10^{-6}, 8.9×10^{-6} at -3 V under 100 mW/cm² white LED	70
InSb	PD	$InBr_3$	0.098(-1V) 8×10^{-4} (0V)	10.1(-1V) 0.008(0V)	1.2	0.55 at 0 V under 1,2 and 4 mW/cm² SWIR from Halogen lamp	52
InSb	PD	Na_2S	0.18(-1V) 12×10^{-3} (0V)	18.52(-1V) 1.3(0V)	1.1	0.2 at 0 V under 1,2 and 4 mW/cm² SWIR Halogen lamp 0.005 and 0.009 at 0V under 80 mW/cm² white light Xenon lamp	Currently in Submission

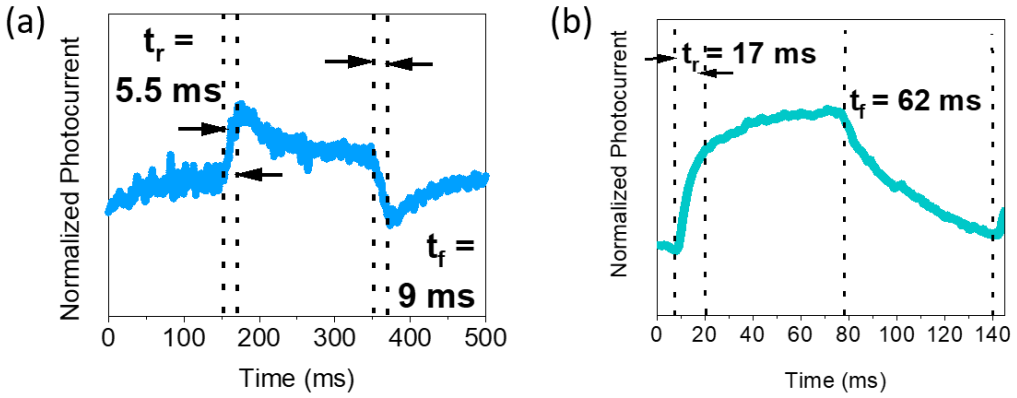

FIGURE 4.9: Normalized photocurrent response of the QPD with (a) Na_2S and (b) $InBr_3$ capped InSb CQD under white light illumination (80 mW/cm^2).

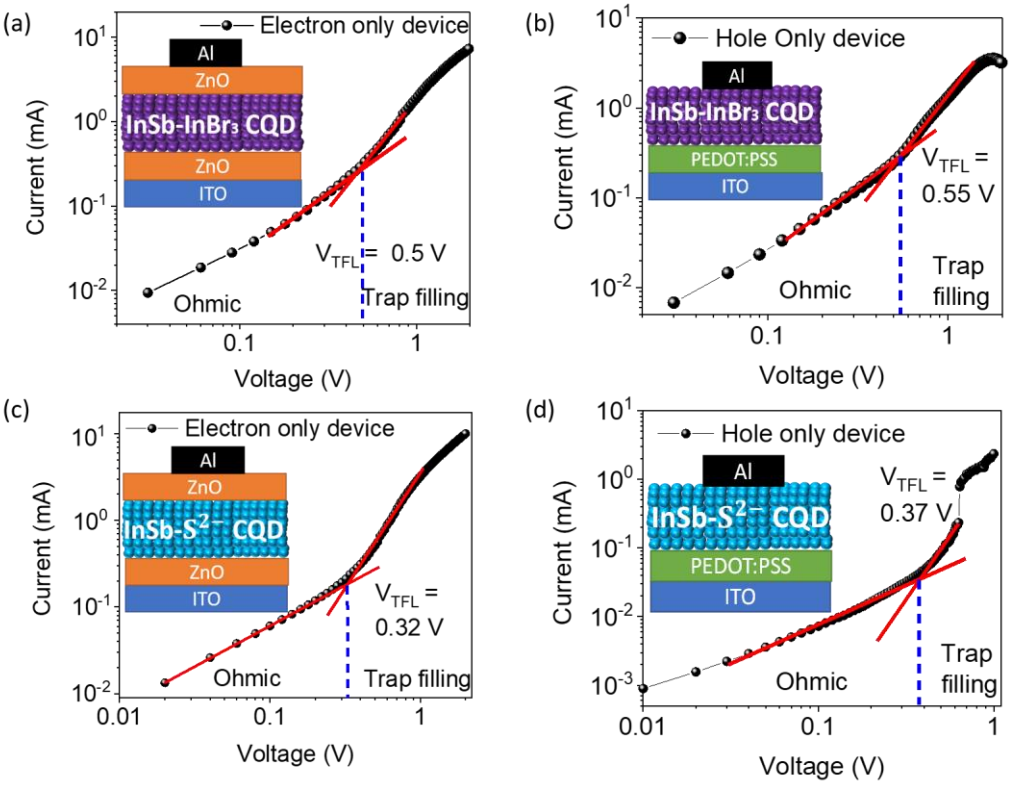

FIGURE 4.10: (a) and (c) The electron mobility from *ZnO*/***InSb-InBr***$_3$/*ZnO* and *ZnO*/***InSb-Na***$_2$***S***/*ZnO* devices respectively. (b) and (d) The hole mobility from *PEDOT: PSS*/***InSb-InBr***$_3$ and *PEDOT: PSS* /***InSb-Na***$_2$***S*** devices respectively.

There are two possible reasons why device performance was improved by replacing the OLA ligand with a sulfur ligand. First, the in-plane carrier mobility of QD solids is enhanced by using sulfur-capped CQDs. For evidence, I prepared hole-only device and electron-only device as shown in Figure 4.10 and estimated the carrier mobility and carrier trap density. The devices with bromine-capped InSb CQDs were used as a standard. The estimated carrier mobility and trap density from space charged limited current (SCLC) and trap-filled regime are summarized in Table 4.2. This quantitative analysis showed that capping with sulfur ligands improved carrier mobility by a factor of 1.6 for electrons and 1.8 for holes. Furthermore, the sulfur-ligand reduced the carrier trap density by a factor of 1.57 for electrons and 1.47 for holes. In addition to the reduction of carrier traps, the improved carrier mobility between the QDs, especially due to the sulfur ligands, contributed to the improved device performance. Second, the HOMO-LUMO level of sulfur-capped InSb CQDs was shifted to higher energy values, resulting in a favourable energy band for better charge transport. The HOMO value of the sulfur-capped InSb CQD layer has been shifted to 5.44. It eventually decreases the energy barrier between the valence band maximum (VBM) of the photoactive layer concerning VBM of HTL layer PEDOT:PSS, which may increase build-in-potential (V_{bi}), enable better hole transportation, and improve the V_{oc}.[124,125] Thus, by improving the electron blocking with better hole extraction,[126] it suppressed the dark current and resulted the faster photoresponse. Using the photoresponse speed 3-dB bandwidth of the photodiode was calculated from the relation: Bandwidth (BW) = $0.35/t_r$, where t_r is the rise time of the photodiode.[30] BW of the sulfur-capped QPD was 63 Hz, whereas BW of the bromine-capped QPD was 20 Hz.

Fabrication procedure: The ZnO layer was spin-coated with 2500 rpm for 45 sec. After that substrate was dried on top of a hot plate at 120 C for 15 min. PEDOT: PSS layer was spin-coated with 5000 rpm for 35 sec,

followed by heat treatment at 120 C for 15 min. QD layer was spin-coated at 1000 rpm for 60 sec, followed by heat treatment at 80 C for 20 min. This process was repeated 10 times to thicken the layer.

Figure 4.10 shows the I-V curve of electron-only and hole-only devices. Mott-Gurney formula was used to calculate carrier mobility:[127–129]

$$J = \frac{9}{8}\varepsilon_r \varepsilon_0 \mu \frac{V^2}{d^3} \tag{4.6}$$

Where J is the current density, ϵ_r and ϵ_0 are the relative dielectric constant of InSb in bulk and the permittivity of free space, respectively. μ is the field-independent carrier mobility, and d is the thickness of the QD layer. Here, ϵ_r and ϵ_0 are set to be 16.8 and $8.85 * 10^{-14}$ F cm^{-17}. The thickness of QD films is about 100 nm.

N_t is the carrier trap density of the thin film has been calculated by the following formula:[127,130]

$$V_{TFL} = \frac{eN_t d^2}{2\epsilon_r \epsilon_0} \tag{4.7}$$

Here, e represents elementary charge, V_{TFL} known as trap filled limit voltage. V_{TFL} can be described as the transit point between two regions:

TABLE 4.2: Summary of the Carrier mobility and Carrier trap density calculated from SCLC from electron-only and hole-only device.

Ligand	μ_e **(cm^{2}V^{-1}S^{-1})**	μ_h**(cm^{2}V^{-1}S^{-1})**	**e-only N$_t$**	**h-only N$_t$**
$InBr_3$	0.012	0.01	$9.3 * 10^{11}$	$1 * 10^{12}$
Na_2S	0.02	0.018	$5.9 * 10^{11}$	$6.8 * 10^{11}$

ohmic region ($I \propto V$), and trap-filled limit region (TFL region). From Equation 4.7 N_t (Carrier number/cm^3) values for h-only and e-only are $9.3 * 10^{11}$, $5.9 * 10^{11}$ and $1 * 10^{12}$, $6.8 * 10^{11}$, respectively.

4.2 Conclusion

The OLA molecules were exchanged by the $InBr_3$ ligands under two-phase conditions employing octane as the nonpolar phase and DMF as the polar phase, leading to significantly enhanced carrier transportation in the QD film. I further built a photodiode with a multilayer structure where InSb QDs were sandwiched between PEDOT:PSS as the HTL and ZnO as the ETL by taking advantage of the solution-processed method. The QPD achieved high responsivity and EQE compared to those of other reported InSb-based photodetectors. Our findings open a new window where InSb shows potentiality to substitute toxic materials for SWIR photodetectors. Colloidal synthesis of crystalline QDs without surface oxides will become the next subject to improve the optoelectronic performances.

Next, post-synthesis ligand engineering with S^{2-} ligand was performed to improve the mobility and trap density of the QD surface, which eventually improves the charge transfer between the adjacent CQDs by reducing the inter-particle distance of adjacent CQDs. Due to having less trap density S^{2-} capped InSb QPD film achieves a very low dark current which is very

competitive among SWIR materials. Further, sulfide capped InSb thin films show very high carrier mobility which could be applicable vastly for SWIR fast sensing in the future. Further, fabricated sulfide capped InSb QPD responded as a self-powered photodiode and achieved 1.3% EQE and responded 5.5 ms under 0 V. The fast response with promising figures of merit shows the potential to substitute Pb, Hg, and As-free quantum dots for SWIR sensing. Further improvements in terms of EQE and photoresponse speed are possible by reducing trap density, improving band alignment, and increasing carrier extraction within the QPD structure.

Chapter 5

Conclusion and Future work

5.1.1 Future work

InSb is an established semiconductor candidate from III-V family for various device applications for optoelectronics, although colloidal InSb QDs has not been studied because of their unsolved surface chemistry and many other physical properties. Additionally, improvement of carrier mobility by improving the surface defects and ligand exchange and doping should be evaluated in future for various SWIR to MWIR application. Based on the current comprehensive knowledge of this material system proposed future works are: al-inorganic InSb CQD photodetector.

5.1.2 All-inorganic Inverted Structure QPD

In this work, I used an inverted device structure with the following constituent layers: ITO/Al-doped ZnO/InSb QD/MoO_3/Al. In this device architecture, the Al-ZnO and MoO_3 layers served as the electron transportation layer (ETL) and hole transportation layer (HTL), respectively. Proposed energy level diagram under a zero applied bias voltage is shown in Fig. 5.1 (a). A cross-sectional SEM image of the multi-layer shows that the thickness of the active InSb QD layer was ~ 90 nm, whereas the thicknesses of the ZnO and MoO_3 layer were 12 nm and 9 nm, respectively (see Fig. 5.1 (b)). Fig. 5.1 (c) shows the EDS mapping of the cross-sectional layers of the device. HOMO and LUMO values of MoO_3 is taken from our previous work. Fig. 5.2 (a) depicts the current versus voltage (I-V) characteristics of the InSb QPD in the dark and SWIR-light illumination (λ_{em} = 1200-1800 nm,

18 mW/cm^2) using the halogen lamp. The active area of the device was approximately 0.04 cm^2. According to the I-V curve in the dark, a typical rectifying characteristic was observed, suggesting the formation of hetero-junction between ETL, QD layer, and HTL. Upon irradiation of SWIR light, an open circuit voltage (V_{oc}) and a short circuit current (I_{sc}) are generated, signifying the PD characteristics. The current density increased due to the photogenerated carriers in parallel with the reverse bias. Under the reverse bias at -1.0 V, the dark current was 29 mA whereas the light current of the device upon illumination of SWIR light was 34 mA, indicating the detection of the SWIR light. The current device achieved the I_{light}/I_{dark} ratio of 1.17 at -1 V. At -1 V, the dark current is very high which contributes to the shot noise in the photodiode.

The typical photoresponses of the device shown in 5.2 (b) demonstrate the reproducible photocurrent response and cycling stability even at a voltage bias of 0 V. The response profile shows that the measured rise time (τ_{rise}: from 10% to 90% of the saturated value) and fall time (τ_{fall}: from 90% to 10% of the peak value) were 5 sec and 4 sec. The device structure of our InSb-QPDs was robust and their performances were maintained even after leaving at room temperature in ambient air for 6 months. It is noted that the InSb-QPD exhibited pronounced photovoltaic behavior under light illumination at the external bias voltage of 0 V, indicating that the InSb-QPD functions as a self-driven photodetector.

Here, I assume shot noise is the main source of noise for the photodiode, as InSb is a low bandgap material.[46] EQE value of the photodiode at -1 V has achieved more than 100% (Fig. 5.2 (c)). In this study, I assume due to the electron-trapping effect in HTL by the photoconductive gain is caused higher than the unity gain. This also has been reported for photo- diode photodetectors in many reports. EQE spectra show maxima at the

spectral wavelength from 1000 nm to 1200 nm which is very similar to the excitonic feature of the absorption spectra of the sample. Responsivity (R), defined by the generated photocurrent per incident unit optical power, was calculated according to the previous Equation 4.4. In this work, I obtained the best

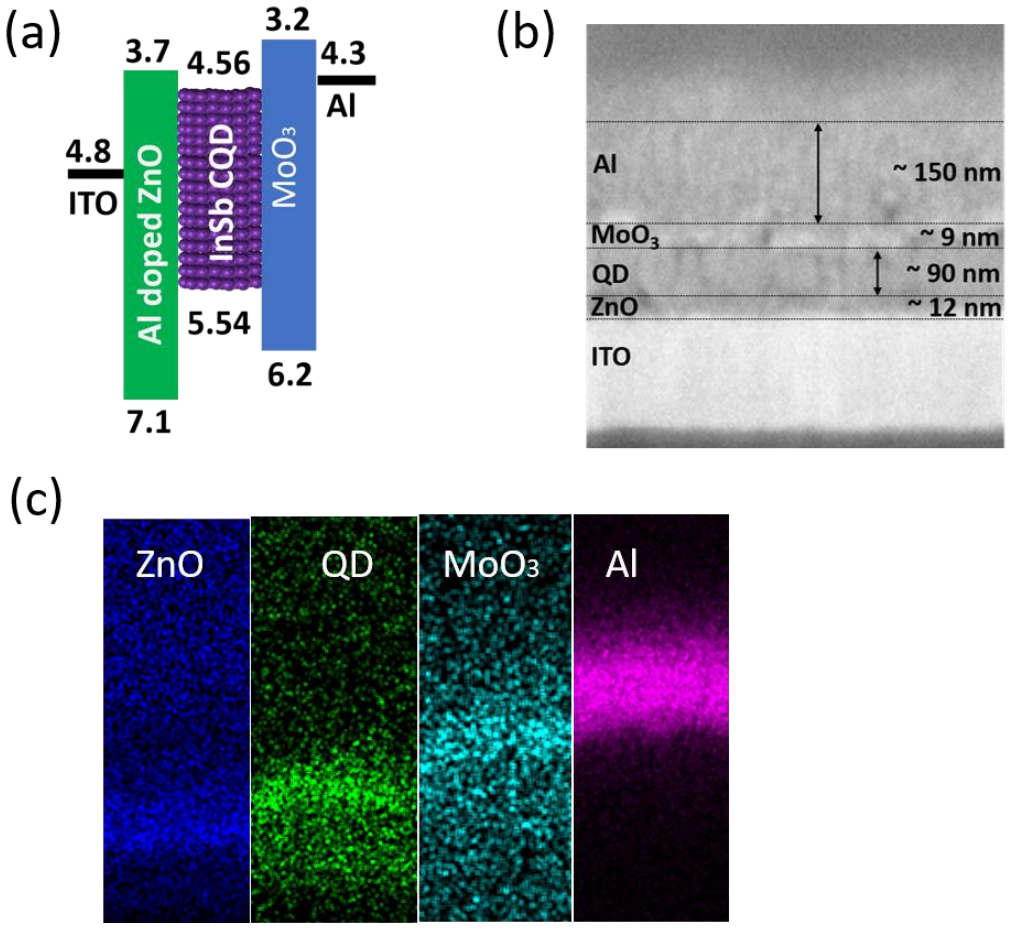

FIGURE 5.1: (a) Energy band diagram in the unbiased conditions. (b) A typical cross-sectional SEM image of the InSb-QPD structure with the organic-inorganic hybrid multi-layer stack. (c) EDS maps of the cross-sectional SEM image.

values of R= 7.08 A/W and D = 4.33×10^{10} Jones at -1 V (Jones = cm $Hz^{1/2}$ W^{-1}), respectively. The wavelength-dependent value of R and D* from the range 800 nm to 1800 nm were calculated under constant optical light power density (1 mW/cm^2) at the bias voltage of -1 V (See Fig. 5.2 (d)) for ~5.1 nm InSb QD based photodiodes. Maxima of R and D* values were achieved from wavelength of 1000 nm to 1200 nm for ~5.1 nm QDs, which is a similar

feature with the optical exciton characteristic of the respective samples, which justify the QDs are highly sensitive at their exciton wavelength range under SWIR light.

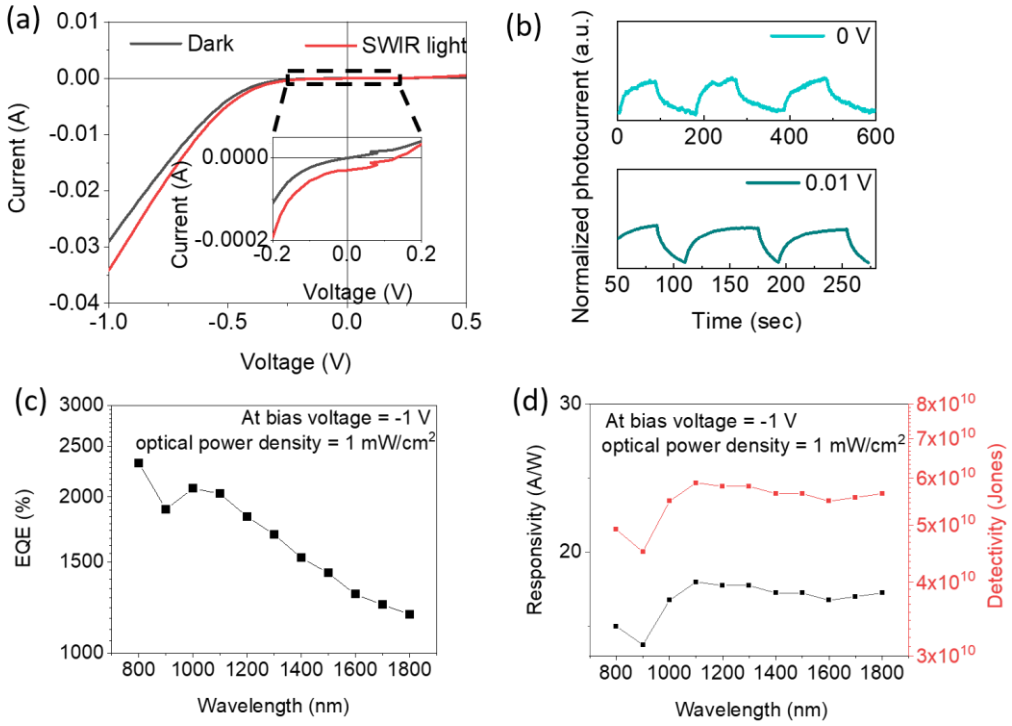

FIGURE 5.2: (a) I-V characteristics of InSb-QPD under illumination of SWIR light (λ=1200-1800 nm, 18 mW/cm^2). (b) Time response curve of photocurrent at 0 V and 0.01 V bias voltage under the SWIR light illumination. Spectral (c) EQE, (d) R and D* of the photodiode at -1 V bias voltage under constant optical light intensity of 1 mW/cm^2.

5.2 Conclusion

In conclusion, I have manipulated the surface properties of InSb CQDs by ligand exchange which further influence to change the energy level and doping concentrations. Additionally, the mobility of the CQDs were improves by exchanging the ligands. By exchanging the ligand, I have designed SWIR photodiodes with very competitive values of figure of merits with non-toxic material system.

In ***Chapter 2***, I introduce the synthesis of InSb CQDs with easily available

halide (chloride and bromide) precursors by following hot-injection synthesis protocol. Where, successful synthesis of InSb with different size nanocrystal was obtained. Further, I have followed the size selective precipitation to obtain monodisperse nanocrystal to achieve better optical properties of nanocrystals. Optical properties and bandgap were varied from 840 nm to 1450 nm with 1.8 eV to 0.86 eV, while photoluminescence was achieved from 1015 nm and 1440 nm for QD size 2.6 nm and 4.8 nm respectively. Further, I report on no-oxidation on surface for both In and Sb element among all the previously reported InSb CQD literature.

In ***Chapter 3*** exploits successful ligand exchange from OLA to bromide and sulfide for better optoelectronics characteristics for photodiodes. Importantly, to shorten the interparticle distance of adjacent QDs electronically neutral is important, which is presented as a proof of evidence by measuring zeta potential. Whereas reduction of interparticle distance was confirmed by GI-XRD and HR-TEM.

In ***Chapter 4***, I studied InSb CQD based photodiode for SWIR application. Two different capped InSb CQD were used as active layer of the device. By comparing the device performance sulfide capped InSb QPD achieves better photoresponse, responsivity and EQE under SWIR light. Additionally, sulfur capped device achieves less dark current. Sulfur and bromide capped InSb CQD were used to prepare electron only and hole only device to calculate the carrier mobility and trap density. Finally, sulfur caped device shows significant improvement in the carrier mobility and less trap density which further impact to achieve better performed.

In the last ***Chapter 5***, I propose an al-inorganic device prepared by InSb CQDs capped with bromide ligand. In future, these device structure can be modified with sulfur and different ligands to improve the practical applicability of InSb QPD for SWIR region.

Bibliography

1. Rauch, T. *et al.* Near-infrared imaging with quantum-dot-sensitized organic photodiodes. *Nat Photonics* **3**, 332–336 (2009).
2. Ren, Z. *et al.* Bilayer PbS quantum dots for high-performance photodetectors. *Advanced materials* **29**, 1702055 (2017).
3. Tang, X., Ackerman, M. M., Chen, M. & Guyot-Sionnest, P. Dual-band infrared imaging using stacked colloidal quantum dot photodiodes. *Nat Photonics* **13**, 277–282 (2019).
4. Shin, D. *et al.* Photon-efficient imaging with a single-photon camera. *Nat Commun* **7**, 12046 (2016).
5. Yu, J. *et al.* Near-infrared photodetectors based on CH 3 NH 3 PbI 3 perovskite single crystals for bioimaging applications. *J Mater Chem C Mater* **10**, 274–280 (2022).
6. Rogalski, A., Martyniuk, P., Kopytko, M., Madejczyk, P. & Krishna, S. InAsSb-based infrared photodetectors: Thirty years later on. *Sensors* **20**, 7047 (2020).
7. Li, N. *et al.* SWIR photodetection and visualization realized by incorporating an organic SWIR sensitive bulk heterojunction. *Advanced Science* **7**, 2000444 (2020).
8. Li, N. *et al.* Solution-processable infrared photodetectors: Materials, device physics, and applications. *Materials Science and Engineering: R: Reports* **146**, 100643 (2021).
9. Vafaie, M. *et al.* Colloidal quantum dot photodetectors with 10-ns response time and 80% quantum efficiency at 1,550 nm. *Matter* **4**, 1042–1053 (2021).
10. Clifford, J. P. *et al.* Fast, sensitive and spectrally tuneable colloidal-quantum-dot photodetectors. *Nat Nanotechnol* **4**, 40–44 (2009).
11. He, J. *et al.* Synergetic effect of silver nanocrystals applied in PbS colloidal quantum dots for high-performance infrared photodetectors. *ACS Photonics* **1**, 936–943 (2014).
12. Saran, R., Nordin, M. N. & Curry, R. J. Facile fabrication of PbS nanocrystal: C60 fullerite broadband photodetectors with high detectivity. *Adv Funct Mater* **23**, 4149–4155 (2013).
13. Tang, Y. *et al.* A Colloidal-Quantum-Dot Infrared Photodiode with High Photoconductive Gain. *Small* **14**, 1803158 (2018).
14. Rastogi, P. *et al.* Complex optical index of HgTe nanocrystal infrared thin films and its use for short wave infrared photodiode design. *Adv Opt Mater* **9**, 2002066 (2021).
15. Jia, B. W. *et al.* Monolithic integration of InSb photodetector on silicon for mid-infrared silicon photonics. *ACS Photonics* **5**, 1512–1520 (2018).
16. XIV. Experiments on the refrangibility of the invisible rays of the sun. *Philos Trans R Soc Lond* **90**, 284–292 (1800).
17. Akula, A., Ghosh, R. & Sardana, H. K. Thermal imaging and its application in defence systems. in *AIP conference proceedings* vol. 1391 333–335 (2011).
18. Rand, B. P., Xue, J., Yang, F. & Forrest, S. R. Organic solar cells with sensitivity extending into the near infrared. *Appl Phys Lett* **87**, (2005).
19. L. Bready, S. N. and D. D. Decision Making in Anesthesiology, Fourth Edition. *Maryland Heights, MO: Mosby Elsevier* (2007).
20. Corneliu Rablau. LIDAR – A new (self-driving) vehicle for introducing optics to broader engineering and non-engineering audiences. in *Proceeding of SPIE: Conference of Education and Training in Optics and Photonics* 11138–11143 (2019).
21. Seravalli, L., Trevisi, G. & Frigeri, P. Design and growth of metamorphic InAs/InGaAs quantum dots for single photon emission in the telecom window. *CrystEngComm* **14**, 6833 (2012).
22. D. A. Neaman. *Semiconductor Physics and Devices: Basic Principles*. (NY: McGrawHill, 2012).

23. Kagan, C. R., Lifshitz, E., Sargent, E. H. & Talapin, D. V. Building devices from colloidal quantum dots. *Science (1979)* **353**, (2016).
24. Chukwuocha, E. O., Onyeaju, M. C. & Harry, T. S. T. Theoretical Studies on the Effect of Confinement on Quantum Dots Using the Brus Equation. *World Journal of Condensed Matter Physics* **02**, 96–100 (2012).
25. Huang, W. *et al.* Size tunable and controllable synthesis of PbS quantum dots for broadband photoelectric response. *Opt Mater (Amst)* **142**, 113977 (2023).
26. Ginterseder, M. *et al.* Scalable synthesis of InAs quantum dots mediated through indium redox chemistry. *J Am Chem Soc* **142**, 4088–4092 (2020).
27. Liu, W., Chang, A. Y., Schaller, R. D. & Talapin, D. V. Colloidal insb nanocrystals. *J Am Chem Soc* **134**, 20258–20261 (2012).
28. Carey, G. H. *et al.* Colloidal Quantum Dot Solar Cells. *Chem Rev* **115**, 12732–12763 (2015).
29. Hetsch, F., Zhao, N., Kershaw, S. V. & Rogach, A. L. Quantum dot field effect transistors. *Materials Today* **16**, 312–325 (2013).
30. Saran, R. & Curry, R. J. Lead sulphide nanocrystal photodetector technologies. *Nat Photonics* **10**, 81–92 (2016).
31. Choi, M. K., Yang, J., Hyeon, T. & Kim, D.-H. Flexible quantum dot light-emitting diodes for next-generation displays. *npj Flexible Electronics* **2**, 10 (2018).
32. Lee, H., Song, H.-J., Shim, M. & Lee, C. Towards the commercialization of colloidal quantum dot solar cells: perspectives on device structures and manufacturing. *Energy Environ Sci* **13**, 404–431 (2020).
33. Murray, C. B., Kagan, C. R. & Bawendi, M. G. Synthesis and Characterization of Monodisperse Nanocrystals and Close-Packed Nanocrystal Assemblies. *Annual Review of Materials Science* **30**, 545–610 (2000).
34. Murray, C. B. *et al.* Colloidal synthesis of nanocrystals and nanocrystal superlattices. *IBM J Res Dev* **45**, 47–56 (2001).
35. Murray, C. B., Norris, D. J. & Bawendi, M. G. Synthesis and characterization of nearly monodisperse CdE (E = sulfur, selenium, tellurium) semiconductor nanocrystallites. *J Am Chem Soc* **115**, 8706–8715 (1993).
36. LaMer, V. K. & Dinegar, R. H. Theory, Production and Mechanism of Formation of Monodispersed Hydrosols. *J Am Chem Soc* **72**, 4847–4854 (1950).
37. Nag, A., Zhang, H., Janke, E. & Talapin, D. V. Inorganic Surface Ligands for Colloidal Nanomaterials. *Zeitschrift für Physikalische Chemie* **229**, 85–107 (2015).
38. Horing, N. J. M. Nanostructure van der Waals interaction between a quantum well and a quantum dot atom. *J Phys A Math Gen* **39**, 6567–6573 (2006).
39. Robertson, J. D. *et al.* Purification of Nanoparticles by Size and Shape. *Sci Rep* **6**, 27494 (2016).
40. Mori, Y. Size-Selective Separation Techniques for Nanoparticles in Liquid. *KONA Powder and Particle Journal* **32**, 102–114 (2015).
41. Liu, M. *et al.* Efficiently Improved Photoluminescence in Cesium Lead Halide Perovskite Nanocrystals by Using Bis(trifluoromethane)sulfonimide. *J Phys Chem Lett* **13**, 1519–1525 (2022).
42. Papagiorgis, P. *et al.* The Impact of Ligand Removal on the Optoelectronic Properties of Inorganic and Hybrid Lead Halide Perovskite Nanocrystal Films. *Adv Opt Mater* (2023) doi:10.1002/adom.202301501.
43. Papagiorgis, P. *et al.* The Impact of Ligand Removal on the Optoelectronic Properties of Inorganic and Hybrid Lead Halide Perovskite Nanocrystal Films. *Adv Opt Mater* (2023) doi:10.1002/adom.202301501.
44. Kirmani, A. R., Walters, G., Kim, T., Sargent, E. H. & Amassian, A. Optimizing Solid-State Ligand Exchange for Colloidal Quantum Dot Optoelectronics: How Much Is Enough? *ACS Appl Energy Mater* **3**, 5385–5392 (2020).
45. Wang, W. *et al.* Colloidal Inorganic Ligand-Capped Nanocrystals: Fundamentals, Status, and Insights into Advanced Functional Nanodevices. *Chem Rev* **122**, 4091–

4162 (2022).
46. Nemoto, K., Watanabe, J., Yamada, H., Sun, H.-T. & Shirahata, N. Impact of coherent core/shell architecture on fast response in InP-based quantum dot photodiodes. *Nanoscale Adv* **5**, 907–915 (2023).
47. Liu, Y. *et al.* Dependence of Carrier Mobility on Nanocrystal Size and Ligand Length in PbSe Nanocrystal Solids. *Nano Lett* **10**, 1960–1969 (2010).
48. Chen, M., Hao, Q., Luo, Y. & Tang, X. Mid-Infrared Intraband Photodetector *via* High Carrier Mobility HgSe Colloidal Quantum Dots. *ACS Nano* **16**, 11027–11035 (2022).
49. Green, M. L. H. A new approach to the formal classification of covalent compounds of the elements. *J Organomet Chem* **500**, 127–148 (1995).
50. Kagan, C. R. & Murray, C. B. Charge transport in strongly coupled quantum dot solids. *Nat Nanotechnol* **10**, 1013–1026 (2015).
51. Boles, M. A., Ling, D., Hyeon, T. & Talapin, D. V. The surface science of nanocrystals. *Nat Mater* **15**, 141–153 (2016).
52. Chatterjee, S., Nemoto, K., Ghosh, B., Sun, H.-T. & Shirahata, N. Solution-Processed InSb Quantum Dot Photodiodes for Short-Wave Infrared Sensing. *ACS Appl Nano Mater* **6**, (2023).
53. Liu, W., Lee, J.-S. & Talapin, D. V. III–V Nanocrystals Capped with Molecular Metal Chalcogenide Ligands: High Electron Mobility and Ambipolar Photoresponse. *J Am Chem Soc* **135**, 1349–1357 (2013).
54. Talapin, D. V. & Murray, C. B. PbSe Nanocrystal Solids for n- and p-Channel Thin Film Field-Effect Transistors. *Science (1979)* **310**, 86–89 (2005).
55. Liu, Y. *et al.* PbSe Quantum Dot Field-Effect Transistors with Air-Stable Electron Mobilities above 7 $cm^2 V^{-1} s^{-1}$. *Nano Lett* **13**, 1578–1587 (2013).
56. Oh, S. J. *et al.* Engineering Charge Injection and Charge Transport for High Performance PbSe Nanocrystal Thin Film Devices and Circuits. *Nano Lett* **14**, 6210–6216 (2014).
57. Choi, J.-H. *et al.* Bandlike Transport in Strongly Coupled and Doped Quantum Dot Solids: A Route to High-Performance Thin-Film Electronics. *Nano Lett* **12**, 2631–2638 (2012).
58. Norman, Z. M., Anderson, N. C. & Owen, J. S. Electrical Transport and Grain Growth in Solution-Cast, Chloride-Terminated Cadmium Selenide Nanocrystal Thin Films. *ACS Nano* **8**, 7513–7521 (2014).
59. Zhao, T. *et al.* General Synthetic Route to High-Quality Colloidal III–V Semiconductor Quantum Dots Based on Pnictogen Chlorides. *J Am Chem Soc* **141**, 15145–15152 (2019).
60. Zhang, H., Jang, J., Liu, W. & Talapin, D. V. Colloidal Nanocrystals with Inorganic Halide, Pseudohalide, and Halometallate Ligands. *ACS Nano* **8**, 7359–7369 (2014).
61. Poirier, G. E. & Pylant, E. D. The Self-Assembly Mechanism of Alkanethiols on Au(111). *Science (1979)* **272**, 1145–1148 (1996).
62. Koleilat, G. I. *et al.* Efficient, Stable Infrared Photovoltaics Based on Solution-Cast Colloidal Quantum Dots. *ACS Nano* **2**, 833–840 (2008).
63. Lin, Q. *et al.* Phase-transfer ligand exchange of lead chalcogenide quantum dots for direct deposition of thick, highly conductive films. *J Am Chem Soc* **139**, 6644–6653 (2017).
64. Ahmed, F., Dunlap, J. H., Pellechia, P. J. & Greytak, A. B. A p-type PbS quantum dot ink with improved stability for solution processable optoelectronics. *Chemical Communications* **57**, 8091–8094 (2021).
65. Nag, A. *et al.* Metal-free Inorganic Ligands for Colloidal Nanocrystals: S^{2-}, HS^-, Se^{2-}, HSe^-, Te^{2-}, HTe^-, TeS_3^{2-}, OH^-, and NH_2^- as Surface Ligands. *J Am Chem Soc* **133**, 10612–10620 (2011).
66. Fafarman, A. T. *et al.* Thiocyanate-Capped Nanocrystal Colloids: Vibrational Reporter of Surface Chemistry and Solution-Based Route to Enhanced Coupling in Nanocrystal Solids. *J Am Chem Soc* **133**, 15753–15761 (2011).

67. Liu, M. *et al.* Hybrid organic–inorganic inks flatten the energy landscape in colloidal quantum dot solids. *Nat Mater* **16**, 258–263 (2017).
68. Brown, P. R. *et al.* Energy Level Modification in Lead Sulfide Quantum Dot Thin Films through Ligand Exchange. *ACS Nano* **8**, 5863–5872 (2014).
69. Xu, Q. *et al.* Ultrafast Colloidal Quantum Dot Infrared Photodiode. *ACS Photonics* **7**, 1297–1303 (2020).
70. Leemans, J. *et al.* Colloidal III–V Quantum Dot Photodiodes for Short-Wave Infrared Photodetection. *Advanced Science* **9**, (2022).
71. Xia, P. *et al.* Sequential Co-Passivation in InAs Colloidal Quantum Dot Solids Enables Efficient Near-Infrared Photodetectors. *Advanced Materials* **35**, (2023).
72. Sun, B. *et al.* Fast Near-Infrared Photodetection Using III–V Colloidal Quantum Dots. *Advanced Materials* **34**, (2022).
73. Song, J. H., Choi, H., Pham, H. T. & Jeong, S. Energy level tuned indium arsenide colloidal quantum dot films for efficient photovoltaics. *Nat Commun* **9**, 4267 (2018).
74. He, M. *et al.* Colloidal InSb Quantum Dots/Organic Integrated Bulk Heterojunction for Fast and Sensitive Near-Infrared Photodetectors. *Adv Photonics Res* **3**, (2022).
75. Kagan, C. R. Flexible colloidal nanocrystal electronics. *Chem Soc Rev* **48**, 1626–1641 (2019).
76. Kwak, D.-H., Ramasamy, P., Lee, Y.-S., Jeong, M.-H. & Lee, J.-S. High-Performance Hybrid InP QDs/Black Phosphorus Photodetector. *ACS Appl Mater Interfaces* **11**, 29041–29046 (2019).
77. McDonald, S. A. *et al.* Solution-processed PbS quantum dot infrared photodetectors and photovoltaics. *Nat Mater* **4**, 138–142 (2005).
78. Liu, Y. *et al.* Merging Passivation in Synthesis Enabling the Lowest Open-Circuit Voltage Loss for PbS Quantum Dot Solar Cells. *Advanced Materials* **35**, 2207293 (2023).
79. Xu, J. *et al.* 2D matrix engineering for homogeneous quantum dot coupling in photovoltaic solids. *Nat Nanotechnol* **13**, 456–462 (2018).
80. Sze, S. M. & Ng, K. K. *Physics of Semiconductor Devices*. (Wiley, 2006). doi:10.1002/0470068329.
81. Hou, B. *et al.* Evolution of Local Structural Motifs in Colloidal Quantum Dot Semiconductor Nanocrystals Leading to Nanofaceting. *Nano Lett* **23**, 2277–2286 (2023).
82. Pak, S. *et al.* Consecutive Junction-Induced Efficient Charge Separation Mechanisms for High-Performance MoS_2 /Quantum Dot Phototransistors. *ACS Appl Mater Interfaces* **10**, 38264–38271 (2018).
83. Levinshtein, M., Rumyantsev, S. & Shur, M. *Handbook Series on Semiconductor Parameters*. vol. 2 (WORLD SCIENTIFIC, 1996).
84. Nilsson, H. A. *et al.* Temperature dependent properties of InSb and InAs nanowire field-effect transistors. *Appl Phys Lett* **96**, (2010).
85. Evans, C. M., Castro, S. L., Worman, J. J. & Raffaelle, R. P. Synthesis and Use of Tris(trimethylsilyl)antimony for the Preparation of InSb Quantum Dots. *Chemistry of Materials* **20**, 5727–5730 (2008).
86. Kim, S.-W., S., S. & Lee, B. Y. $InAs_x Sb_{1-x}$ alloy nanocrystals for use in the near infrared. *Chem. Commun.* 4811–4813 (2006) doi:10.1039/B611099A.
87. Busatto, S. *et al.* Luminescent Colloidal InSb Quantum Dots from *In Situ* Generated Single-Source Precursor. *ACS Nano* **14**, 13146–13160 (2020).
88. Tamang, S., Kim, K., Choi, H., Kim, Y. & Jeong, S. Synthesis of colloidal InSb nanocrystals via in situ activation of $InCl_3$. *Dalton Transactions* **44**, 16923–16928 (2015).
89. Yarema, M. & Kovalenko, M. V. Colloidal Synthesis of InSb Nanocrystals with Controlled Polymorphism Using Indium and Antimony Amides. *Chemistry of Materials* **25**, 1788–1792 (2013).
90. He, M. *et al.* Colloidal InSb Quantum Dots/Organic Integrated Bulk Heterojunction for

Fast and Sensitive Near-Infrared Photodetectors. *Adv Photonics Res* **3**, (2022).
91. Crisp, R. W. *et al.* Selective antimony reduction initiating the nucleation and growth of InSb quantum dots. *Nanoscale* **10**, 11110–11116 (2018).
92. Langille, M. R., Personick, M. L., Zhang, J. & Mirkin, C. A. Defining Rules for the Shape Evolution of Gold Nanoparticles. *J Am Chem Soc* **134**, 14542–14554 (2012).
93. King, M. E., Kent, I. A. & Personick, M. L. Halide-assisted metal ion reduction: emergent effects of dilute chloride, bromide, and iodide in nanoparticle synthesis. *Nanoscale* **11**, 15612–15621 (2019).
94. Copperthwaite, R. G., Kunze, O. A., Lloyd, J., Neely, J. A. & Tuma, W. Surface Analysis of InSb by X-Ray Photoelectron Spectroscopy (XPS). *Zeitschrift für Naturforschung A* **33**, 523–527 (1978).
95. Garbassi, F. XPS and AES study of antimony oxides. *Surface and Interface Analysis* **2**, 165–169 (1980).
96. Chen, D., Li, C., Zhu, Z., Fan, J. & Wei, S. Interface effect of InSb quantum dots embedded in <math display="inline"> <mrow> <mi>Si</mi> <msub> <mi mathvariant="normal">O</mi> <mn>2</mn> </msub> </mrow> </math> matrix. *Phys Rev B* **72**, 075341 (2005).
97. Tyschenko, I. E., Volodin, V. A. & Popov, V. P. Raman Scattering in InSb Spherical Nanocrystals Ion-Synthesized in Silicon-Oxide Films. *Semiconductors* **53**, 493–498 (2019).
98. Algarni, Z., Singh, A. & Philipose, U. Synthesis of Amorphous InSb Nanowires and a Study of the Effects of Laser Radiation and Thermal Annealing on Nanowire Crystallinity. *Nanomaterials* **8**, 607 (2018).
99. Makuła, P., Pacia, M. & Macyk, W. How To Correctly Determine the Band Gap Energy of Modified Semiconductor Photocatalysts Based on UV–Vis Spectra. *J Phys Chem Lett* **9**, 6814–6817 (2018).
100. Efros, Al. L. & Rosen, M. Quantum size level structure of narrow-gap semiconductor nanocrystals: Effect of band coupling. *Phys Rev B* **58**, 7120–7135 (1998).
101. Allan, G. & Delerue, C. Confinement effects in PbSe quantum wells and nanocrystals. *Phys Rev B* **70**, 245321 (2004).
102. Calvin, J. J., Kaufman, T. M., Sedlak, A. B., Crook, M. F. & Alivisatos, A. P. Observation of ordered organic capping ligands on semiconducting quantum dots via powder X-ray diffraction. *Nat Commun* **12**, 2663 (2021).
103. Gull, S., Jamil, M. H., Zhang, X., Kwok, H. & Li, G. Stokes Shift in Inorganic Lead Halide Perovskites: Current Status and Perspective. *ChemistryOpen* **11**, (2022).
104. Tang, J. *et al.* Colloidal-quantum-dot photovoltaics using atomic-ligand passivation. *Nat Mater* **10**, 765–771 (2011).
105. Ghosh, B. *et al.* Origin of the Photoluminescence Quantum Yields Enhanced by Alkane-Termination of Freestanding Silicon Nanocrystals: Temperature-Dependence of Optical Properties. *Sci Rep* **6**, 36951 (2016).
106. Schubert, E. F. *Doping in III-V semiconductors*. (2015).
107. Owen, J. The coordination chemistry of nanocrystal surfaces. *Science (1979)* **347**, 615–616 (2015).
108. Chen, P. E., Anderson, N. C., Norman, Z. M. & Owen, J. S. Tight Binding of Carboxylate, Phosphonate, and Carbamate Anions to Stoichiometric CdSe Nanocrystals. *J Am Chem Soc* **139**, 3227–3236 (2017).
109. Shirahata, N., Hasegawa, T., Sakka, Y. & Tsuruoka, T. Size-Tunable UV-Luminescent Silicon Nanocrystals. *Small* **6**, 915–921 (2010).
110. Ren, Y.-K. *et al.* Controllable intermediates by molecular self-assembly for optimizing the fabrication of large-grain perovskite films via one-step spin-coating. *J Alloys Compd* **705**, 205–210 (2017).
111. van Oversteeg, C. H. M. *et al.* Water-Dispersible Copper Sulfide Nanocrystals via Ligand Exchange of 1-Dodecanethiol. *Chemistry of Materials* **31**, 541–552 (2019).
112. Wan, Y., Goubet, N., Albouy, P.-A., Schaeffer, N. & Pileni, M.-P. Hierarchy in Au

Nanocrystal Ordering in a Supracrystal: II. Control of Interparticle Distances. *Langmuir* **29**, 13576–13581 (2013).
113. Yazdani, N., Bozyigit, D., Yarema, O., Yarema, M. & Wood, V. Hole Mobility in Nanocrystal Solids as a Function of Constituent Nanocrystal Size. *J Phys Chem Lett* **5**, 3522–3527 (2014).
114. Ghosh, B., Yamada, H., Chinnathambi, S., Özbilgin, İ. N. G. & Shirahata, N. Inverted Device Architecture for Enhanced Performance of Flexible Silicon Quantum Dot Light-Emitting Diode. *J Phys Chem Lett* **9**, 5400–5407 (2018).
115. Surawijaya, A., Chandra, Z., Sulthoni, M. A., Idris, I. & Adiono, T. Modeling and Simulation of Si Grating Photodetector Fabricated Using MACE Method for NIR Spectrum. *Electronics (Basel)* **12**, 663 (2023).
116. Baierl, D. *et al.* Solution-processable inverted organic photodetectors using oxygen plasma treatment. *Org Electron* **11**, 1199–1206 (2010).
117. Salunkhe, P., Bhat, P. & Kekuda, D. Performance evaluation of transparent self-powered n-ZnO/p-NiO heterojunction ultraviolet photosensors. *Sens Actuators A Phys* **345**, 113799 (2022).
118. Pan, X. *et al.* Incorporating Guanidinium as Perovskitizer-Cation of Two-Dimensional Metal Halide for Crystal-Array Photodetectors. *Chem Asian J* **16**, 1925–1929 (2021).
119. Lan, Z. *et al.* Near-infrared and visible light dual-mode organic photodetectors. *Sci Adv* **6**, (2020).
120. Lee, J. W., Kim, D. Y. & So, F. Unraveling the Gain Mechanism in High Performance Solution-Processed PbS Infrared PIN Photodiodes. *Adv Funct Mater* **25**, 1233–1238 (2015).
121. Diedenhofen, S. L., Kufer, D., Lasanta, T. & Konstantatos, G. Integrated colloidal quantum dot photodetectors with color-tunable plasmonic nanofocusing lenses. *Light Sci Appl* **4**, e234–e234 (2015).
122. Konstantatos, G., Clifford, J., Levina, L. & Sargent, E. H. Sensitive solution-processed visible-wavelength photodetectors. *Nat Photonics* **1**, 531–534 (2007).
123. Xie, Y. *et al.* Broad-Spectral-Response Nanocarbon Bulk-Heterojunction Excitonic Photodetectors. *Advanced Materials* **25**, 3433–3437 (2013).
124. Afzal, A. M. *et al.* Highly efficient self-powered perovskite photodiode with an electron-blocking hole-transport NiOx layer. *Sci Rep* **11**, 169 (2021).
125. Ma, F. *et al.* Nickel oxide for inverted structure perovskite solar cells. *Journal of Energy Chemistry* **52**, 393–411 (2021).
126. Zhu, H. L. *et al.* Room-Temperature Solution-Processed NiO_x :PbI_2 Nanocomposite Structures for Realizing High-Performance Perovskite Photodetectors. *ACS Nano* **10**, 6808–6815 (2016).
127. Hsiao, K.-C. *et al.* Enhancing Efficiency and Stability of Hot Casting p–i–n Perovskite Solar Cell via Dipolar Ion Passivation. *ACS Appl Energy Mater* **2**, 4821–4832 (2019).
128. Chiang, C.-H. & Wu, C.-G. Bulk heterojunction perovskite–PCBM solar cells with high fill factor. *Nat Photonics* **10**, 196–200 (2016).
129. Röhr, J. A. & MacKenzie, R. C. I. Analytical description of mixed ohmic and space-charge-limited conduction in single-carrier devices. *J Appl Phys* **128**, (2020).
130. Heo, J. H. *et al.* Hysteresis-less mesoscopic CH3NH3PbI3 perovskite hybrid solar cells by introduction of Li-treated TiO2 electrode. *Nano Energy* **15**, 530–539 (2015).